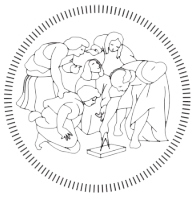

POLITECNICO
MILANO 1863

Gravitational-magnetic tug

An investigation on combined gravitational and magnetic interaction for asteroid deflection and control

Supervisor:	Prof. Camilla Colombo	Author:	Renato Cirelli
Co-supervisor:	Dr. Juan Luis Gonzalo Gómez	Mat.	883828

Master Thesis

School of Industrial and Information Engineering
Department of Aerospace Science and Technology

Academic Year 2019-2020

Declaration of Authorship

This content is original, written by the Author, Renato Cirelli. All the non-originals information, taken from previous works, are specified and recorded in the Bibliography.

When referring to this work, full bibliographic details must be given, i.e.

Renato Cirelli, "Gravitational-magnetic tug, an investigation on combined gravitational and magnetic interaction for asteroid deflection and control", 2021. Master of Science in Space Engineering, School of Industrial and Information Engineering, Department of Aerospace Science and Technology, Politecnico di Milano, Italy. Supervisor Prof. Camilla Colombo , Co-Supervisor Dr. Juan Luis Gonzalo Gómez.

Printed in Italy

Acknowledgments

I would like to express my gratitude to my advisors, Prof. Camilla Colombo and Dr. Juan Luis Gonzalo Gómez. I appreciate the time you dedicated to me, the enthusiasm you showed and the positive support you provided.

My deepest gratitude goes to my girlfriend and to my family. Luisa, thank you for your patient, your presence and for your great support in all these beautiful moments that we lived, and we are living together. Thank you Mum, Sister and all family members for your support, without it none of these would have been possible. Unfortunately, Father, Agnese, Ana and Dora are not here today to live with us this wonderful achievement, but I know they would be proud of me and of the person I have become. They were, and They will always be in my heart and mind.

I want to thank all the people that crossed my path and made these years better than they could have ever been. A special thank goes to quite a long but not exhaustive list of people. The space guys and girls with whom I shared most of my university life: Edo, David, Ila, Giulio, Vale, Scudi, Han||naH, Alo, Giulia, Ale, Marzia, and Alvaro. Meni and Bavu, thank you for all the good time spent together and the delicious food/wine you made me discover. The Garba-Team: Luca, Ros, Jessica, Labbro, Daniel, Cobi, Marco, Zeno, and Vitto. Marisa and Paolo for always supporting me in many ways. Tommy, for all the crazy adventures in Milano city. The people that embraced new and not well-defined challenges with me (e.g., SpaceUp Team, Aracne Team, MIMESiS Team). All the people that alleviated the quarantine period through every virtual environments possible. All the old areo-friends, the people I met during my time in Villa Litta, the friend from the library, and many others.

This journey has come to an end, leaving me with an enormous amount of memories that will never fade.

Milano, April 2021 Renato Cirelli

Abstract

Near Earth Objects (NEOs) pose a great threat to our planet not only due to the direct consequences of a possible impact, but rather because of the long-term climatic effects it would induce. Many deflection strategies, based on either impacting the NEO or gently pushing it for a long time, have been proposed to reduce its impact probability or to avoid its passage into an Earth's gravitational keyhole that would lead to a future impact. Among these, the Gravitational Tug (GT) technique is one of the best options in case of high warning time, contained asteroid mass and small targeted deflection at Minimum Orbit Intersection Distance (MOID). On the other hand, it often requires the spacecraft (SC) to non-inertial hover close to the NEO, which can increase mission risk and reduce linear momentum transfer efficiency between NEO and SC.

In the dissertation, the simultaneous use of gravitational and magnetic interactions between a NEO (i.e., target), with natural global magnetisation state, and a SC (i.e., chaser), equipped with an onboard magnetic field generator subsystem, is investigated with the goal of improving the achieved deflection at MOID. The analysis is based on the GT model extended to include the free-free dipoles magnetic interaction under the far-field assumptions. It takes into account the chaser's propulsive and power generation subsystems efficiencies, the target and chaser's heliocentric motions and the target's tumbling state. Furthermore, the target-chaser optimal relative configuration is analysed and a control law for the orientation of the chaser's magnetic dipole is proposed, considering the limitations associated to its attitude and orbit control subsystems. Dynamics is formulated using relative motion models and is integrated numerically in MATLAB® and Simulink® environments. Two test cases based on a target with known estimated magnetic properties and a virtual target are presented, highlighting the conditions for which the gravitational-magnetic tug technique can effectively increase the deflection performance compared to simply using GT, according to different metrics.

Sommario

Gli asteroidi rappresentano una minaccia per il nostro pianeta, non solo per le conseguenze dirette di un loro possibile impatto, ma per gli effetti a lungo termine che questo produrrebbe sul clima. Per scongiurare un tale evento, sono state proposte numerose strategie che mirano a ridurre la probabilità di un impatto imminente, o a evitare il passaggio dell'asteroide in una zona di risonanza gravitazionale che porterebbe ad un impatto futuro. Le strategie esplorate adottano l'applicazione di una spinta ridotta sull'asteroide per un periodo di tempo prolungato, oppure optano per una violenta e rapida collisione con esso.

Ad oggi, la tecnica del trattore gravitazionale risulta essere una delle opzioni migliori in caso di abbondante preavviso, massa dell'asteroide contenuta e ridotta deflessione valutata all'istante di minima distanza orbitale tra Terra e asteroide. Tuttavia, tale metodo, richiede spesso di mantenere un satellite nei pressi dell'asteroide in moto relativo non-inerziale e di operare a distanze ridotte; queste condizioni operative, oltre ad aumentare il rischio associato alla missione, riducono l'efficienza del trasferimento di momento lineare tra asteroide e satellite.

Nella tesi viene proposto l'utilizzo simultaneo delle interazioni gravitazionali e magnetiche (i.e, trattore gravitazionale-magnetico) tra un asteroide, caratterizzato da uno stato di magnetizzazione globale naturale, e un satellite, dotato di un sistema in grado di generare un campo magnetico. L'obiettivo è valutare l'efficacia di tale cooperazione, misurare l'eventuale incremento in deflessione e stimare i requisiti che il satellite deve soddisfare per ottenerlo.

L'analisi effettuata amplia il modello di trattore gravitazionale includendo l'interazione tra dipoli magnetici. Il modello proposto considera: l'efficienza dei sottosistemi del satellite adibiti alla generazione di spinta e alla generazione di energia di bordo, il moto eliocentrico dell'asteroide e del satellite e lo stato di rotazione dell'asteroide. Viene analizzata la configurazione ottimale che permette di massimizzare l'interazione tra satellite e asteroide, al fine di migliorarne la deflessione. Vengono inoltre proposte due strategie di controllo per il dipolo generato a bordo dal satellite, tenendo in

considerazione le limitazioni associate al sottosistema di controllo d'assetto orbitale. La dinamica è formulata utilizzando modelli di moto relativo e integrata numericamente in Matlab® e Simulink®.

Per valutare le condizioni in cui il trattore gravitazionale-magnetico può aumentare le prestazioni in termini di deflessione rispetto all'utilizzo del trattore gravitazionale, il modello sviluppato viene applicato un asteroide virtuale ed a uno reale, con proprietà magnetiche note.

Contents

List of Figures

List of Tables

List of Acronyms

Acronym	Description
AOCS	Attitude and Orbit Control Subsystem
AU	Astronomial Units
BEP	Break Even Point
BFF	Body Fixed Frame
CM	Center of Mass
DCL	Dipole Control Law
DOFS	Degrees Of Freedom
GMT	Gravitational-Magnetic Tug
GT	Gravitational Tug
IAU	International Astronomical Union
IO	Impacted Object
IVP	Initial Value Problem
KEP	Keplerian Elements
LHS	Left Hand Side
LTA	Low-Thrust Action
LVLH	Local Vertical Local Horizontal
MOID	Minimum Orbit Intersection Distance
MT	Magnetic Tug
NEA	Near Earth Asteroid
NEC	Near Earth Comet
NEO	Near Earth Object
NTH	Normal Tangential
ODE	Ordinary Differential Equation
PGS	Power Generation Subsystem
PS	Propulsive Subsystem
R2BP	Restricted Two-Body Problem
RAAN	Right Ascension of the Ascending Node
RHS	Right Hand Side
RNI	Requirement of Non-Impingement

Acronym	Description
RTS	Requirement of Tug Sustainability
SC	Spaceraft
SCEI	Sun Centred Ecliptic Inertial
SD	Space Debris
SI	International System of units
SMM	Specific Magnetic Moment
SMS	Superconductive Magnets Subsystem
SSSB	Small Solar System Body
TM	Tugging Mode
TOF	Time Of Flight
TRL	Technology Readiness Level

List of Symbols

Symbol	Description	Unit
a	Orbital semi-major axis	km
α_{POD}	Fraction of the power mass dedicated to thrust generation	$-$
Az_i	Azimuth of object's i-th magnetic dipole referred to the target's motion normal unit vector	rad
β_i	Nozzle i-th cant angle with respect to a common direction	deg
β_p	Cant angle of an adapted canted nozzles configuration	deg
m_C	Chaser's mass	kg
G	Universal gravitational constant	$km^2/(s^2 kg)$
d_{RNIL}	Relative hovering distance's lower boundary	m
m_{dry}	Chaser's dry mass	kg
e	Orbital eccentricity	$-$
η_{th}	Thrust efficiency	$-$
γ	Flight path angle	deg
m_{fuel}	Chaser's available fuel mass	kg
m_{C0}	Chaser's total mass at interception	kg
F_{GT}	Gravitational tugging force	N
h_i	Elevation of object's i-th magnetic dipole measured from the target orbital plane	rad
d	Target-chaser hovering relative distance measured from their centers of mass	m
i	Orbital plane inclination	rad

Symbol	Description	Unit
t_0	Initial time	s
Isp	Specific impulse of the chaser's propulsive subsystem	s
M	Mean anomaly	rad
$\mu_{\epsilon\mu 0}$	Vacuum magnetic permeability	H/m
ν	Magnetic amplifiction factor	$-$
$\underline{\mu}_{\epsilon\mu,i}$	Magnetic dipole moment vector of object i	Am^2
μ_i	Gravitational constant of object i	km^3/s^2
μ_T	Gravitational constant of the target	km^3/s^2
ω	Argument of pericenter	rad
h	Specific orbital angular momentum	km^2/s
ϕ_i	Exhaust cone semi-amplitude angle of nozzle i	deg
ϕ_p	Exhaust cone semi-amplitude angle of an adapted canted nozzles configuration	deg
POD	Chaser's power mass over dry mass ratio	$-$
m_{pw}	Chaser's mass dedicated to the onboard power generation subsystem	kg
$m_{pw,\epsilon\mu}$	Chaser's power mass dedicated to the magnetic dipole generation	kg
$m_{pw,th}$	Chaser's power mass dedicated to the thrust generation	kg
Ω	Right ascension of the ascending node	rad
K	Dipoles relative orientation coefficient	$-$
K_r	Dipoles radial relative orientation coefficient	$-$
K_σ	Dipoles orthogonal relative orientation coefficient	$-$
g_0	Gravitational acceleration on Earth surface, at sea level	m/s^2
m_T	Target's mass	kg
R_T	Target equivalent radius	m
τ_{pw}	Mass of the power generation subsystem to produce one Watt of electric power	kg/W
t_{co}	Cut-off epoch	s
θ	True anomaly	rad
t_i	Interception epoch	s

Symbol	Description	Unit
T_n	Total thrust generated by the chaser's propulsive subsystem	N
t_{tug}	Total tugging time	s
ξ_{th}	Thrust generated by the chaser with one Watt of electric power	N/W

Chapter 1

Introduction

This chapter presents the problem posed by Near Earth Objects (NEOs), and reviews most of the commonly proposed technique in the literature that aims to diminish the risk of an actual impact with planet Earth. A brief classification of the NEOs population is given, both in terms of orbital motion and impacting risk measurement, and an overview their physical and magnetic properties is carried out. The chapter also reviews past, present and future missions that operated in proximity of a NEO, focusing on the ones that gathered magnetic information about the object.

1.1 Near Earth Objects and Space Debris

NEOs and Space Debris (SD) pose a high concern to everyday life on planet Earth. NEOs are ancient objects that have populated the solar system for many millions of years, mostly reliquiae of an early stage of planetary formation that brought the material contained into the protoplanetary disk surrounding the newly born sun, our star, to become the planets and moons we see today. SDs are remanent of man-made objects, designed to sustain the rush environment of space for decades, whose original task was to improve our everyday life on planet Earth.

NEOs are natural objects that orbit our Sun, that can reach Earth proximity and eventually collide with it. They have been and are important sources of information for the scientific community, for instance, they contain the information related to the material abundance in the young solar system environment [1], they allow the study of complex dynamic interactions such as binary systems [2] and desegregation processes dynamics [3]. Moreover, they have attracted the interest of the private sector and brought it to invest in research for space resource gathering [4], defining the path for a possible new space economy that can improve not only space exploration but also our life and impact on planet Earth.

SDs are mainly composed by abandoned launch vehicle stages, mission related debris, fragmentations, and non-functional spacecrafts that orbit Earth, creating a sort of cloud that surrounds our planet. In such environment, a high velocity collision between two objects can easily degenerate into a cascade effect with devastating consequences on operational spacecrafts (i.e., Kessler syndrome) [5]. Since the beginning of human space exploration, the number of objects orbiting Earth is increased, reaching a population of 28210 actively tracked objects [6]. To mitigate the SDs generation, and maintain the usability of space, it is required a strong compliance with end-of-life disposal guidelines. The main approaches are identified in the active debris removal, and design-for-demise [7].

Even though NEOs and SD may be considered totally different objects, there are common techniques that aims to mitigate the very different risk that they pose. In the thesis, the focus is given on the mitigation of a possible impact between a NEO and planet Earth, however, the explored concepts may be also applied to SDs mitigation.

1.1.1 Near Earth Objects

According to the International Astronomical Union (IAU), the solar system bodies population can be partitioned in the commonly accepted classes summarised in figure 1.1.

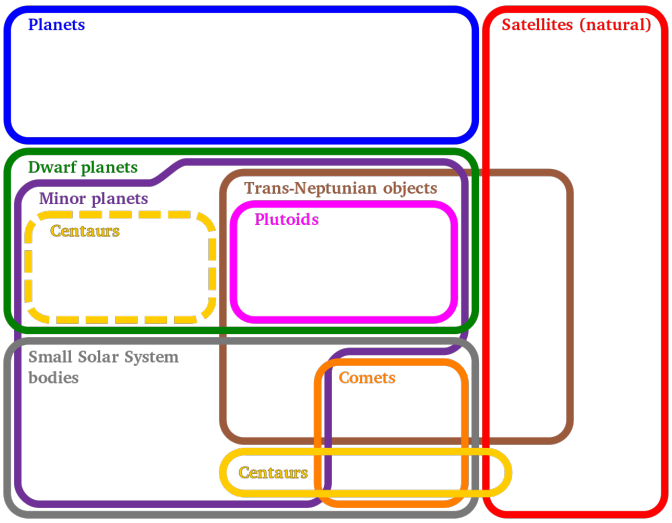

Figure 1.1: *Euler diagram of the solar system bodies [8].*

The most significant one, in the context of this dissertation, is the Small Solar System Body (SSSB) class composed by objects that are neither planets, dwarf planet nor natural satellites. Almost any SSSB that can reach Earth proximity during its heliocentric motion is considered to be a NEO if its perihelion (i.e., closest reachable point with respect to the Sun) is within 1.3 Astronomial Units (AU). A refined classification of such objects is obtained considering different characteristics (e.g., nature, extension, orbital motion).

According to definitions commonly adopted in the literature [9, 10, 11], NEOs can be partitioned in

- **Near Earth Asteroids (NEAs)**
  SSSBs that can reach Earths proximity and have no active visible surface phenomena (e.g., tail, coma)
- **Near Earth Comets (NECs)**
  SSSBs that can reach Earth proximity, have either a tail or a coma and have an orbital period shorter than 200 years. Typically, they are less dense than NEAs and characterised by an higher relative velocity with respect to Earth, at close approach

Figure 1.2 presents the overall population, as of 15 March 2021, counting 25299 individuals NEAs and 113 NECs [11].

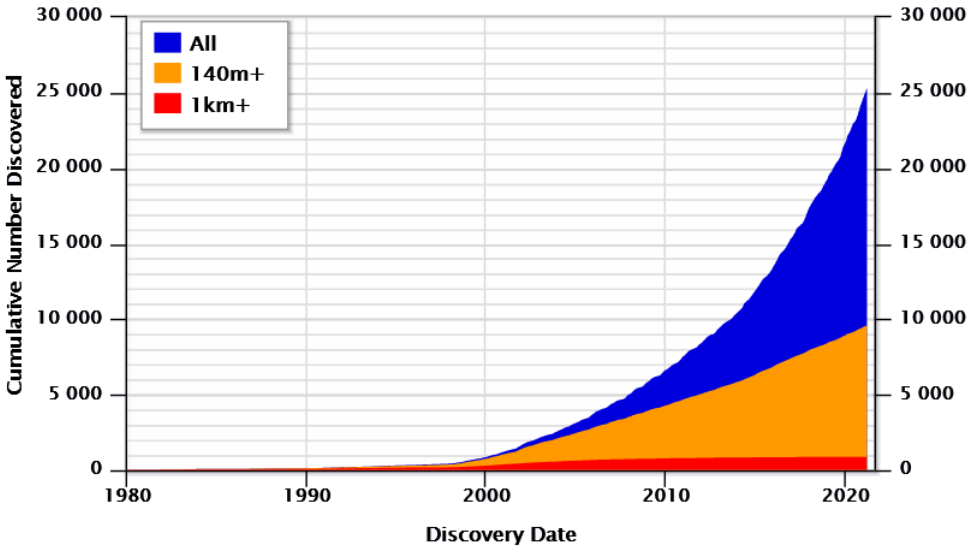

Figure 1.2: *Near Earth objects cumulative number evolution in time [11].*

Orbital based classification

It is common to divide NEOs in groups, or dynamical classes, named upon the first discovered element of the group itself [12]. These are defined considering the NEO orbital motion about the Sun and the Earth trajectory as

- **Nearly Earth-Crosser**
  The NEO motion projected on the ecliptic plane (i.e., Earth's orbital plane) is not crossing the Earth's trajectory. Therefore, the object can only perform a close approach of the planet
  - **Armor group**
    Named upon an asteroid discovered in 1932, Armor's NEOs have a heliocentric orbit within $1 - 1.3$ AU and include 37.0% of the entire NEA population.
  - **Atira group**
    Named upon an asteroid discovered in 2003, Atira's NEOs have a heliocentric orbit smaller than 1 AU and include 0.1% of the entire NEA population.
- **Earth-Crosser**
  The NEO motion projected on the ecliptic plane is crossing the Earth's trajectory. Therefore, the object can perform either a close approach (i.e., flyby) of or an impact with the planet.
  - **Apollo group**
    Named upon an asteroid discovered in 1932, Apollo's NEOs have a semi-major axis greater than 1 AU and a perihelion distance smaller than 1 AU, resulting in an orbital period longer than Earth's one. They include 55.3% of the entire NEA population.
  - **Aten group**
    Named upon an asteroid discovered in 2003, Aten's NEOs have a semi-major axis smaller than 1 AU and an aphelion (i.e., farthest reachable point with respect to the Sun) distance greater than 1 AU, resulting in an orbital period shorter than Earth's one. They include 7.6% of the entire NEA population.

Any NEO can evolve from one group to another within short time scales due to the exposure to different kind of perturbations (e.g., massive planets gravitational attraction, Yarkovsky effect, solar radiation pressure) and the population can increase due to different generation mechanisms [13].

Risk based classification

The outcomes of a NEO impacting planet Earth are connected to its kinetic energy at close approach conditions, which is proportional to its mass and the second power of the relative velocity in respect the Earth, and to its impact probability connected to how well its trajectory is known in terms of position and velocity vectors (i.e., state vector of the object and associated uncertainty).

Commonly, two different classifications are adopted to describe the hazard posed by a NEO

- **Torino scale**
  Primarily designed for public communication of impact risk and adopted by IAU in 1999, it describes the likelihood of an impact and its severity in terms of outcomes once the kinetic energy and the impact probability of the object are known. This approach is designed for public communication of impact risks.

- **Palermo scale**
  Primarily designed for technical comparison of the impact risk, it describes the likelihood of an impact and its severity in terms of outcomes comparing the former to the background risk, an average risk posed by objects of at lest the same size as the impacting one within the time interval from the object detection to the potential impact event [14]. This approach is designed principally to facilitate communication among astronomers.

Potentially hazardous objects

A NEA can be classified as a potentially hazardous objects if the closest approach to planet Earth (i.e., minimum orbital intersection distance) is closer than $0.05AU$ (i.e., 19.5 times the Earth-Moon distance) and its dimension is larger than $150\,[m]$. Such object's impact on Earth surface would have devastating consequences, either locally or globally. As of 15 March 2021, up to 2173 NEAs are identified in this class [10].

Physical properties

Most of the available properties of asteroids are derived from correlations between measurements performed either on ground or in orbit. Unless close approaches to

the asteroid happen, either with an Earth flyby or an encounter during an interplanetary mission, these remain the only way to retrieve meaningful information.

The rotational period and the shape can be correlated to the light curve of the object [15] but poor information upon the actual spin axis persist. The asteroid mass can be estimated analysing how its gravitational field is interacting with any other close object (e.g., binary asteroid system, other object flyby) or how it interacts with a spacecraft close to it [16].

Magnetic Properties

The magnetic characterization of a NEO is associated to the fraction of mineral constituents, their distribution within the NEO volume and to the presence of internal/external phenomena that can alter its magnetisation state [17, 18] (e.g., active convective nucleus, magnetosphere, high external magnetic gradients).

Each constituent can be described by either its magnetic susceptibility (i.e., state of self-magnetisation upon external magnetic field application) in the case of non-magnetized materials or by its spontaneous magnetisation state in the case of magnetized ones.

The evaluation of such state is a challenging task, and it is usually performed in different ways

- **Close approach, close proximity and in-situ operations**
  A magneto-sensitive subsystem of the Spaceraft (SC) is used to measure the NEO magnetic signature by analysing either its intensity or its interaction with the solar wind [19, 20] (i.e., draping, the deformation of the solar wind magnetic field lines), typically done during a close approach to the object [21, 22]. This allows to have an overview of the overall magnetisation state of the NEO. The same subsystem can be used when either close proximity or in-situ operations are performed but, in this case, mainly local information about the magnetisation state are retrieved.

- **Meteorite class correlations**
  The meteorites fallen on Earth are analysed in order to find information about a possible remanent magnetic field present in the main object that generated them [23]. Typically, the magnetic susceptibility of the samples are correlated with its metal content [24], but in-situ measurements have demonstrated that they do not correlate well with such meteoritic studies [25].

Up to date, limited information about the global-magnetization state of asteroids is available. A non-comprehensive list of past mission's findings is here briefly reported, focusing on the achieved results.

- **ROSETTA MISSION**
  An ESA mission with target comet 67P/Churyumov-Gerasimenko, it was composed by a spacecraft (i.e., Rosetta) and a lander (i.e., Philae) and performed two flybys close to NEOs (21)Lutetia and (2867) Steins. It found no conclusive evidence of a global magnetisation during (21)Lutetia flyby [26] and a very weak interaction with the solar wind in the case of (2867)Steins one [27]. Regarding the comet magnetic properties, no significant magnetisation of the surface was observed [28].

- **HAYABUSA 2 MISSION**
  A JAXA sample and return mission of asteroid (162173)Ryugu, it found a local magnetisation state at the centimetre/sub-centimetre level during in-situ operations at the NEO. On the other hand, no sign of a global magnetisation was detected [29, 30].

- **NEAR MISSION**
  A NASA mission to asteroid (433) Eros, the first one ever to go into orbit around an asteroid. The mission found no global magnetisation state during in-orbit and on-ground operations [30].

- **GALILEO MISSION**
  A NASA mission with main objective to study planet Jupiter, it performed a close approach to asteroid (951) Gaspra during its interplanetary travel. It found non trivial magnetic interaction between the asteroid and the solar wind, suggesting an overall magnetisation state [21].

- **DEEP SPACE 1 MISSION**
  A NASA mission first of its kind, it was the first time that an ion-engine was used for an interplanetary mission. It performed a close approach to asteroid (9969) Braille, finding an evident global magnetisation with no stable magnetosphere [31].

Table 1.1 summarises all the available magnetic information retrieved from past mission analysis [31, 25]

1.1.2 Deflection strategies

Even thought civil defense (e.g., evacuation, sheltering) may be a cost-effective mitigation measure in the case of small NEOs, a preventive approach would always be

Body	**Mean radius**	**Density**	**Spec. magnetic moment**
	$[km]$	$[kg/m^3]$	$[Am^2/kg]$
Gaspra	7	4000	0.024
Braille	0.8	3900	0.028
Steins	3	3200	10^{-3}
Lutetia	49	3400	10^{-7}
Eros	9	2650	10^{-6}
Vesta	530	3900	0.026
Mathilde	26	1340	0.075
Ida	16	2600	0.038

Table 1.1: *Summary of the estimated magnetic properties of an identified group of NEAs*

perceived as a better option, and it may be the only valid one for bigger class of NEOs [32]. Different deflection strategies have been studied and proposed with the aim of mitigating the risk of collision between a NEO and planet Earth. They all consist of either an instantaneous or a persistent deviating action which is used to change the NEO heliocentric orbit, aiming to a higher MOID and a lower impact probability.

Generally, the deflection is achieved by exploiting the action-reaction principle within the system formed by the NEO (i.e., the target) and a SC (i.e., the chaser) which is subjected to an acceleration, direct result of a net external force (i.e., the deflection action). Referring to the duration of such action, it is possible to identify

- **Impulsive strategy**
  The velocity vector of the target is changed in an instantaneous way at a specific instant of time (i.e., epoch),
- **Low-push strategy**
  The nominal state of the target is changed in a continuous way starting from an initial epoch until either the MOID event or a final epoch.

Another possible classification is obtained considering the NEO-SC system and analysing its momentum variation. In this framework, it is possible to have

- **Mass expulsion**
  The system momentum variation is obtained ejecting mass from either the NEO or SC,

- **Mass acquisition**
  The system momentum variation is obtained acquiring mass,
- **Mass expulsion/acquisition**

In general, impulsive techniques are able to produce higher deflections than the low-thrust ones, especially when the mass and size of the target is relevant. For smaller sizes and masses, low-thrust strategies may become a better option, especially when the target deflection is limited (e.g., keyhole avoidance [33, 34]), but they all require a high warning time (i.e., time from the identification of the threat to the actual deflective action to take place). In both cases, the optimality of the solution shall be addressed with multi-criteria analysis [35]. An overview of the most common deflection strategies is here proposed.

Impulsive Strategies

- **Kinetic impactor**
  This is considered the strategy with the highest Technology Readiness Level (TRL) and consists of impacting the target with a massive spacecraft at the highest achievable velocity. To do so, the interplanetary transfer of the spacecraft is carefully designed to maximize the relative velocity at target interception [36]. The achieved linear momentum variation can also be enhanced by the ejection of mass or gasses that can happens in such high velocity impacts [37].
- **Nuclear Blast**
  This strategy is the most efficient one in terms of energy transfer to the target and may be considered one of the most effective [38] in case of larger bodies in course of impact with planet Earth (i.e., diameter greater than $1km$). Several concepts are proposed and are all based on the idea of detonating a nuclear device either close, onto, or inside the target. The main drawback of this approach is the possible generation of a cloud of smaller debris, made from the original target, without any real control over their post-deflection trajectory [39]. In addition, the usage of such technology in outer space is technically banned by space treaties.

Low Thrust Strategies

- **Low thrust tug**
  It consists of a low-thrust generation device carefully placed on the body to be deflected and exploited to slowly change the latter's orbit. This method implies a physical attachment to the body surface and its effects are affected

by any target rotational state that can misalign the direction of pointing of the generated thrust. In addition, operating on the surface in a low gravity environment could create conditions that alter the nominal operations of the used devices [40].

- **Gravity tug**
  This strategy may be considered the most simple to implement with nowadays technology (i.e., high TRL) and it consists of a spacecraft, placed in a controlled hovering position close to the target in such a way that it is able to exploit the mutual gravitational attraction to pull on it. Different hovering techniques have been proposed with the aim of reducing the loss in efficiency. These are are mainly associated with the impingement of the engines' mass ejecta onto the target surface [41, 42]. The equivalent low trust action acting on the target can reach magnitudes close to the mN level with deflection in the order of tens of kilometres when applied to a small target (i.e., diameter smaller than $200m$) and for a period of time typically longer than the orbital one. The main limiting factor is the maximum mass that a single launch vehicle can bring into orbit which, as of 7th April 2021, is $63800kg$ [43].

- **Electrostatic tug**
  The electrostatic interaction between charged spacecraft and a charged target is exploited to either push or pull the latter and modify its orbit. This concept has been originally proposed in the context of spacecraft formation-flying control [44] and involves the generation of a potential to create micro-newton interaction forces between the formation components. The usage of electrostatic tug for asteroid deflection may be an option for small asteroids, in the $100m$ range, using voltage levels in the order of $20kV$ that shall be maintained continuously between the chaser and the target itself [45]. This shall be done within the plasma environment of space that is affecting the interaction, shielding one of the two objects [46].

- **Laser ablation**
  A laser is used to induce either the vaporization or sublimation of a spot on the target surface, obtaining a mass ejecta that generates thrust [47]. Its applicability depends upon the target's composition, its shape and is affected by any residual rotational state. The results can be improved when the laser is also used to control the rotation of the target [48].

- **Magnetic tug**
  It consists in the generation of a magnetic field, onboard the spacecraft, capable to induce a magnetic interaction on the target. The main applications are

related to the maintenance and control of flight formations [49, 50, 51], the detumbling of a space debris or active satellite [52] and, the debris End-Of-Life manoeuvring or orbit maintenance [53, 54]. The drawbacks are connected to the small relative operative distance (i.e., order of meters) with respect to the target and to the magnitude of the generated magnetic field (i.e., up to a $20000 Am^2$ equivalent magnetic dipole) that can be required.

Gravity tug overview

Given that the dissertation is centred on the Gravitational Tug (GT) concept, a deeper overview is here proposed to better understand the different ways it can be implemented and studied, exploring the work of different authors. McInnes [55] analyses the GT studying the target-chaser's centre of mass heliocentric motion as a Keplerian orbit and the relative motion between the two objects as result of a gravitational coupling under either a static equilibrium (e.g., non-inertial hover fixed with respect to the target, inertial hover fixed for an inertial observer) or displaced orbit assumption. The latter approach shows a higher coupling efficiency leading to interesting advantages in terms of overall deflecting action and, therefore, a potentially better deflection at MOID.

Foster *et al.* [42] discuss the advantages of using multiple SCs to perform a GT deflection and propose three possible different operational modes to be adopted after rendezvous with the NEO. Results show an increment in deflecting efficiency up to 10%. Wie [56] demonstrated the usefulness of modified Clohessy–Wiltshire–Hill (i.e., linearised relative motion) equations for the preliminary control analysis and design of such strategies.

Yeomans *et al.* [57] study a possible deflection campaign in which a SC operating close to the NEO is exploited not only to deflect it but also to lower the uncertainties in its orbital parameters (i.e., improving the orbit determination problem), with final goal of defining the gravity tractor phase's requirements. The deflection action aims to avoid possible keyholes (i.e., resonant orbits that would bring to a future collisions with planet Earth) and it may be performed after a kinetic impactor when not sufficient to avoid an actual impact.

Brown [58] studies the gain factor, in terms of achieved deflecting force, between a novel magneto-tug and the gravity tug techniques. The NEO-SC system's interaction force is obtained from both the gravitational attraction and magnetic one resulting from the free-free magnetic dipole interaction of collocated magnets on both the NEO (i.e., a magnetic grid of $1.4T$ magnets) and on SC (i.e., superconducting magnet of $10T$). The achieved force can be up to two order of magnitudes higher com-

pared to the gravity tug technique, allowing higher deflecting Low-Thrust Action (LTA) (i.e., external net force acting on the system) and resulting into a better overall performance. On the other hand, the assumptions done by the author restrict applications to the case of non-spinning asteroid with aligned and collinear magnetic dipole moments, and a relative distance that may be dangerously small (i.e., order of 10^1 m). Moreover, the SC compatibility with such strong static magnetic field as well as its maintainability, for typical operational times, shall be investigated.

Yamaguchi *et al.* [59] study the electrostatic-gravitational tug in the context of displaced non-Keplerian orbits, often called 'artificial halo orbits'. The dynamics is described using non-homogeneous Clohessy-Wiltshire-Hill equations and numerically integrated in order to compare the deflection efficiency between the gravity and electrostatic tug in the context of displaced orbits.

1.2 Asteroid review

It is here presented a non-comprehensive review, as of 7th April 2021, of current missions that are either concluded, in course or planned, with the main goal to rendezvoused with a NEO.

1. **AIDA** (Planned)
   The Asteroid Impact and Deflection Assessment (AIDA) is a NASA/ESA collaboration that consists of a pair of space probes (i.e., Dart,Hera) that will study the effect of a kinetic impact on small moon of a binary asteroid system (i.e., (65803)Didymos). Dart is a 500kg impactor equipped with a single camera for close target navigation and is expected to impact the target in 2022, leading to a slight change in the small 160m moon (i.e., Dimorphos) motion about the main asteroid. Hera will follow in 2026, performing post impact scientific measurements (e.g., high-resolution imaging, laser and radio mapping of the surface).

2. **Hayabusa 1** (Concluded)
   Launched in 2003, it was a JAXA sample and return mission that rendezvoused with asteroid (25143) Itokawa in 2005. It performed different studies on the asteroid shape, spin, topography, composition and density, and found that it is probably originated from a bigger asteroid.

3. **Hayabusa 2** (Concluded)
   Launched in 2014, it was a JAXA sample and return mission to an asteroid called (162173)Ryugu in which the sampling was done after a high velocity

impact obtained using a projectile. The ejecta from the impact was analysed and four small rovers and one lander were deployed on the surface of the asteroid, performing in-situ investigations.

4. **Rosetta Mission** (Concluded)
   Launched in 2004, it was a mission to comet 67P/Churyumov-Gerasimenko carried out by ESA. Unique of its kind, it was the first mission to rendezvous a comet, the first to follow a comet evolution on its orbit about the Sun, and the first to deploy a lander on a comet's surface (i.e., Philae).

1.3 Dissertation objective

The thesis aims to asses the possibility of improving the deflection offered by a classical GT technique exploiting a magnetic interaction in cooperation with the chaser-target mutual gravitational attraction. The work done in a previous study [58] pointed out the advantages of using a magnetic interaction but assumed the target to be in a non-rotational state, equipped with a man-made device capable to generate a magnetic field, and a dangerously small asteroid-spacecraft relative distance. The thesis primary goal is to study the conditions for which the cooperation between these two forces are actually possible, considering the actual spacecraft limitation when a non-inertial hovering about the target is taking place. In addition, the magnetic properties of the target are considered as a direct consequence of a natural global magnetisation state which is no necessarily optimal for the selected tugging direction.

1.4 Dissertation structure

An introduction to the mathematical tools used in the dissertation is presented in chapter 2. These are then used in chapter 3 to study the gravitational-magnetic interaction between a target and a chaser, to develop the GMT model used to design the chaser in such a way that the tug can operate at the target for a given total tugging time, and to assess the GMT performance when the target is characterised by a tumbling state that alters its magnetic dipole orientation with respect the chaser.

This thesis was part of the COMPASS project: "Control for orbit manoeuvring by surfing through orbit perturbations"(Grant agreement No 679086). This project is a European Research Council (ERC) funded project under the European Unions Horizon 2020 research.

Chapter 2

Mathematical model

This chapter presents a review of the mathematical background that is later used in the dissertation. Section 2.1 introduces the reader to used notations and frames of reference, section 2.3 discusses the force models adopted to describes the accelerations acting on the considered objects (i.e., target and chaser), sections 2.5 covers fundamental concepts about the classical gravitational tug technique that are later extended to include a magnetic contribution, and section 2.6 develops some concepts used to model the gravitational-magnetic tug, in convenient non-inertial frames, that allows to estimate the chaser's control effort to maintain a selected hovering position with respect to the target.

2.1 Notations

The first instance of a quantity is always defined in an extensive way (i.e., symbol [dimension]) using International System of units (SI), it is then compacted to the symbol only. Whenever the dimension is not in SI the extensive notation is restored and the link between SI and the used dimension is underlined. The list of symbols (p. xix) summarises all the defined quantities throughout the current dissertation.

A scalar value is always indicated with a letter (e.g., α, a), a column vector with an underlined letter (e.g., $\underline{b}$, $\underline{\beta}$), a column unit vector with a hatted letter (e.g., $\hat{\xi}$, $\hat{p}$) and a matrix with a bold letter (e.g., $\mathbf{h}$, $\boldsymbol{\gamma}$). Subscripts are used to associate a quantity to a subject (e.g., m_{SC} is the mass of SC, $\underline{F}_{th}$ is the force generated by a thruster), to express a relative quantity (e.g., $\underline{v}_{SC-NEO}$ is the velocity of the SC relative to the NEO) and to describe action-reaction generalized forces (e.g., $\underline{F}_{SC\to NEO}$ is a force acting on the NEO due to the presence of SC). Pre-superscripts are used to indicate in which reference frames a vector is written (e.g., ${}^{\mathcal{H}}\underline{x}$ is a vector whose components are expressed in the reference frame $\mathcal{H}$).

2.2 Frame of reference

All the introduced frames of reference are constructed according to the right-hand rule and indicated as

$$\mathcal{H} : \{\hat{e}_1, \hat{e}_2, \hat{e}_3\}_O$$

where $\mathcal{H}$ is the frame name, O is the point at which the frame is centred and $\hat{e}_i$ are mutually orthogonal unit vectors that satisfy $\hat{e}_3 = \hat{e}_1 \times \hat{e}_2$. The latter can be written using the skew symmetric matrix operator associated to the vectorial product as

$$\begin{cases} \hat{e}_3 & = \hat{e}_1 \times \hat{e}_2 = [\hat{e}_1]^\wedge \hat{e}_2 \\ [\hat{e}_1]^\wedge & \triangleq \begin{bmatrix} 0 & -\hat{e}_{1,z} & \hat{e}_{1,y} \\ \hat{e}_{1,z} & 0 & -\hat{e}_{1,x} \\ -\hat{e}_{1,y} & \hat{e}_{1,x} & 0 \end{bmatrix} \end{cases}$$

This notation is used throughout the entire dissertation and allows, in general, a cleaner manipulation of vectorial relations.

Considering two frames of reference $\mathcal{H}$ and $\mathcal{K}$, the transformation matrix that brings a vector written in $\mathcal{H}$ components to $\mathcal{K}$ ones is defined as

$$\mathcal{K} : \{\hat{e}_4, \hat{e}_5, \hat{e}_6\}_{O'}$$

$$\mathbf{T}_{\mathcal{K}\to\mathcal{H}} = \begin{bmatrix} | & | & | \\ {}^{\mathcal{H}}\hat{e}_4 & {}^{\mathcal{H}}\hat{e}_5 & {}^{\mathcal{H}}\hat{e}_6 \\ | & | & | \end{bmatrix}$$

and coincides with the direction cosine matrix of the two frames [60].

In general, a reference frame can be classified as non-inertial or inertial according to, respectively, the presence or absence of fictitious forces arising from the fact that the frame itself is moving in space with a non-null linear or angular acceleration. As a result, the dynamics written in non-inertial frames is usually more complex and sometime leads to unintuitive results.

The frames of reference used in the dissertation are here briefly presented and consist of typical choices when it comes to describe the motion of an astronomical object.

Sun Centred Ecliptic Inertial Frame

The Sun Centred Ecliptic Inertial (SCEI) frame is defined according to Earth's orbital motion about the Sun and takes as a reference the Vernal direction (i.e., γ point), a point in the sky fixed in respect to distant stars. This frame is centred at the Sun's Center of Mass (CM) and constructed as

$$\mathcal{I} : \{\hat{\gamma}, \hat{h}_{\oplus} \times \hat{\gamma}, \hat{h}_{\oplus}\}_{CM_{\odot}} \tag{2.1}$$

where $\hat{\gamma}$ is the Vernal direction and $\hat{h}_{\oplus}$ is the angular momentum unit vector of planet Earth (i.e., Unit vector orthogonal to Earth's ecliptic plane).

Local Vertical Local Horizontal Frame

The Local Vertical Local Horizontal (LVLH) frame is a non-inertial frame associated to an object. It is defined considering the object position vector and its motion in respect to a reference point as

$$\begin{cases} \mathcal{L} : \{\hat{x}, \hat{h} \times \hat{x}, \hat{h}\}_P \\ \hat{h} \triangleq (\hat{x} \times \dot{\hat{x}})/|\hat{x} \times \dot{\hat{x}}| \end{cases} \tag{2.2}$$

where $\hat{x}$ is the position unit vector of the object, $\dot{\hat{x}}$ its velocity, $\hat{h}$ is the unit vector normal to its orbital plane, and P is a generic application point.

Normal Tangential Frame

The Normal Tangential (NTH) frame is a non-inertial frame associated to an object. It is defined considering the object velocity vector and its motion in respect to a reference point as

$$\begin{cases} \mathcal{N} : \{\dot{\hat{x}} \times \hat{h}, \dot{\hat{x}}, \hat{h}\}_P \\ \hat{h} \triangleq (\hat{x} \times \dot{\hat{x}})/|\hat{x} \times \dot{\hat{x}}| \end{cases} \tag{2.3}$$

Body Fixed Frame

The Body Fixed Frame (BFF) is a non-inertial frame attached to an object that follows its rotational state. Even though any point of the object is a feasible origin, the frame is here centred at the body's CM and particular axes are used to simplify the angular dynamic equations. It is defined as

$$\mathcal{B} : \{\hat{I}_1, \hat{I}_2, \hat{I}_3\}_{CM} \tag{2.4}$$

where $\hat{I}_i$ is the body i-th principal axis of inertia.

2.3 Force models

In this section the forces acting on the chaser and target, referred from now on as objects when the distinction is not required, are modelled and discussed. Whereas there may be many contributions, a deeper focus on the gravitational and magnetic interactions is given, mainly focusing on the latter one.

2.3.1 Gravitational interaction

The most general *n-body* problem describes the motion of n point masses subjected to merely their mutual gravitational interactions. Their translational motions can be described in an inertial frame of reference according to Newton's universal gravitational law as

$$\begin{cases} m_i \, {}^{\mathcal{I}}\underline{\ddot{x}}_i = \sum_{\substack{j=1 \\ j\neq i}}^{n} G\frac{m_i m_j}{r_{ij}^3}\left({}^{\mathcal{I}}\underline{x}_j - {}^{\mathcal{I}}\underline{x}_i\right), & i \in [1,n] \\ {}^{\mathcal{I}}\underline{\dot{x}}_i(t_0) = {}^{\mathcal{I}}\underline{\dot{x}}_{i,0} \\ {}^{\mathcal{I}}\underline{x}_i(t_0) = {}^{\mathcal{I}}\underline{x}_{i,0} \end{cases} \tag{2.5}$$

where G $[km^2/(s^2kg)]$ is the universal gravitational constant, m_i $[kg]$ is the mass of the i-th object, ${}^{\mathcal{I}}\underline{x}_i$ $[km]$ is its position in the inertial frame, and r_{ij} $[km]$ is the relative distance between objects i and j.

It is not possible to find any finite terms close form general solution to problem 2.5 and numerical simulations may be challenging due to the involved non-linearities. These make the solution to be chaotic (i.e., highly sensitive to initial conditions) and require the usage of specific mathematical tools to proceed with the dynamic analysis. On the other hand, such complexity is often reduced and assumptions are made to proceed with preliminary analysis and tackle the early stage of mission design. For instance, the simpler *Restricted Two-Body Problem (R2BP)* assumes $n = 2$, $m_2 \ll m_1$ and results into Ordinary Differential Equations (ODEs) that are integrable in close form, leading to the Keplerian orbit theory.

Restricted Two-body problem

Considering two objects, the R2BP describes the perturbed motion of m_2 (i.e., secondary object) relative to m_1 (i.e., primary object or main attractor), written in an inertial frame centred at m_1 CM. It is summarized in the Initial Value Problem (IVP) defined as

$$\begin{cases} {}^{\mathcal{I}}\ddot{\underline{r}}\,(t) = -\frac{\mu_1}{r^3}\ {}^{\mathcal{I}}\underline{r}\,(t) + {}^{\mathcal{I}}\underline{a}_p + {}^{\mathcal{I}}\underline{a}_c \\ {}^{\mathcal{I}}\dot{\underline{r}}\,(t_0) = {}^{\mathcal{I}}\dot{\underline{r}}_0 \\ {}^{\mathcal{I}}\underline{r}\,(t_0) = {}^{\mathcal{I}}\underline{r}_0 \end{cases} \tag{2.6}$$

where ${}^{\mathcal{I}}\underline{r} \equiv {}^{\mathcal{I}}\underline{r}_{2-1}$ $[km]$ is the relative position vector, μ_i $[km^3/s^2]$ with $i = 1$ is the primary's gravitational parameter, t_0 $[s]$ is the initial time, and ${}^{\mathcal{I}}\underline{a}_i$ $[km/s^2], i = \{p, c\}$ are the inertial accelerations induced by, respectively, perturbations to the R2BP dynamics and presence of any artificial actuation system that aims to control the secondary's motion about the primary.

Equations 2.6 can be used to approximate the motions of N bodies with a common main attractor (e.g., planets heliocentric motions, SSSBs motions about the Sun or about another body) as far as the latter induced acceleration is dominant in respect any other mutual gravitational contributions in the system [60].

2.3.2 Keplerian parameters

The unperturbed R2BP, obtained by setting ${}^{\mathcal{I}}\underline{a}_i = 0, i = \{p, c\}$ in equations 2.6, is numerically integrable and leads to the well known integral of motion

$$r = r(t) = \frac{h^2}{\mu_1} \frac{1}{1 + e\cos(\theta(t))} \tag{2.7}$$

where h $[km^2/s]$ is the specific orbital angular moment, a $[km]$ is the semi-major axis of the orbit, e $[-]$ is the orbital eccentricity , and θ $[rad]$ is the true anomaly.

Given m_2 initial state vector, its unperturbed motion is bounded to a plane (i.e., orbital plane) and uniquely identified as conic section (i.e., ellipse, hyperbola and parabola) described by different sets of orbital parameters. The Keplerian Elements (KEP) set is the most straightforward choice, and it is defined as

$$\underline{KEP} = [a, e, i, \Omega, \omega, \theta]^T \tag{2.8}$$

where i $[rad]$ is the orbital plane inclination with respect to the ecliptic plane, Ω $[rad]$ is the Right Ascension of the Ascending Node (RAAN) and, ω $[rad]$ is the argument of perigee.

Different sets are available in the literature (e.g., equinoctial elements, Euler parameters, Dromo elements) and are introduced to address possible singularities, to simplify algebraic manipulation, and to allow a better representation of particular phenomena; however, the KEP set is adopted in the dissertation.

Note that equation 2.7 is implicitly dependant upon time through the true anomaly, the link between them is retrieved as

$$\dot{\theta} = \frac{h}{r^2} \tag{2.9}$$

which is integrated either numerically, with semi-analytic approaches or analytically. Proceeding with the analytical integration of equation 2.9, it is possible to obtain the explicit formulation of only $t = t(\theta)$ whereas, the inverse function (i.e., $\theta = \theta(t)$) remains implicit.

Such integration leads to the Kepler's equation for orbital time [60] valid for a generic Keplerian orbit. The link can be particularized for a close orbit as

$$\begin{cases} M & = \frac{\mu_1^2}{h^3}(1-e^2)^{3/2}t \\ M & = E - e\sin(E) \\ \tan\left(\frac{E}{2}\right) & = \sqrt{\frac{1-e}{1+e}}\tan\left(\frac{\theta}{2}\right) \end{cases} \tag{2.10}$$

where E $[rad]$ is the eccentric anomaly and, M $[rad]$ is the mean anomaly, and t is the orbital time elapsed since the last pericenter passage.

2.3.3 Perturbation of the two-body problem

The perturbation term ${}^{\mathcal{J}}\underline{a}_p$ is associated to the net contributions of different sources: atmospheric drag, gravitational perturbations due to a primary with non-homogeneous mass distribution, solar radiation pressure, third body perturbations and others. In general, its magnitude is small compared to the gravitational acceleration induced by the main attractor, and the net result is visible in the KEP elements as either a fast (i.e., true anomaly), or slow (i.e., all the remaining elements) variation.

Third body perturbation

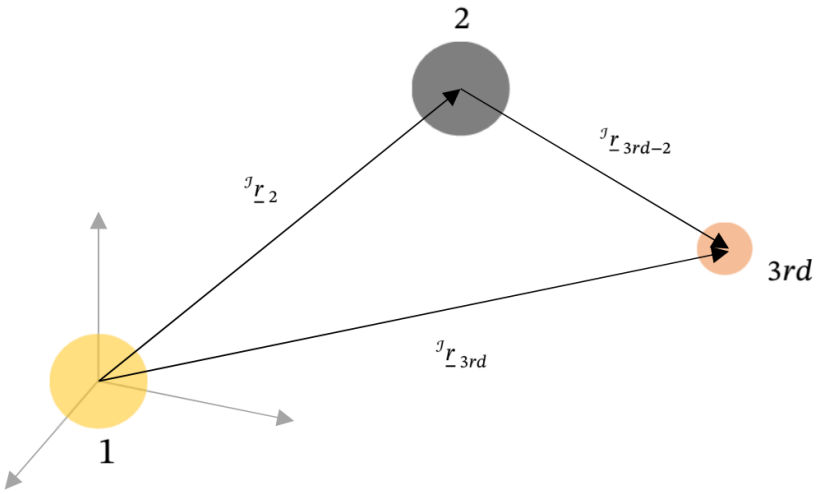

Figure 2.1: *Positions of the secondary mass and the third object with respect to the inertial frame centred at the primary mass.*

Referring to figure 2.1, the perturbation that a third body is inducing on a mass in orbit about a primary is

$$\begin{cases} {}^{\mathcal{J}}\underline{a}_{p,3rd} = \mu_{3rd}\left(\dfrac{{}^{\mathcal{J}}\underline{r}_{3rd-2}}{({}^{\mathcal{J}}r_{3rd-2})^3} - \dfrac{{}^{\mathcal{J}}\underline{r}_{3rd}}{({}^{\mathcal{J}}r_{3rd})^3}\right) \\ {}^{\mathcal{J}}\underline{r}_{3rd-2} = {}^{\mathcal{J}}\underline{r}_{3rd} - {}^{\mathcal{J}}\underline{r}_{2} \end{cases} \tag{2.11}$$

where $\mathcal{J}$ is a inertial frame of reference centred at the primary's CM (e.g., SCEI) and $^{\mathcal{J}}\underline{r}_{3rd}$ is the position of the third mass in that frame.

2.3.4 Propulsive subsystem

The chaser's Attitude and Orbit Control Subsystem (AOCS) is a collection of equipped actuators that allow the linear and angular momentum variation necessary to maintain the desired attitude and motion. Considering that the typical operational time for a low-thrust deflection mission can easily go beyond one year, the chaser considered in the dissertation is assumed to be equipped with electric propulsive units (e.g., ion thrusters) which exploit mass expulsion mechanisms for linear momentum management. Using the same approach as in [35], the total thrust that the chaser's Propulsive Subsystem (PS) can achieve is written as

$$\begin{cases} T_n = m_{pw} \frac{\xi_{th}}{\tau_{pw}} \\ m_{pw} = POD\, m_{dry} \end{cases} \tag{2.12}$$

where m_{pw} $[kg]$ is the mass dedicated to the on-board Power Generation Subsystem (PGS), m_{dry} $[kg]$ is the dry mass of the chaser, ξ_{th} $[N/W]$ is the PS's specific thrust, τ_{pw} $[kg/W]$ is the PGS's mass to power ration, and POD $[-]$ is the power mass to dry mass ratio. The latter is introduced in the formulation to allow the sensitivity analysis that is later carried out in the dissertation. Moreover, the mass to power ratio and the specific thrust are referred from now on as PGS and PS performances, respectively.

Recalling the specific impulse definition [60], the fuel depletion due for T_n $[N]$ generation is

$$\dot{m}_{fuel} = \frac{T_n}{Isp\, g_0} \tag{2.13}$$

where Isp $[s]$ is the specific impulse of the PS and g_0 $[m/s^2]$ is the standard gravitational acceleration on Earth evaluated at sea level (i.e., $g_0 = 9.81$ $[m/s^2]$).

The chaser's mass variation in time is then computed using the mass conservation on the chaser (i.e., $\dot{m}_C = -\dot{m}_{fuel}$) with equations (2.12) and (2.13), obtaining the following IVP

$$\begin{cases} \dot{m}_C = -POD \frac{\xi_{th}}{\tau_{pw}} \frac{m_{dry}}{Isp\, g_0} \\ m_C(t_0) = m_{C0} \end{cases} \tag{2.14}$$

where m_{C0} $[kg]$ is the initial chaser's total mass and t_0 is the time at which the thrust is applied.

For the purposes of the current preliminary analysis, the angular momentum management is not directly addressed. Yet, considerations on possible requirements related to such task are derived from the obtained results.

2.3.5 Magnetic interaction

The magnetic interaction between the considered objects is connected to their magnetic properties, their mutual orientation and their relative distance.
Assuming the objects are able to sustain current circulations within their domain, the obtained infinitesimal magnetic field can be computed recalling Biot and Savart law

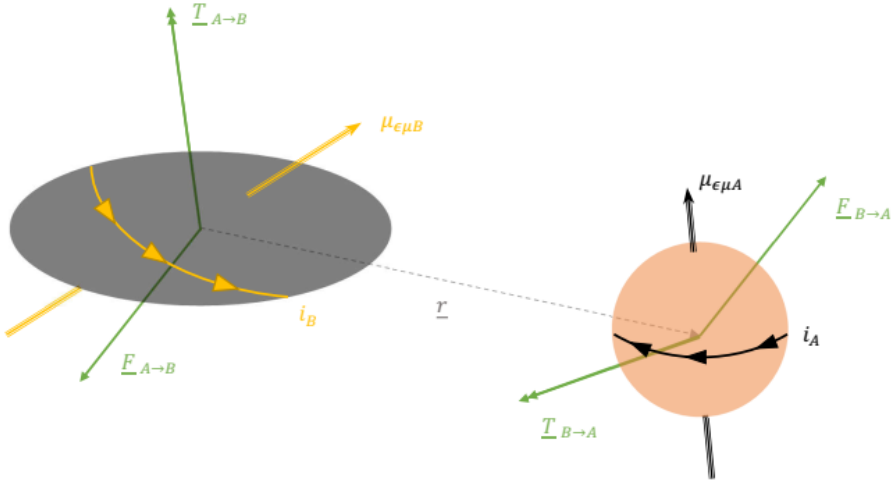

Figure 2.2: *Two domains that can support current circulations, separated by a known distance and interacting through mutual generalised force.*

$$d\underline{B} = \frac{i\,\mu_{\epsilon\mu_0}}{4\pi}\frac{\left[d\underline{l}\right]^{\wedge}\hat{r}}{r^2} \tag{2.15}$$

where i $[A]$ is the current flowing in the current-carrying domain, $\mu_{\epsilon\mu 0}$ $[H/m]$ is the magnetic permeability of vacuum, $d\underline{l}$ $[m]$ is the infinitesimal current-carrying domain length, and $\underline{r}$ $[m]$ is the vector pointing the location at which the field is evaluated starting from the infinitesimal element.

Considering two current-carrying domains A and B, represented in figure 2.2, the infinitesimal force acting on A due to the magnetic field of B is computed according to the Lorentz force developed on the moving charges in A (i.e., Laplace force) as

$$d\underline{F}_{B\to A} = i_A \left[d\underline{l}_a\right]^{\wedge} \underline{B}_B \tag{2.16}$$

where i_A is current flowing in domain A, $d\underline{l}_A$ is the infinitesimal element length of domain A, and $\underline{B}_B$ is the magnetic field generated by domain B.

Close-field and Far-field magnetic interaction for a two coil system

Equations (2.15) and (2.16) can be particularised for current-carrying coils composed by multiple turns, obtaining the *close-field* formulation of the magnetic interaction

$$\begin{cases} \underline{F}_{B\to A} = \dfrac{\mu_{\epsilon\mu_0}\, i_A N_A\, i_B N_B}{4\pi} \oint \left[\oint d\underline{B}_B \right]^{\wedge} d\underline{l}_A \\ \underline{\tau}_{B\to A} = \dfrac{\mu_{\epsilon\mu_0}\, i_A N_A\, i_B N_B}{4\pi} \oint \left[\underline{r}_A\right]^{\wedge} \left(\left[\oint d\underline{B}_B \right]^{\wedge} d\underline{l}_A \right) \end{cases} \tag{2.17}$$

where $\underline{r}_A$ is the relative position vector of the infinitesimal element of coil A and $N_i, i = \{A, B\}$ is the number of turns of coil i.

It is possible to obtain an analytical expression of equation (2.17) performing a Taylor expansion and retaining only the first order terms. Such approximation, referred to as *far-field* formulation, is proven to be acceptable when the inter-coil distance is greater than ~ 7 times the maximum coil radii, committing an error lower than 10% compared to the close-field formulation [61].

In this framework, the interaction between chaser C and the target T is described using magnetic dipole theory [62, 63, 64, 53] as

$$\begin{cases} \underline{F}_{T\to C} &= \frac{3\mu_{\epsilon\mu_0}}{4\pi r^4}((\underline{\mu}_{\epsilon\mu,T}\cdot\underline{\mu}_{\epsilon\mu,C})\hat{r} + (\underline{\mu}_{\epsilon\mu,T}\cdot\hat{r})\hat{\mu}_{\epsilon\mu,C} + (\underline{\mu}_{\epsilon\mu,C}\cdot\hat{r})\hat{\mu}_{\epsilon\mu,T} \\ & \quad -5(\underline{\mu}_{\epsilon\mu,T}\cdot\hat{r})(\underline{\mu}_{\epsilon\mu,C}\cdot\hat{r})\hat{r}) \\ \underline{F}_{C\to T} &= -\underline{F}_{T\to C}; \\ \underline{\tau}_{T\to C} &= \frac{\mu_{\epsilon\mu_0}}{4\pi r^3}\left[\underline{\mu}_{\epsilon\mu,C}\right]^{\wedge}\left(3(\underline{\mu}_{\epsilon\mu,T}\cdot\hat{r})\hat{r} - \underline{\mu}_{\epsilon\mu,C}\right) \\ \underline{\tau}_{C\to T} &= -\underline{\tau}_{T\to C} - \left[\underline{r}\right]^{\wedge}\underline{F}_{T\to C} \end{cases} \tag{2.18}$$

where $\mu_{\epsilon\mu 0}$ $[H/m]$ is the vacuum magnetic permeability, $\underline{\mu}_{\epsilon\mu,i}$ $[Am^2]$ is the magnetic dipole moment vector associated to object $i = \{T, C\}$, and $\underline{r} = \underline{r}_{T\to C}$ is the vector pointing the chaser from the target.

Equations 2.18 can also be rewritten in matrix form obtaining

$$\begin{cases} \underline{F}_{T\to C} &= \frac{3\mu_{\epsilon\mu 0}}{4\pi r^4}\mathbf{\Phi}(\underline{\mu}_{\epsilon\mu,T}, \underline{r})\underline{\mu}_{\epsilon\mu,C} \\ &= \frac{3\mu_{\epsilon\mu 0}}{4\pi r^4}\mathbf{\Phi}(\underline{\mu}_{\epsilon\mu,C}, \underline{r})\underline{\mu}_{\epsilon\mu,T} \\ \underline{\tau}_{T\to C} &= \frac{\mu_{\epsilon\mu 0}}{4\pi r^3}\left[\underline{\mu}_{\epsilon\mu,C}\right]^{\wedge}\left(\mathbf{\Gamma}(r)\underline{\mu}_{\epsilon\mu,T}\right) \end{cases} \tag{2.19}$$

where $\mathbf{\Gamma}$ is a non-singular matrix (i.e., invertible) dependant upon only the relative position vector and $\mathbf{\Phi}$ is a conditionally singular matrix dependant on both target's dipole orientation and relative position vector. The definition of these matrices is here omitted and can be found in appendix A.

It is always possible to impose a certain torque on one of the two objects, but there are relative configurations of the system for which a subset of forces are not imposable. Visually inspecting equations 2.18, it is found that whenever $\hat{\mu}_{\epsilon\mu,i} \cdot \hat{r} = 0$ the achievable magnetic force can only be contained within the plane defined by the relative position and the i-th magnetic dipole unit vector . Figure 2.3 shows the plane of achievable force directions for the condition $\hat{\mu}_{\epsilon\mu,C} \cdot \hat{r} = 0$.

Moreover, equations (2.18) show that the torque acting on the chaser is equal to the one acting on the target only when the magnetic force is directed as the relative position vector. In general, $\underline{\tau}_{T\to C} \neq \underline{\tau}_{C\to T}$ [65].

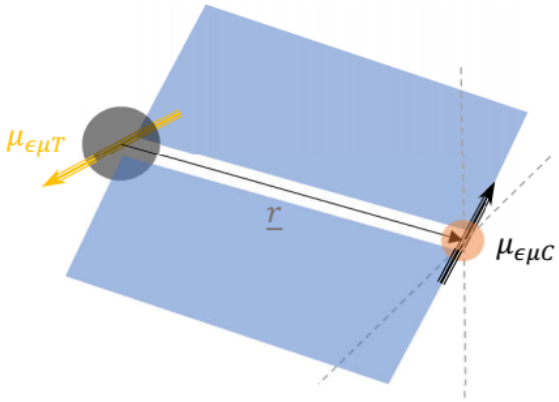

Figure 2.3: *Blue plane representing the locus of magnetic force directions when matrix* $\mathbf{\Phi}$ *is non invertible due to chaser relative orientation.*

2.4 Orbital deflection

The selection of a suitable deflection strategy is driven by the target orbital motion, its geo-physical properties and the available time to take action (i.e., warning time). Typically, the latter includes the Time Of Flight (TOF) required to reach the target and, in the case af a LTA strategy, the time to establish the proper relative motion and attitude for the deflective action to take place. An optimal deflection strategy is often wanted and found by means of constrained optimization techniques [35] in which important factors are considered for the mission to be feasible, efficient and

reliable (e.g., power and mass budgets, data uncertainties, targeted deflection). Optimization techniques rely on a parametric model of the problem and they are the heart of today's design process allowing its analysis within predefined boundaries, under particular constraints and performance metrics.

Orbital Deflection Model

The orbital deflection model aims to describe how the target's state vector changes, at a certain epoch in time, due to the previously applied LTA. Such action is acting for a finite amount of time that goes from the interception instant (i.e., interception epoch, t_i $[s]$), when the chaser is at the nominal position to operate at the target, to a final instant (i.e., cut-off epoch, t_{co} $[s]$), when the chaser ceases to operate. The cut-off epoch can be either before or at the close-passage/impact epoch with a third body (e.g., the Earth, an SSSB, another SC), referred from now on as Impacted Object (IO).

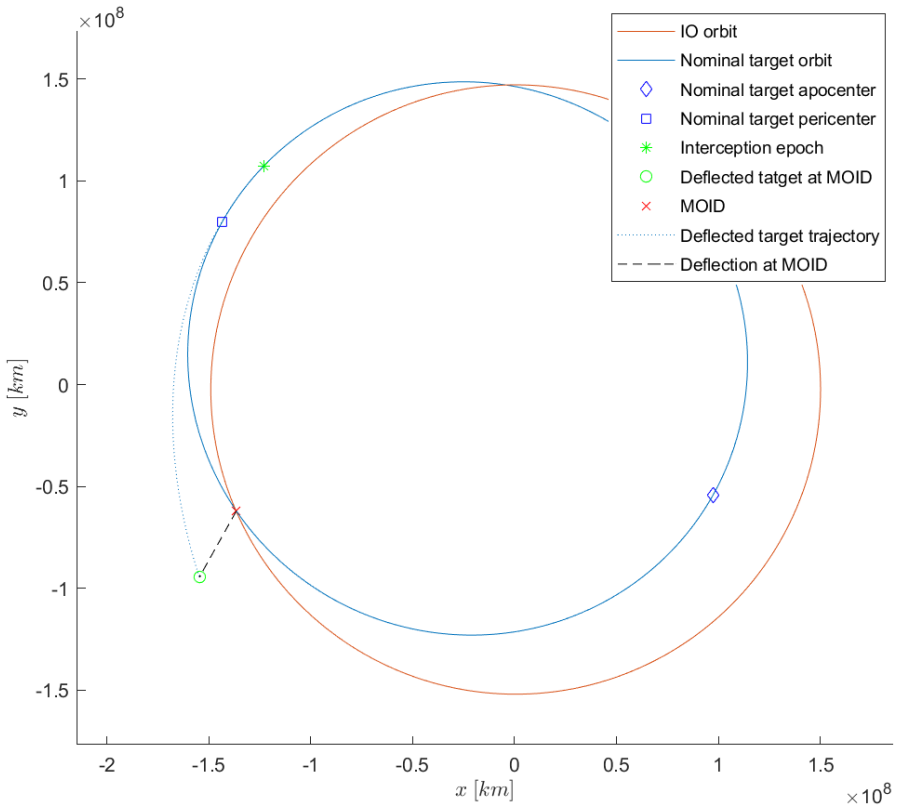

Figure 2.4: *Representation of a low-thrust orbital deflection showing: the orbit of IO object, the target interception point, the MOID point, the deflected target orbit, the deflection vector at MOID, and the nominal target absidial points.*

Figure 2.4 shows the IO, nominal target and deflected target trajectories. The close-passage/impact with IO can only happen when the target is close/at the MOID, defined as the minimum geometric distance between IO's orbit and the target one. The MOID conditions are obtained propagating in time the considered bodies motions, searching for such minima. In general, the MOID conditions are evolving in time due to presence of perturbations, high MOID conditions fidelity is out of the scope of the current dissertation and thus, the unperturbed R2BP model is used to compute them.

The state vector of the deflected target can be found proceeding with a direct integration of equation 2.6 with the applied LTA time profile, from interception up until MOID epoch and then evaluate its deviation from the nominal state vector. Due to the LTA expected small magnitude, the perturbed orbit can be considered to be proximal to the unperturbed one. Under this assumption, it is often adopted either a semi-analytical or an analytical approach [66, 67, 36], aiming to reduce the computational effort of the propagation.

However, the approach followed in the dissertation is fully numerical, and involves the propagation of the target's state using Gauss' planetary equations. These describe the evolution of the target's KEP elements due to a generic perturbation, here written in NTH components, and are defined as

$$\begin{cases} \dot{a} = \frac{2a^2 v}{\mu_1} a_t \\ \dot{e} = \frac{1}{v}\left[2(e+\cos(\theta))a_t - \frac{r}{a}\sin(\theta)a_n\right] \\ \dot{i} = \frac{r\cos(\theta+\omega)}{h\sin(i)} a_h \\ \dot{\Omega} = \frac{1}{ev}\left[2\sin(\theta)a_t + \left(2e + \frac{r}{a}\cos(\theta)a_n\right)\right] - \frac{r\sin(\theta+\omega)\cos(i)}{h\sin(i)} a_h \\ \dot{M} = n - \frac{b}{eav}\left[2\left(1+\frac{e^2 r}{p}\right)\sin(\theta)a_t + \frac{r}{a}\cos(\theta)a_n\right] \\ \underline{KEP}(t_0) = \underline{KEP}_0 \\ {}^{\mathcal{N}}\underline{a}_p(t) = [a_t(t), a_n(t), a_h(t)]^T \end{cases} \tag{2.20}$$

where $b \triangleq a\sqrt{1-e^2}$ $[km]$ is the orbital semi-minor axis, $p \triangleq h^2/\mu_1$ is the orbital semilatus rectum, $\underline{KEP}_0$ is the initial KEP vector of the target, and ${}^{\mathcal{N}}\underline{a}_p$ is the perturbing acceleration vector acting on the target, written in NTH components.

Given the LTA time profile acting on the target, equations (2.20) are integrated from

interception to MOID epoch and the achieved deflection is computed as

$$\begin{cases} {}^{\mathcal{J}}\underline{dr}_{T}(t_{moid}) & = {}^{\mathcal{J}}\underline{R}_{T}(t_{moid}) - {}^{\mathcal{J}}\underline{R}_{nT}(t_{moid}) \\ {}^{\mathcal{J}}\underline{R}_{T}(t_{moid}) & = \mathbf{R}^{T}_{I\to P}(t_{moid}) \left(\frac{\bar{p}}{1+\bar{e}\cos(\bar{\theta})} \left[\cos(\bar{\theta}), \sin(\bar{\theta}), 0\right]^{T} \right) \\ \mathbf{R}_{I\to P}(t_{moid}) & = \begin{bmatrix} \cos(\bar{\omega}) & \sin(\bar{\omega}) & 0 \\ -\sin(\bar{\omega}) & \cos(\bar{\omega}) & 0 \\ 0 & 0 & 1 \end{bmatrix} \begin{bmatrix} 1 & 0 & 0 \\ 0 & \cos(\bar{i}) & \sin(\bar{i}) \\ 0 & -\sin(\bar{i}) & \cos(\bar{i}) \end{bmatrix} \begin{bmatrix} \cos(\bar{\Omega}) & \sin(\bar{\Omega}) & 0 \\ -\sin(\bar{\Omega}) & \cos(\bar{\Omega}) & 0 \\ 0 & 0 & 1 \end{bmatrix} \end{cases} \tag{2.21}$$

where ${}^{\mathcal{J}}\underline{R}_{nT}(t_{moid})$ is the nominal target's position vector at MOID epoch, ${}^{\mathcal{J}}\underline{R}_{T}(t_{moid})$ the deflected target's position vector at MOID epoch, and $\underline{KEP}(t_{moid}) = \left[\bar{a}, \bar{e}, \bar{i}, \bar{\Omega}, \bar{\omega}, \bar{\theta}\right]$ is the result of equations (2.20) integration.

2.5 Gravitational tug

This section presents the key concepts of the gravitational tug technique, and aims to understand how the achieved LTA, acting on the target, can be described and used with the deflection model presented in section 2.4. As discussed in section 1.1.2, there are many ways to implement a GT. In this work, the non-inertial hovering approach is chosen as a basis for the development of the proposed model, aiming to answer the dissertation's questions presented in section 1.3. Nevertheless, the introduced concepts can be extended to other GT approaches.

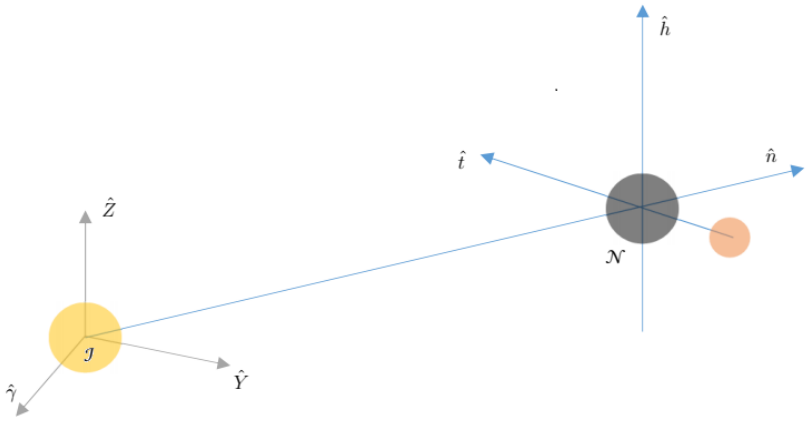

Figure 2.5: *Non-inertial hovering approach scheme*

Considering the target-chaser close system represented in figure 2.5, the GT exploits the chaser's AOCS to generate an external action (i.e., thrust, T_n) able to counterbalance the gravitational pull of the target and, thus, creating an artificial equilibrium point at which the chaser can be maintained (i.e., hovering distance or hovering point, d $[m]$) for a specific amount of time (i.e., total tugging time, t_{tug} $[s]$). Being such action an external force, it is seen as a linear momentum exchange with the target or, equivalently, as a towing force (i.e., tugging force, F_{GT} $[N]$) acting on the target itself [56].

Considering the chaser's AOCS, a GT is feasible only if the following requirements are met

1. **Requirement of Tug Sustainability (RTS)**
   The propulsive subsystem shall be able to generate the proper amount of thrust capable of maintaining the chaser at a certain hovering distance, for a given total tugging time.

2. **Requirement of Non-Impingement (RNI)**
   The expelled mass used to generate thrust shall not impact the target's surface. Otherwise, the result would be the generation of a target-chaser system internal force, according to action-reaction principle, and thus no net action on the system's CM.

Neglecting the heliocentric motion of the objects and using equation (2.6) to describe the chaser's dynamics in the target's gravitational field, the required force to maintain a generic hovering position (i.e., equilibrium position) is

$$\underline{F}_{GT} \equiv \underline{F}_{hover} \triangleq \underline{a}_c m_C = \frac{\mu_T \, m_C}{r^3} \underline{r} = G \, \frac{m_T \, m_C}{r^3} \underline{r} \tag{2.22}$$

where μ_T $[km^3/s^2]$ is the gravitational constant of the target, m_C $[kg]$ is the mass of the chaser, and m_T $[kg]$ is the mass of the target.

Equation (2.22) shows that the required hovering force is always pointing away from the target, along the radial direction. As a consequence, the RNI fulfilment is granted only if $\underline{F}_{hover}$ is obtained as a vectorial sum of multiple thrusting devices. The most common approach in literature [55, 56, 59, 35] is to adopt multiple ion engines with canted nozzles in a symmetric configuration.

Referring to figure 2.6, a canted pair of nozzles is defined as a set of two nozzles inclined in respect to a common direction by an angle β_i $[deg]$ (i.e., the cant angle)

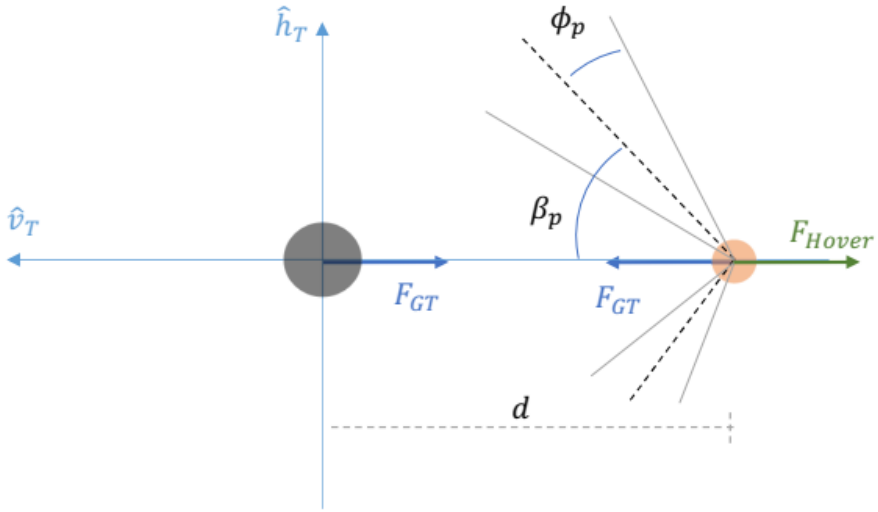

Figure 2.6: *Canted pair of nozzles in a symmetric configuration seen by the NTH frame, centred at the target.*

and characterised by exhaust cones (i.e., ejected mass envelopes) of known semi-amplitudes ϕ_i $[deg]$. The canted pair is symmetric if $\beta_1 = \beta_2 \triangleq \beta_p$ and $\phi_1 = \phi_2 \triangleq \phi_p$

Given a symmetric canted pair of nozzles with fixed geometry, the minimum hovering distance under RNI requirement is

$$d_{min} = \frac{R_T}{\sin\left(\beta_p - \phi_p\right)} \tag{2.23}$$

where R_T $[m]$ is the target equivalent radius.

The minimum hovering distance [48] is associated to a configuration in which the exhaust cones are tangent to the sphere of radius R_T, centred at the target's CM.

Such condition is referred, from now on, as adapted canted nozzles configuration.

Assuming a priori an adapted canted nozzles configuration, $\underline{F}_{hover}$ can also be written as

$$\begin{cases} \underline{F}_{hover} = T_n \, \eta_{th}\left(r\right) \hat{r} \\ \eta_{th} = \cos\left(\arcsin\left(\frac{R_T}{r}\right) + \phi_p\right) \end{cases} \tag{2.24}$$

where T_n $[N]$ is the total thrust generated by the chaser's PS, R_T is the target's equivalent radius, ϕ_p $[deg]$ is the exhaust cone's half angle, and η_{th} $[-]$ is the thrust ef-

ficiency that describes the degradation of the generated thrust due to cosine losses introduced by RNI.

Equation (2.24) shows the existence of a relative hovering distance d_{RNIL} $[m]$ where the thrust efficiency can become zero. This is caused by the RNI satisfaction, and implies that no thrust can be produced to counteract the local gravitational mutual attraction. As a result, the GT hovering position shall be

$$d > d_{RNIL} = \frac{R_T}{\sin\left(\frac{\pi}{2} - \phi_p\right)} \tag{2.25}$$

Assuming to start the hover at a given relative distance d, the generation of the equilibrium thrust $\underline{F}_{hover}$ reduces the chaser mass according to the equation (2.14). As a consequence, the equilibrium condition is lost and can be re-established either reducing d with the same F_{th}, or adopting a constant d with a reduced F_{th}. Keeping d constant leads to a smaller thrust level, which implies lower fuel consumption and higher chaser's dry mass for a fixed overall mass at interception m_{C0}. This is translated into a higher achievable maximum thrust and thus to the possibility of a smaller d. Iterating this process, it is possible to find an optimal initial hovering point [35] that makes the constant option more efficient than the variable one, for a given m_{C0}.

Assuming to use a PS composed by adapted pair of nozzles with a common specific impulse, combining equations (2.22) and (2.24), and solving equation (2.14) with a constant relative hovering distance, the chaser's mass time variation is

$$m_C = m_C(t) = m_C(t_i) \exp\left(-\frac{G\, m_T}{d^2\, \eta_{th}\,(d)} \frac{(t - t_i)}{Isp\, g_0}\right) \tag{2.26}$$

Recalling equation (2.12) and assuming that all the onboard fuel is used to maintain the GT, the hovering distance that is satisfying both RTS and RNI requirements (i.e., d_{GT}) is found to be the solution of

$$F_{GT}(t_i, d_{GT}) \equiv G\, \frac{m_T\, m_{C0}}{(d_{GT})^2} = \frac{m_C(t_{co})}{2} \frac{\xi_{th}}{\tau_{pw}} \eta_{th}\,(d_{GT}) \equiv T_n \eta_{th}(d_{GT}) \tag{2.27}$$

which can be rewritten using equation 2.26 and the η_{th} definition as

$$G\, \frac{m_T}{(d_{GT})^2} = \frac{\exp\left(-\frac{G\, m_T}{d^2\, \eta_{th}(d)} \frac{(t_{co} - t_i)}{Isp\, g_0}\right)}{2} \frac{\xi_{th}}{\tau_{pw}} \cos\left(\arcsin\left(\frac{R}{d_{GT}}\right) + \phi_p\right) \tag{2.28}$$

Once equation 2.28 is solved (e.g., using numerical methods), the acceleration felt by the target can be written in the target's NTH frame as

$$ {}^{\mathcal{N}}\underline{a}_T = {}^{\mathcal{N}}\underline{a}_T(t) = \frac{{}^{\mathcal{N}}\underline{F}_{hover}(t)}{m_T} = G\,\frac{m_C(t)}{(d_{GT})^2}\,{}^{\mathcal{N}}\hat{r} \tag{2.29} $$

where ${}^{\mathcal{N}}\hat{r}$ is the hovering position unit vector written in the NTH frame of the target.

The deflection from nominal target, at MOID epoch, is then computed using equations (2.21) with the result of (2.20) when (2.29) is considered.

Note that the solution of equation (2.28) is not depending upon the chaser's mass at interception, and equation (2.29) is valid for a generic tugging direction (e.g., tangential tug represented in figures 2.6 and 2.5).

2.6 Rigid body dynamics

This section introduces some concepts that are later used to develop the target-chaser translational and rotational dynamic model, used to asses the performance of the GMT in case of a target with a generic tumbling state.

2.6.1 Translational and rotational dynamics

Let G be the CM of a rigid object located at a given position in the inertial frame $\mathcal{I}$. The trajectory of G is determined by Newton's law of motion as

$$ \begin{cases} {}^{\mathcal{I}}\ddot{\underline{R}}_G = \dfrac{{}^{\mathcal{I}}\underline{F}_{Ext}}{m} \\ {}^{\mathcal{I}}\dot{\underline{R}}_G(0) = {}^{\mathcal{I}}\underline{V}_{G,0} \\ {}^{\mathcal{I}}\underline{R}_G(0) = {}^{\mathcal{I}}\underline{R}_{G,0} \end{cases} \tag{2.30} $$

where m is the mass of the body, ${}^{\mathcal{I}}\underline{F}_{Ext}$ is the resultant of all the external inertial forces acting on it, and ${}^{\mathcal{I}}\underline{V}_{G,0}$ and ${}^{\mathcal{I}}\underline{R}_{G,0}$ are the initial conditions in velocity and position for such second order ODE.

Let G be also the centre of a body fixed frame $\mathcal{B}$ attached to the object and aligned with its principal axes of inertia. The relative orientation of $\mathcal{B}$ with respect to $\mathcal{I}$ evolves in time according to Euler's equation as

$$\begin{cases} \mathbf{J}\,{}^{\mathcal{B}}\underline{\dot{\omega}}_{\mathcal{BI}} + \dot{\mathbf{J}}\,{}^{\mathcal{B}}\underline{\omega}_{\mathcal{BI}} + \left[{}^{\mathcal{B}}\underline{\omega}_{\mathcal{BI}}\right]^{\wedge}\mathbf{J}\,{}^{\mathcal{B}}\underline{\omega}_{\mathcal{BI}} = {}^{\mathcal{B}}\underline{T}_{ext} + {}^{\mathcal{B}}\underline{T}_{as} \\ \dot{\mathbf{T}}_{\mathcal{I}\to\mathcal{B}} = -\left[{}^{\mathcal{B}}\underline{\omega}_{\mathcal{BI}}\right]^{\wedge}\mathbf{T}_{\mathcal{I}\to\mathbf{B}} \\ {}^{\mathcal{B}}\underline{\omega}_{\mathcal{BI}}(0) = {}^{\mathcal{B}}\underline{\omega}_{\mathcal{BI},0} \\ \mathbf{T}_{\mathcal{I}\to\mathbf{B}}(0) = \mathbf{T}_{\mathcal{I}\to\mathbf{B},0} \end{cases} \tag{2.31}$$

where $\mathbf{T}_{\mathcal{I}\to\mathbf{B}}$ is the direction cosine matrix used to express the kinematics, ${}^{\mathcal{B}}\underline{\omega}_{\mathcal{BI}}$ is the angular velocity of the object, $\mathbf{J}$ is the diagonal matrix of principal moments of inertia, ${}^{\mathcal{B}}T_{ext}$ is the external net torque acting, ${}^{\mathcal{B}}T_{as}$ is the torque arising from internal angular momentum storing devices (e.g., reaction wheels, controlled moment gyro) that may be present when the object has some sort of angular momentum management capability, and ${}^{\mathcal{B}}\underline{\omega}_{\mathcal{BI},0}$ and $\mathbf{T}_{\mathcal{I}\to\mathbf{B},0}$ are the initial angular velocity and attitude for such system of ODE.

2.6.2 Relative translational dynamics in non-inertial frames

Let P be an object in motion within an inertial frame $\mathcal{I}$. Considering a non-inertial moving frame $\mathcal{L}$ centred at the generic point O, the relative position vector of P in respect to O is

$${}^{\mathcal{I}}\underline{r}_{P-O} = {}^{\mathcal{I}}\underline{R}_{P} - {}^{\mathcal{I}}\underline{R}_{O} \tag{2.32}$$

It is possible to prove [60] that the velocity of P with respect to O seen by an inertial observer is linked to the one seen by an observer moving with $\mathcal{L}$ as

$$\begin{cases} {}^{\mathcal{I}}\underline{\dot{r}}_{P-O} & = {}^{\mathcal{I}}\underline{\dot{s}} + \left[{}^{\mathcal{I}}\underline{\Omega}_{\mathcal{LI}}\right]^{\wedge}{}^{\mathcal{I}}\underline{s} \\ {}^{\mathcal{I}}\underline{s} & \triangleq {}^{\mathcal{I}}\underline{r}_{P-O} \end{cases} \tag{2.33}$$

where ${}^{\mathcal{I}}\underline{\Omega}_{\mathcal{LI}}$ is the angular velocity of frame $\mathcal{L}$ with respect to $\mathcal{I}$ written in the latter's components, and ${}^{\mathcal{I}}\underline{\dot{s}}$ and ${}^{\mathcal{I}}\underline{s}$ are the relative position and relative velocity seen by $\mathcal{L}$ observer, written in $\mathcal{I}$ components.

Being $\mathbf{T}_{\mathcal{I}\to\mathcal{L}}$ the transformation matrix that projects a generic vector from $\mathcal{I}$ to $\mathcal{L}$, it is possible to rewrite equation (2.33) in frame $\mathcal{L}$ components as

$$
\begin{aligned}
{}^{\mathcal{I}}\underline{\dot{r}}_{P-O} = \mathbf{T}^{T}_{\mathcal{I}\to\mathcal{L}}\left({}^{\mathcal{L}}\underline{\dot{s}} + \left[{}^{\mathcal{L}}\underline{\Omega}_{\mathcal{L}\mathcal{I}}\right]^{\wedge}{}^{\mathcal{L}}\underline{s}\right) \to \\
\to {}^{\mathcal{L}}\underline{\dot{r}}_{P-O} = \mathbf{T}_{\mathcal{I}\to\mathcal{L}}\,{}^{\mathcal{I}}\underline{\dot{r}}_{P-O} = {}^{\mathcal{L}}\underline{\dot{s}} + \left[{}^{\mathcal{L}}\underline{\Omega}_{\mathcal{L}\mathcal{I}}\right]^{\wedge}{}^{\mathcal{L}}\underline{s}
\end{aligned}
\tag{2.34}
$$

Following the same steps, the acceleration of P with respect to O seen by an inertial observer is linked to the one seen by an observer moving with $\mathcal{L}$ as

$$
{}^{\mathcal{L}}\underline{\ddot{r}}_{P-O} = {}^{\mathcal{L}}\underline{\ddot{s}} + 2\left[{}^{\mathcal{L}}\underline{\Omega}_{\mathcal{L}\mathcal{I}}\right]^{\wedge}{}^{\mathcal{L}}\underline{\dot{s}} + \left[{}^{\mathcal{L}}\underline{\dot{\Omega}}_{\mathcal{L}\mathcal{I}}\right]^{\wedge}{}^{\mathcal{L}}\underline{s} + \left[{}^{\mathcal{L}}\underline{\Omega}_{\mathcal{L}\mathcal{I}}\right]^{\wedge}\left[{}^{\mathcal{L}}\underline{\Omega}_{\mathcal{L}\mathcal{I}}\right]^{\wedge}{}^{\mathcal{L}}\underline{s} \tag{2.35}
$$

where ${}^{\mathcal{L}}\underline{\ddot{s}}$ is the relative acceleration seen by $\mathcal{L}$ observer written in the same frame components and ${}^{\mathcal{L}}\underline{\dot{\Omega}}_{\mathcal{L}\mathcal{I}}$ is the angular acceleration of frame $\mathcal{L}$ with respect to $\mathcal{I}$.

2.6.3 Osculating cinematic relations

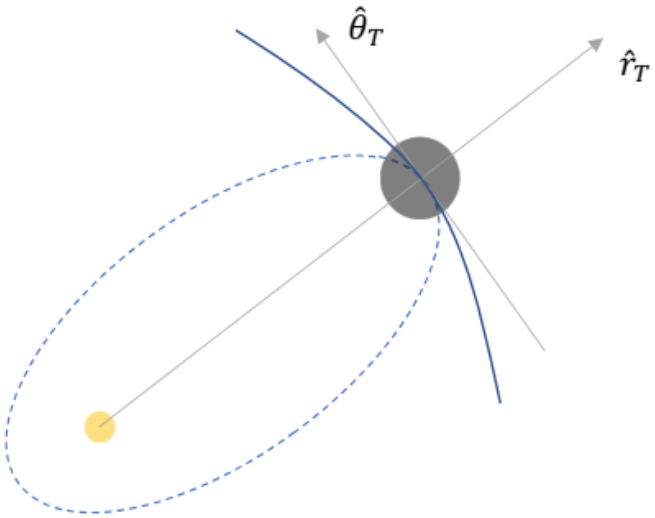

Figure 2.7: *Non Keplerian motion and osculating orbit of an object about a primary.*

Given an objects' state vector relative to a primary body at a certain epoch, represented in figure 2.7, the osculating orbit about the primary is defined as the fictitious Keplerian orbit that has the same state vector relative to the primary itself, at the given epoch. It is possible to construct the osculating frames $\tilde{\mathcal{L}}$ and $\tilde{\mathcal{N}}$, and use them to retrieve the instantaneous angular velocities and accelerations of such

frames with respect to $\mathcal{I}$.

Recalling equation 2.9, the instantaneous angular velocity vector of $\tilde{\mathcal{L}}$ with respect to $\mathcal{I}$ is computed as

$$\begin{cases} {}^{\tilde{\mathcal{L}}}\underline{\Omega}_{\tilde{L}I} = {}^{\tilde{\mathcal{L}}}\underline{\Omega}_{\tilde{L}I}(t) = \begin{bmatrix} 0 \\ 0 \\ \dot{\theta}(t) \end{bmatrix} \\ \dot{\theta} = \dot{\theta}(t) = (e\cos(\theta)+1)^2 \sqrt{-\frac{\mu_p}{a^3\left(e^2-1\right)^3}} \end{cases} \tag{2.36}$$

where the object's osculating KEP elements are used to compute the rate of change of the osculating true anomaly, and ${}^{\tilde{\mathcal{L}}}\underline{\Omega}_{\tilde{L}I}$ is conveniently written in $\tilde{\mathcal{L}}$ frame components.

The instantaneous angular acceleration vector of $\tilde{\mathcal{L}}$ with respect to $\mathcal{I}$ is computed performing the time derivative of equation (2.36), and it can be written as

$$\begin{cases} {}^{\tilde{\mathcal{L}}}\dot{\underline{\Omega}}_{\tilde{L}I} = {}^{\tilde{\mathcal{L}}}\dot{\underline{\Omega}}_{\tilde{L}I}(t) = \begin{bmatrix} 0 \\ 0 \\ \ddot{\theta}(t) \end{bmatrix} \\ \ddot{\theta} = \ddot{\theta}(t) = \frac{2\,e\,\mu_p \sin(\theta)\,(e\cos(\theta)+1)^3}{a^3\left(e^2-1\right)^3} \end{cases} \tag{2.37}$$

Considering frame $\tilde{\mathcal{N}}$, it can be linked to $\tilde{\mathcal{L}}$ recalling that the former is defined by the velocity vector angle in respect to the osculating local horizontal direction (i.e., osculating flight path angle, γ $[deg]$).

Using the Keplerian orbit theory [60], the osculating flight path angle γ can be defined as

$$\gamma = \gamma(t) = \operatorname{atan}\left(\frac{e\sin(\theta(t))}{e\cos(\theta(t))+1}\right) \tag{2.38}$$

Equation (2.38) is derived in time and after some manipulations, using equations (2.37) and (2.36), the rate of change of the flight path angle can be expressed in terms of osculating Keplerian parameters as

$$\dot{\gamma} = \dot{\gamma}(t) = \frac{e\,\dot{\theta}(t)\;(e+\cos(\theta(t)))}{e^2+2\cos(\theta(t))\;e+1} \tag{2.39}$$

Equation (2.39) can further be derived in time to obtain

$$\begin{aligned}\ddot{\gamma} = \ddot{\gamma}(t) = &\Big[\ddot{\theta}(t)\ e^3 + 3\,\ddot{\theta}(t)\ e^2\cos(\theta(t)) + \sin(\theta(t))\ e^2\,\dot{\theta}(t)^2 \\ &+ 2\,\ddot{\theta}(t)\ e\cos(\theta(t))^2 + \ddot{\theta}(t)\ e + \ddot{\theta}(t)\ \cos(\theta(t)) \\ &- \sin(\theta(t))\ \dot{\theta}(t)^2\Big]\ \frac{e}{(e^2 + 2\cos(\theta(t))\ e + 1)^2}\end{aligned} \tag{2.40}$$

Recalling that $\tilde{\mathcal{N}}$ is obtained performing a clockwise rotation of $\tilde{\mathcal{L}}$ about its third axis, by the γ angle, the instantaneous angular velocity and acceleration vectors of $\tilde{\mathcal{N}}$ with respect to $\mathcal{I}$ are defined as

$$\begin{aligned}{}^{\tilde{\mathcal{N}}}\underline{\Omega}_{\tilde{N}I} &= {}^{\tilde{\mathcal{N}}}\underline{\Omega}_{\tilde{N}I}(t) = \begin{bmatrix} 0 \\ 0 \\ \dot{\theta}(t) - \dot{\gamma}(t) \end{bmatrix} \\ {}^{\tilde{\mathcal{N}}}\underline{\dot{\Omega}}_{\tilde{N}I} &= {}^{\tilde{\mathcal{N}}}\underline{\dot{\Omega}}_{\tilde{N}I}(t) = \begin{bmatrix} 0 \\ 0 \\ \ddot{\theta}(t) - \ddot{\gamma}(t) \end{bmatrix}\end{aligned} \tag{2.41}$$

2.7 Summary

This chapter presented all the mathematical tools that are used in chapter 2 to develop the GMT model, to design the chaser that performs the GMT, to predict its performance in terms of achieved deflection at MOID, to perform the model sensitivity analysis, and to study how the target's tumbling state is affecting the performance of a chaser designed using the proposed approach.

Chapter 3

Gravitational-magnetic tug

This chapter presents the performed investigations, the dynamic GMT model developed, and a series of test cases. General assumptions valid throughout the entire dissertation are stated in section 3.1. Section 3.2 discusses the analysis performed to identify the conditions for which the gravitational and magnetic contributions can efficiently cooperate, considering the objects' relative distance and their dipoles' orientations, with the aim of increasing the LTA imparted on the target. In section 3.3, the GMT model is developed, the optimal relative hovering position problem is studied, the achieved deflection at MOID is estimated, and the sensitivity analysis with respect to a selected group of parameters is carried out. This is done considering a GMT that operates using three different tugging modes, and for a special case that is not affected by the target's tumbling state. Section 3.4 presents the target-chaser relative dynamic model that describes the translational and rotational motions of the objects. This is used to evaluate the chaser's controllability effort and the achieved target deflection at MOID conditions, when the target is characterised by a generic tumbling state, and it is exposed to the gravitational-magnetic interaction of a chaser designed as proposed in the GMT model.

3.1 General assumptions

To answer the thesis objective presented in section 1.3 the discussion is contextualized for a NEO (i.e., target) orbiting the Sun, in course of impact with the planet Earth (i.e., IO). It is assumed that

1. The target has a spherical shape equal to the mean radius of the considered object, a uniform constant density, a uniform global magnetisation state, a constant volume and a simple tumbling motion about one inertially fixed axis. No magnetosphere, nor any other mechanisms that may alter the body magnetisation state are present.

2. The chaser is a homogeneous spherical SC with known initial mass at interception epoch, equipped with a Superconductive Magnets Subsystem (SMS) capable of generating a magnetic dipole moment in any direction of space, regardless the chaser's attitude. It is equipped with an AOCS composed by a set of ion thrusters with known performance and fixed geometry. Furthermore, the onboard PGS is assumed to have a known and fixed efficiency.

3. The mutual magnetic intraction between the chaser and the target can be approximated by the far-field equations (2.19).

4. The chaser performs the tugging action from interception up until MOID epoch.

5. The target and IO are at their MOID true anomaly at MOID epoch.

6. The transfer from planet Earth to the target is not taken into account. For instance, the chaser is considered as a payload of an interplanetary transfer vehicle whose mission design and optimisation is out of scope for the dissertation.

7. It is assumed that the reference GT is achieved performing a non-inertial hovering of the target, along its velocity vector and in such a way that its orbital energy is reduced (i.e., hovering behind the target).

A tangential LTA is often considered the optimal approach to deflect an object with high warning time [68], and it is here assumed as a reference case only, focusing on the possible improvement that a magnetic interaction would introduce. The presented concepts may be applied to a generic optimal LTA direction and may be extended to a space debris target, these are not covered in the dissertation. Furthermore, additional assumptions and considerations are stated at the beginning of each section.

3.2 Static analysis

The primary goal of the static analysis is to compare the LTA obtained with the gravitational and magnetic interactions (i.e., actors), without considering the actual motion the objects, and identify the conditions for which the cooperation between them is optimal. The object's motion about the primary is later taken into account in section 3.4. Sections 3.2.1, 3.2.2 estimate the order of magnitude of the acceleration felt by the target, when both actors are considered. Section 3.2.3 compares the LTA of both actors for a special relative orientation of the objects' dipoles, identifies the minimum magnetic dipole that the chaser would need to generate in order to consider the actors' cooperation, and select a test target among the identified one presented

in table 1.1. Section 3.2.4 studies how the relative orientation of the objects' dipoles is affecting the magnetic interaction, and proposes two approaches to maximize the cooperation between the actors, when the target tumbling state is considered.

3.2.1 Low thrust action relative increment estimation

Figure 3.1 shows the isolated system composed by the target and the chaser interacting with gravitational and magnetic forces.

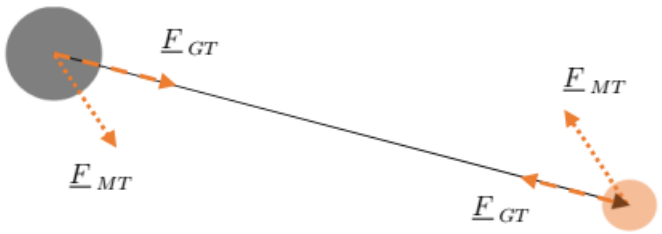

Figure 3.1: *Target-chaser isolated system*

Recalling equations (2.29) and (2.19), the net acceleration experienced by the target is obtained as the vectorial sum of the gravitational and magnetic interaction

$$\underline{a}_{T,GMT} = \frac{\underline{F}_{GMT}}{m_T} = \frac{\underline{F}_{C\to T,GT} + \underline{F}_{C\to T,MT}}{m_T} \tag{3.1}$$

where the gravitational contribution is always aligned with the relative position vector, whereas the magnetic one can act in any direction of space, being highly dependant upon the objects' dipoles relative orientations and relative position.

Given that the reference GT is acting to induce an acceleration aligned with the velocity vector of the target, the relative increment in induced tangential acceleration introduced by the GMT is found using equations (2.24) and (2.19) in equation (3.1), and projecting along the relative position vector.

This is proportional to

$$\frac{\underline{a}_{T,GMT}\cdot\underline{r} - \underline{a}_{T,GT}\cdot\underline{r}}{\underline{a}_{T,GT}\cdot\underline{r}} \propto K\left(\hat{\mu}_{\epsilon\mu,T}, \hat{\mu}_{\epsilon\mu,C}\right)\frac{\mu_{\epsilon\mu,T}\mu_{\epsilon\mu,C}}{m_T m_C}\frac{1}{d^2} \tag{3.2}$$

where K is a coefficient that describes the amount of magnetic acceleration that is actually acting along the same direction as gravity and depends upon the objects' magnetic dipoles orientations.

Equation 3.2 shows that, for a given distance, the increment is proportional to the specific magnetic moments of both target and chaser, and it is inversely proportional to the square of the hovering distance. The target's Specific Magnetic Moment (SMM) (i.e., $\mu_{\epsilon\mu_T}/m_T$) is a constant estimated through previous measurements and affected by uncertainties, whereas the chaser's SMM (i.e., $\mu_{\epsilon\mu_C}/m_C$) can be considered as a design parameter, together with the hovering distance, and it is a time varying quantity due to the fuel mass consumption required for the SC to operate.

3.2.2 Order of magnitude of the magnetic interaction

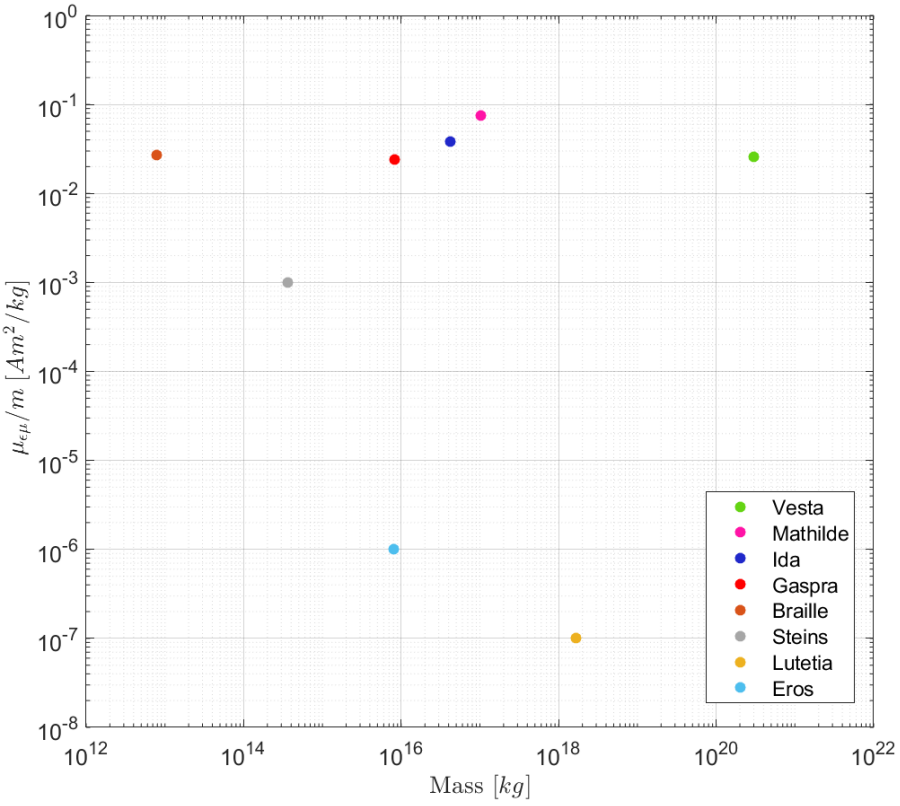

Figure 3.2: *Specific magnetic dipole of the identified asteroids as a function of their mass*

Figure 3.2 shows the estimated maximum SMMs of the available set of NEOs identified in table 1.1. The typical order of magnitude is close to 10^{-2} $[Am^2/kg]$ but it can be as low as 10^{-6} $[Am^2/kg]$. Considering a chaser with a net mass of 1.5 $[ton]$, equipped with a magnetic torquer subsystem that can create a magnetic dipole with an order of magnitude of 10^3 $[Am^2]$ [69], the order of magnitude of its specific magnetic dipole

is 10^{-1} $[Am^2/kg]$. Taking as a reference the target with minimum equivalent radius (i.e., Braille, 800 $[m]$), a unitary K coefficient, and a hovering distance of 500 $[m]$ above the target's surface, the resulting increment in acceleration is estimated using equation 3.2 to have an order of magnitude of 10^{-9}. On the other hand, imposing the same hovering distance and a relative increment of 50% in target's acceleration, the order of magnitude of the required chaser's magnetic dipole would be 10^7 $[Am^2]$ (i.e., 10^4 $[Am^2/kg]$).

The generation of such large magnetic dipole could be possible using a system that exploits a superconducting material, cooled below a critical temperature to reduce the heat generation due to Joule effect [51]. This requires the development of new technologies, or the adaptation of already existing ones, designed ad-hoc and tested for space applications. The dissertation aims to drive such need, understanding the conditions that would need to be maintained if the magnetic interaction is exploited in order to effectively improve a traditional GT, and estimating the chaser's system requirements (e.g., SMS efficiency, AOCS workload) to do so.

3.2.3 Gravitational-magnetic tug interaction as function of the hovering distance

The analysis aims to compare the LTA achieved on the target, when the gravitational and magnetic contributions are considered, as function of the hovering distance d. To proceed, it is assumed a simplified case where the objects dipoles and the relative position vector are co-aligned, pointing in the same direction. This represents the optimal relative configuration that allows to maximize the magnetic interaction force, for a given pair of dipoles, and it is found by inspection of equation (2.19).

Figure 3.3 shows a schematic representation of this configuration. It is worth to mention that the target's tumbling state is not included in the current analysis, and it is later taken into consideration in section 3.2.4.

Referring to the target, the angular momentum conservation is trivially satisfied being the magnetic torque null for the chosen configuration (see equation (2.17)), whereas the linear momentum conservation is reduced to the radial component only and leads to

$$\begin{cases} a_{T,GMT} = \dfrac{F_{GMT}}{m_T} = G\dfrac{m_C}{d^2} + K\dfrac{\mu_{\epsilon\mu_T}}{m_T}\dfrac{\mu_{\epsilon\mu_C}}{d^4} \\ K \triangleq \dfrac{6}{4}\dfrac{\mu_{\epsilon\mu_0}}{\pi} \end{cases} \tag{3.3}$$

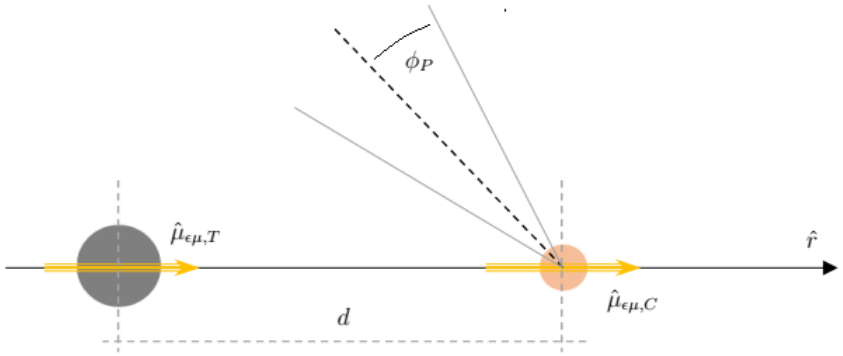

Figure 3.3: *Target-chaser relative dipoles orientation for tugging force sensitivity to hovering distance*

where K [−] is referred from now on as the relative orientation coefficient.

As discussed in section 2.5, the RNI is introducing a degradation of the total generated thrust achievable by the chaser PS. The minimum hovering distance d_{RNIL} defined by equation (2.25) is the limit for the current analysis, and it is dependant upon only the target's equivalent radius R_T and the exhaust cone's half angle ϕ_p.

Equation 3.3 shows that the resulting GMT acceleration is asymptotic to the one of a pure Magnetic Tug (MT) for small hovering distance, whereas it is asymptotic to the pure GT for high ones. Figure 3.4 underlines such behaviour for the considered test case presented in table 3.1 and points out the presence of a Break Even Point (BEP) close to which, the contribution of MT has the same order of magnitude as the GT. Operating close to the BEP location allows the LTA to be the result of a cooperation between the gravitational and magnetic contributions, rather than the result of one surmounting the other.

R_T	800	m	$m_C(t_i)$	1500	kg
ρ_T	3900	kg	Isp	3100	s
$\mu_{\epsilon\mu_T}/m_T$	0.0251	Am^2/kg	ϕ_P	20	deg
			$\mu_{\epsilon\mu_C}/m_C$	10^5	Am^2/kg

Table 3.1: *Target and chaser reference data for the GMT interaction as function of the hovering distance.*

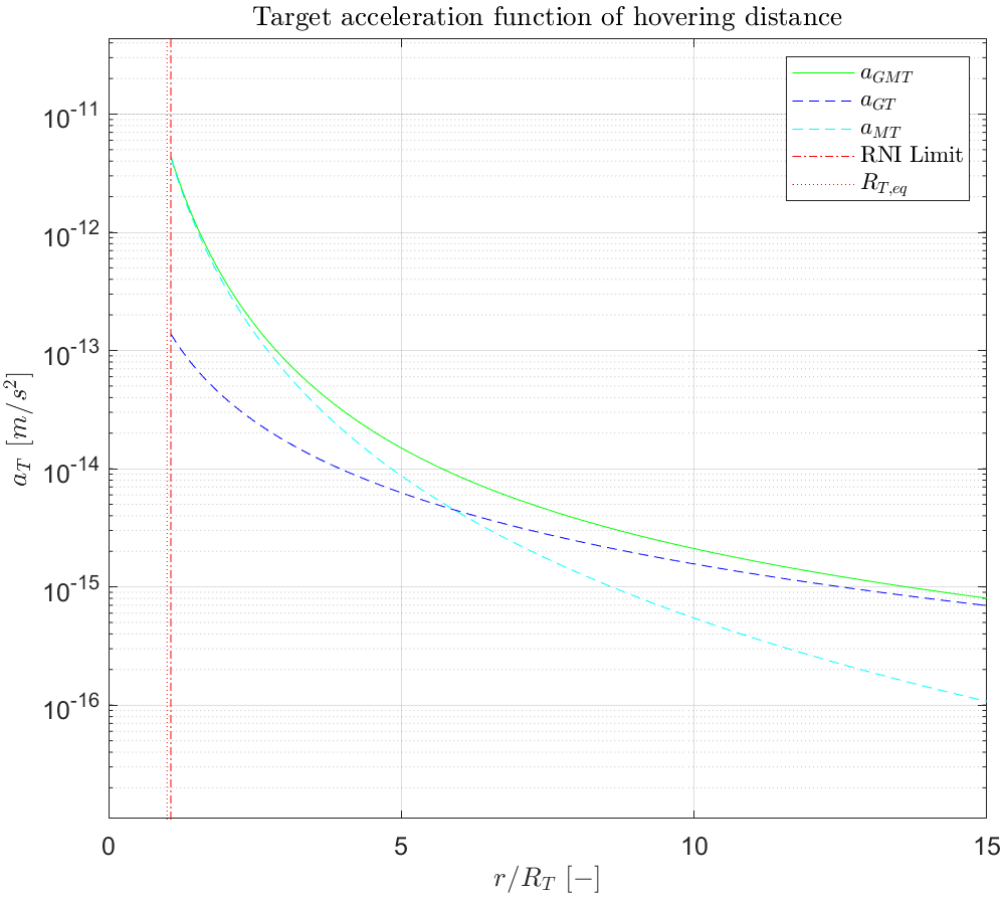

Figure 3.4: *Target's accelerations due to GT, MT and GMT obtained using the reference data of table 3.1. The target equivalent radius and the RNI limiting distance are shown as vertical lines on the Left Hand Side (LHS) of the graph.*

The BEP location is

$$d_{BEP} = \sqrt{\frac{K}{G}\frac{\mu_{\epsilon\mu_C}\mu_{\epsilon\mu_T}}{m_T m_C}} \tag{3.4}$$

and it is simply found looking for the hovering distance at which the GT and MT interactions are the same.

Recalling the RNI requirements and equation 2.25, the BEP happens at a feasible tugging distance if

$$d_{BEP} > d_{RNIL} \quad \rightarrow \quad \sqrt{\frac{K}{G}\frac{\mu_{\epsilon\mu_T}\mu_{\epsilon\mu_C}}{m_T m_C}} > \frac{R_T}{\sin\left(\frac{\pi}{2} - \phi_p\right)} \tag{3.5}$$

which is an irrational inequality that can be rearranged to extract a condition for the chaser's minimum SMM as

$$\frac{\mu_{\epsilon\mu_C}}{m_C} > \frac{m_T}{\mu_{\epsilon\mu_T}} \frac{G}{K} \frac{\left[\frac{3}{4\pi}\frac{m_T}{\rho_T}\right]^{2/3}}{\left[\sin\left(\frac{\pi}{2} - \phi_p\right)\right]^2} \triangleq \frac{\mu_{\epsilon\mu_C}}{m_C}|_{BEP@RNIL} \tag{3.6}$$

where the target equivalent radius is written in terms of the target's mass and density, assuming spherical shape.

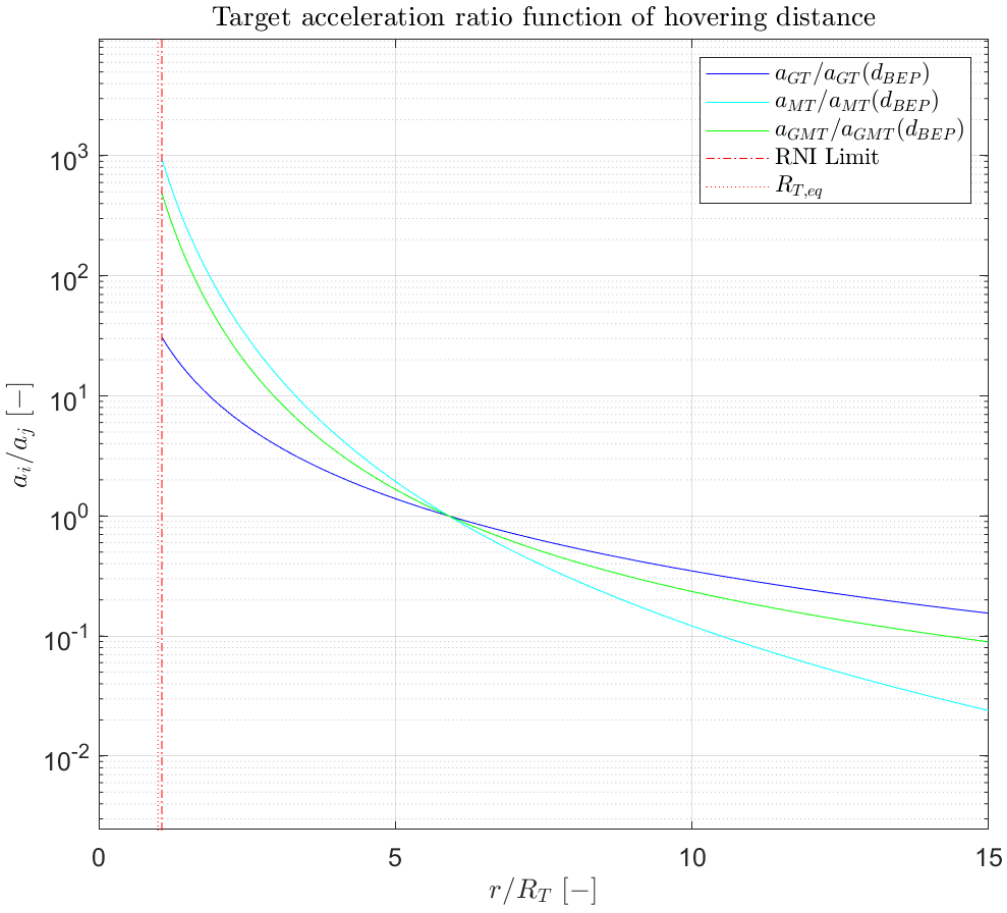

Figure 3.5: *Different target's accelerations ratios referred to the BEP condition, obtained using the reference data of table 3.1.*

Figure 3.5 presents the ratios of GT, MT and GMT accelerations over the corresponding values achieved at d_{BEP}. The break even point is visible and coincides with the unit ratios condition. The hovering distance at which MT has changed by an order of magnitude equal to n with respect to the value at d_{BEP} is

$$d_{MTL} = \left(10^{-\frac{n}{4}}\right) d_{BEP} \tag{3.7}$$

where $n > 0$ is associated to an increment of the order, whereas $n < 0$ to a decrement.

The minimum chaser's SMM that allows such point to be a feasible hovering distances is computed proceeding in the same way as inequality 3.5, obtaining

$$\frac{\mu_{\epsilon\mu_C}}{m_C} > \left(10^{\frac{n}{4}}\right) \frac{\mu_{\epsilon\mu_C}}{m_C}|_{BEP@RNIL} \tag{3.8}$$

The condition 3.6 defines a lower limit for the SMM that a chaser would need to generate in order to being able to magnetically accelerate the target at least as the gravitational field does, from a hovering distance farther than d_{RNIL}. The smaller the relative hovering distance is, the closer is the required chaser's dipole to the value of equation (3.6), in order to achieve the BEP condition. The RTS satisfaction becomes the limiting factor, setting the closest maintainable hovering point according to the chaser's thrusting capabilities. Moreover, the limiting conditions described in equations 3.6 and 3.8 strongly depend upon the target's physical properties and its tumbling state, through coefficient K.

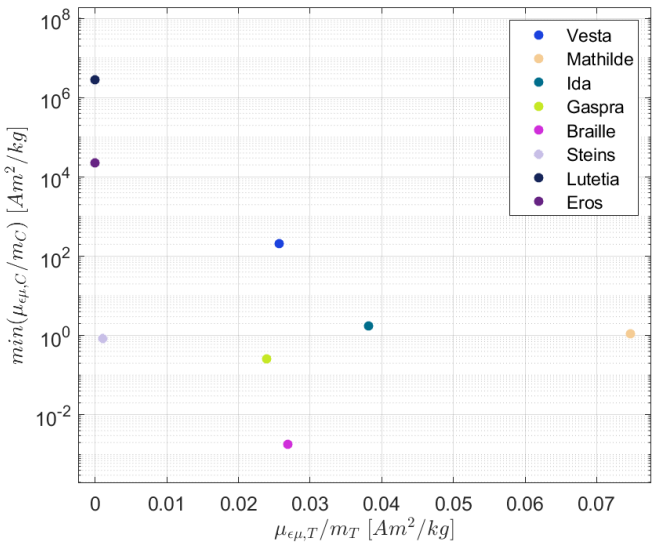

Figure 3.6: *Chaser's SMM for RNI satisfaction at $d_{BEP} = d_{RNIL}$, computed for all the identified targets summarized in 1.1.*

Figure 3.6 shows the minimum SMM the test chaser shall be able to generate for each target identified in table 1.1, the configuration showed in figure 3.3. The target with the smallest minimum SMM (i.e., Braille) is selected as one of test cases, used throughout the dissertation.

3.2.4 Gravitational-magnetic tug interaction as function of the objects' dipoles relative orientation

The analysis is based on equations 2.18 and aims to understand how the magnetic interaction between the considered objects, placed at a fixed hovering distance and characterised by constant dipole magnitudes, are affected by their dipoles relative orientation.

$$\begin{aligned} \mu_{\epsilon\mu_T} &= const \\ \mu_{\epsilon\mu_C} &= const \\ r &= const \end{aligned} \tag{3.9}$$

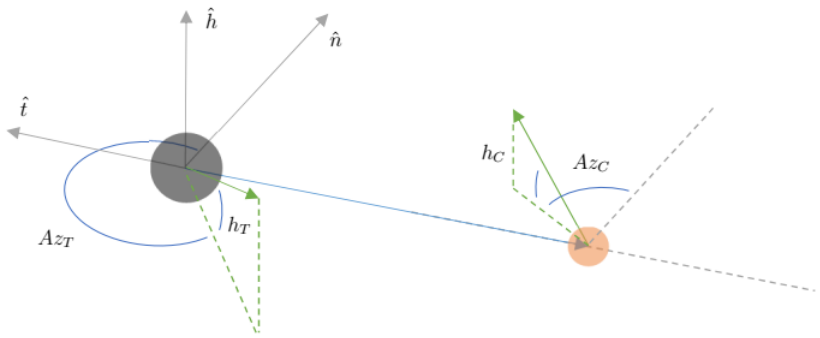

Figure 3.7: *Target centred NTH frame used in the relative attitude analysis and objects magnetic dipoles directions.*

Considering the NTH reference frame centred at the target's CM represented in figure 3.7, the unit vectors of the magnetic dipoles can be written in spherical coordinates as

$$\begin{aligned}\hat{\mu}_{\epsilon\mu,T} &= \hat{\mu}_{\epsilon\mu,T}(Az_T, h_T) = \begin{bmatrix}\cos(h_T)\cos(Az_T)\\ \cos(h_T)\sin(Az_T)\\ \sin(h_T)\end{bmatrix} \triangleq \begin{bmatrix}\bar{a}\\ \bar{b}\\ \bar{c}\end{bmatrix}\\ \hat{\mu}_{\epsilon\mu,C} &= \hat{\mu}_{\epsilon\mu,C}(Az_C, h_C) = \begin{bmatrix}\cos(h_C)\cos(Az_C)\\ \cos(h_C)\sin(Az_C)\\ \sin(h_C)\end{bmatrix} \triangleq \begin{bmatrix}\bar{e}\\ \bar{f}\\ \bar{g}\end{bmatrix}\end{aligned} \tag{3.10}$$

where Az_i $[rad]$ is the dipole's azimuth of object $i = T, C$ with respect of the motion normal unit vector (i.e., $\hat{n}$), h_i $[rad]$ is the dipole's altitude of object $i = T, C$ measured from the orbital plane of the target, and $\bar{a}, \bar{b}, \bar{c}$ and $\bar{e}, \bar{f}, \bar{g}$ are the Cartesian components of, respectively, the dipole of target and chaser in NTH frame.

Equation (2.19) is rewritten using (3.10) as

$$\begin{cases}\underline{F}_{T\to C,MT} &= \underline{F}_{T\to C,MT}(\hat{r}, Az_T, h_T, Az_C, h_C) =\\ &= \frac{3\mu_{\epsilon\mu 0}}{4\pi}\frac{\mu_{\epsilon\mu,T}\mu_{\epsilon\mu,C}}{r^4}\mathbf{\Phi}_T(\hat{r}, \hat{\mu}_{\epsilon\mu,T}(Az_T, h_T))\hat{\mu}_{\epsilon\mu,C}(Az_C, h_C)\\ \underline{F}_{C\to T,MT} &= -\underline{F}_{T\to C,MT}\end{cases} \tag{3.11}$$

which underlines the six Degrees Of Freedom (DOFS) of the resulting magnetic interaction: four angles that describe the dipoles orientations in the chosen frame (i.e., $\{Az_i, h_i\}, i = \{T, C\}$), and two angles that describe the hovering direction relative to the target (i.e., $\hat{r}$).

Recalling that the GMT is performing the non-inertial hovering along the target's velocity vector from behind (i.e., $\hat{r} \cdot \hat{v}_T = -1$), the DOFS are reduced to the dipoles' angles only and the hovering position is constrained on the target's orbital plane to be

$$\underline{r} = -r\hat{t}; \tag{3.12}$$

As previously stated, the GMT can contribute to the classical GT only if the newly introduced magnetic interaction has a not null component along the relative position vector which, in this special case, coincides with the target's velocity vector. Using the action reaction principle, this condition can be written for the magnetic force felt by the chaser as

$$\underline{F}_{T\to C,MT} \cdot \hat{r} < 0 \tag{3.13}$$

and it is achievable by acting upon the only controllable quantity of the system: the chaser's magnetic dipole direction.

The analysis considers all the possible orientations of the target's dipole and searches for the chaser's ones that generate a magnetic interaction force pointing towards the target, thus satisfying condition (3.13). This is referred from now on as target pointing DCL.

Target pointing DCL

The chaser's dipole orientation that leads to a magnetic interaction along a generic imposed direction is obtained from equation (2.19), dropping the magnitudes and inverting the relation as

$$\hat{\mu}_{\epsilon\mu,C} = \frac{\boldsymbol{\Phi}^{-1}(\hat{r}, \hat{\mu}_{\epsilon\mu,T}(Az_T, h_T))\, \hat{l}}{|\boldsymbol{\Phi}^{-1}(\hat{r}, \hat{\mu}_{\epsilon\mu,T}(Az_T, h_T))\, \hat{l}|} \quad , \quad \hat{\mu}_{\epsilon\mu,T} \cdot \hat{r} \neq 0 \tag{3.14}$$

where $\hat{l}$ is the unit vector of the imposed direction.

Being the hovering position defined by equation (3.12), the target pointing DCL is achieved if

$$\hat{l} = \hat{t} \equiv -\hat{r} \tag{3.15}$$

which can be used in equation (3.11), together with equation (3.14), to find the resulting magnetic interaction acting on the chaser

$$\begin{cases} \underline{F}_{T\to C,MT} = \underline{F}_{T\to C,MT}(Az_T, h_T) = -\frac{3\mu_{\epsilon\mu 0}}{4\pi} \frac{\mu_{\epsilon\mu,T}\mu_{\epsilon\mu,C}}{r^4} \frac{1}{|\boldsymbol{\Phi}^{-1}(\hat{r}, Az_T, h_T)\, \hat{r}|} \hat{r} \\ |\boldsymbol{\Phi}^{-1}(\hat{r}, Az_T, h_T)\, \hat{r}| = \frac{\sqrt{(\cos(\mathrm{Az}_T)\cos(h_T))^2 + (\sin(h_T))^2 + (\sin(\mathrm{Az}_T)\cos(h_T))^2}}{\left(-\cos(\mathrm{Az}_T)^2\cos(h_T)^2 + \cos(h_T)^2 + 1\right)} \end{cases} \tag{3.16}$$

where the original DOFS are reduced to the two angles associated to the target's dipole orientation with respect of the NTH frame.

Note that equation (3.16) is always defined, being $\hat{r}$ contained within the achievable plane associated to the singularity condition for $\boldsymbol{\Phi}$ discussed in section 2.3. On the other hand, equation (3.14) is valid only for a subset of the possible target orientations in respect to $\hat{r}$. In case of $\hat{\mu}_{\epsilon\mu,T} \cdot \hat{r} = 0$, it is still possible to obtain a pure radial component by imposing the target's dipole to be contained into the plane defined by

$\hat{r}$ itself (i.e., $\hat{\mu}_{\epsilon\mu,C} \cdot \hat{r} = 0$).

The latter condition is found through inspection of equation (2.18) and it is used to construct the complete target pointing DCL as

$$\begin{cases} \hat{\mu}_{\epsilon\mu,C} = -\frac{\boldsymbol{\Phi}^{-1}(\hat{r},\hat{\mu}_{\epsilon\mu,T}(Az_T,h_T))\,\hat{r}}{|\boldsymbol{\Phi}^{-1}(\hat{r},\hat{\mu}_{\epsilon\mu,T}(Az_T,h_T))\,\hat{r}|} & \hat{\mu}_{\epsilon\mu,T} \cdot \hat{r} \neq 0 \\ \hat{\mu}_{\epsilon\mu,C} = -\hat{\mu}_{\epsilon\mu,T} & \hat{\mu}_{\epsilon\mu,T} \cdot \hat{r} = 0 \end{cases} \tag{3.17}$$

Equation (3.16) shows that it is always possible to impose a magnetic force on the target with a pure radial component aligned with the local gravitational contribution. This force is modulated by the target's dipole evolution in the NTH frame (i.e., $Az_t(t)$ and $h_T(t)$) caused by the combined effects of an initial tumbling state of the target and its orbital motion about the primary.

The same equation can be rewritten proceeding as in equation (3.3) as

$$\begin{cases} \underline{F}_{T\to C,MT} = -K_r(Az_T, h_T)\frac{\mu_{\epsilon\mu,T}\mu_{\epsilon\mu,C}}{r^4}\hat{r} \\ K_r(Az_T, h_T) \triangleq \frac{3\mu_{\epsilon\mu 0}}{4\pi|\boldsymbol{\Phi}^{-1}(\hat{r},Az_T,h_T)\,\hat{r}|} \end{cases} \tag{3.18}$$

where K_r [−] is the radial relative orientation coefficient.

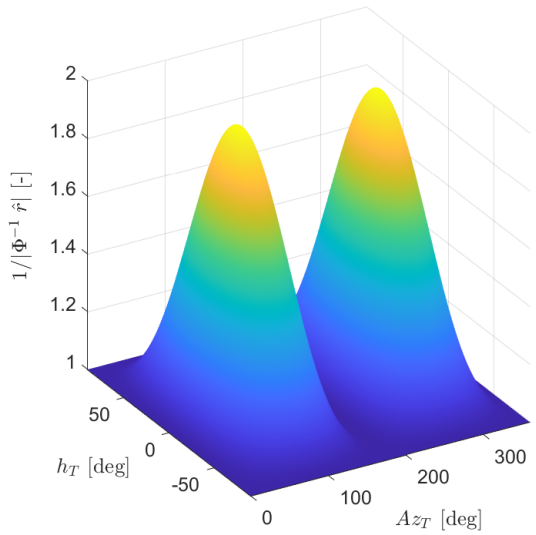

Figure 3.8: *Normalised radial relative orientation coefficient using the target pointing DCL function of the azimuth and elevation of the target's dipole in the NTH frame.*

A quick analysis of the K_r, presented in figure 3.8, shows that it is limited to

$$K_r(Az_T, h_T) \in \left[\frac{3\mu_{\epsilon\mu 0}}{4\pi}, \frac{6\mu_{\epsilon\mu 0}}{4\pi}\right] \tag{3.19}$$

The closer the chaser's dipole unit vector is to the hovering position unit vector (i.e., $\hat{r}$), the stronger is the obtained mutual magnetic interaction force between the objects. The strongest magnetic interaction is achieved when $|\hat{\mu}_{\epsilon\mu,T} \cdot \hat{r}| = 1$, the weakest when $\hat{\mu}_{\epsilon\mu,T} \cdot \hat{r} = 0$.

Figure 3.9 shows the magnetic interaction force and torque for the test case described in table 3.1, when the target pointing DCL is applied at a distance of $r = d_{BEP}/2$ $[m]$. Given the target's KEP and a generic tumbling state, its dipole draws a curve in the $\{Az_T, h_T\}$ plane that evolves according to the linear and rotational momentum variation of the target itself. It is assumed that any relative orientation are reachable with equal probability, this choice is enforced by the uncertainty affecting the target tumbling state which is often present and challenging to be reduced until medium-close range operations at the target begin.

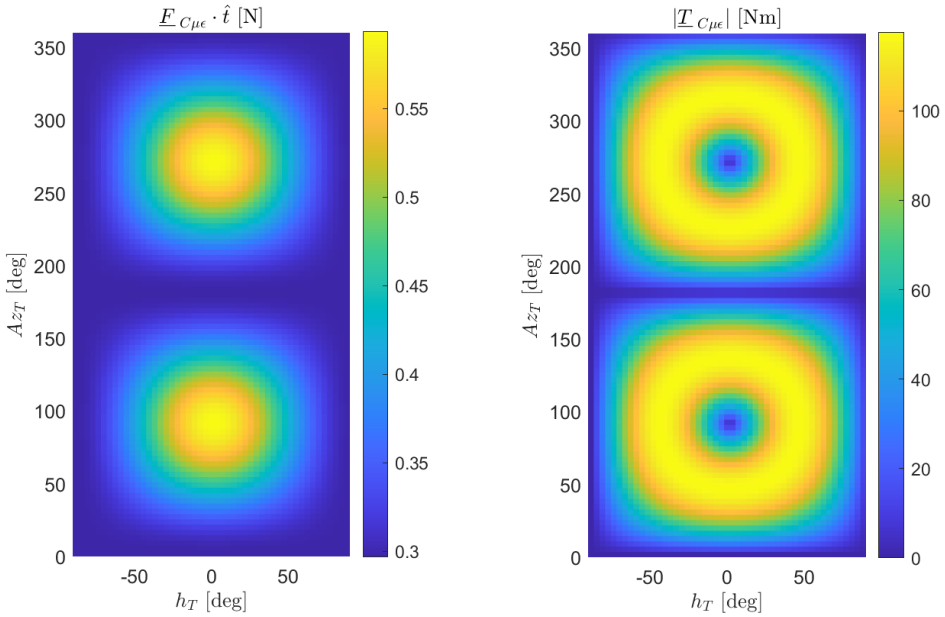

Figure 3.9: *Magnetic force along the relative position vector and magnitude of the resulting magnetic torque that act on the chaser, using the target pointing DCL.*

As a consequence, the chaser could be exposed to magnetic interaction torques that can reach high values and last for the entire duration of the deflection (i.e., months if not years). This may lead to the saturation of the devices used to manage the angular

momentum of the chaser (e.g., inertial wheels, controlled moment gyro), affecting its controllability and thus increasing the risk of the entire mission. Considering the test case, values up to 100 Nm can be reached in the worst relative orientation possible.

Two solutions are identified to overcome the possible issues introduced by the target pointing DCL:

- The dipole of the chaser is used for deflection purposes for a limited amount of time and then exploited to desaturate the AOCS allowing for internal momentum management. Nevertheless, the tugging duty cycle (i.e., the ratio between the time spent on deflection over the one spent on a complete desaturation) shall be maintained high enough to allow an appreciable contribution to the overall induce LTA.

- The DCL is changed in such a way that the magnetic interaction torque is absent. This is achieved imposing the target's dipole to be aligned with the local magnetic field generated by the target itself and it is referred from now on as B-field DCL. Since equation 3.17 is not used, the resulting magnetic interaction force is not necessarily aligned with the relative position vector and thus, it may not cooperate with the gravitational interaction in the most efficient way.

Although the first solution may be viable, it is not further investigated in the dissertation. The second solution is considered instead, assumed to be a reasonable trade-off between efficiency of the induced LTA and controllability of the system.

B-field DCL

The target's magnetic field direction at the chaser location is computed using equation (2.19) as

$$\hat{B}_T = \frac{\boldsymbol{\beta}(\hat{r})\, \hat{\mu}_{\epsilon\mu,T}(Az_T, h_T)}{|\boldsymbol{\beta}(\hat{r})\, \hat{\mu}_{\epsilon\mu,T}(Az_T, h_T)|} \tag{3.20}$$

Assuming to align the chaser's dipole to the field

$$\hat{\mu}_{\epsilon\mu,C} = \mu_{\epsilon\mu,C}\hat{B}_T \tag{3.21}$$

the magnetic interaction torque acting on the chaser vanishes, whereas the resulting magnetic force is found using equations (3.12) and (3.21) in (2.19), obtaining

$$\begin{cases} \underline{F}_{T\to C,MT}(Az_T, h_T) = \frac{3\mu_{\epsilon\mu 0}}{4\pi}\frac{\mu_{\epsilon\mu,T}\mu_{\epsilon\mu,C}}{r^4}\frac{\boldsymbol{\Phi}_T(\hat{r},Az_T,h_T)\,\boldsymbol{\beta}_T(\hat{r})\hat{\mu}_{\epsilon\mu,T}(Az_T,h_T)}{|\boldsymbol{\beta}_T(\hat{r})\,\hat{\mu}_{\epsilon\mu,T}(Az_T,h_T)|} \\ \frac{\boldsymbol{\Phi}_T(\hat{r},Az_T,h_T)\,\boldsymbol{\beta}_T(\hat{r})\hat{\mu}_{\epsilon\mu,T}(Az_T,h_T)}{|\boldsymbol{\beta}_T(\hat{r})\,\hat{\mu}_{\epsilon\mu,T}(Az_T,h_T)|} = \frac{1}{\sqrt{|a|^2+4\,|b|^2+|c|^2}}\begin{bmatrix} -\bar{a}\,\bar{b} \\ \bar{a}^2+4\,\bar{b}^2+\bar{c}^2 \\ -\bar{b}\,\bar{c} \end{bmatrix} \end{cases} \tag{3.22}$$

where the target's dipole components in the NTH frame, defined in equation (3.10), are used for compactness.

Equations (3.22) can also be rewritten dividing the contribution of the radial component from the orthogonal one, obtaining

$$\begin{cases} \underline{F}_{T\to C,MT} & = -K_r(Az_T, h_T)\frac{\mu_{\epsilon\mu,T}\mu_{\epsilon\mu,C}}{r^4}\hat{r} + K_\sigma(Az_T, h_T)\frac{\mu_{\epsilon\mu,T}\mu_{\epsilon\mu,C}}{r^4}\hat{\sigma} \\ K_r(Az_T, h_T) & \triangleq \frac{3\mu_{\epsilon\mu 0}}{4\pi}\frac{\cos(\mathrm{Az}_T)^2\cos(h_T)^2+4\sin(\mathrm{Az}_T)^2\cos(h_T)^2+\sin(h_T)^2}{\sqrt{(\cos(\mathrm{Az}_T)\cos(h_T))^2+(\sin(h_T))^2+4\,(\sin(\mathrm{Az}_T)\cos(h_T))^2}} \\ K_\sigma(Az_T, h_T) & \triangleq \frac{3\mu_{\epsilon\mu 0}}{4\pi}\frac{\sqrt{(\sin(\mathrm{Az}_T)\cos(h_T)\sin(h_T))^2+\frac{(\cos(h_T))^4\,(\sin(2\,\mathrm{Az}_T))^2}{4}}}{\sqrt{(\cos(\mathrm{Az}_T)\cos(h_T))^2+(\sin(h_T))^2+4\,|\sin(\mathrm{Az}_T)\cos(h_T)|^2}} \end{cases} \tag{3.23}$$

where $\hat{\sigma}$ is the generic direction orthogonal to the relative position vector, and K_σ $[-]$ is the relative orientation coefficient associated to the orthogonal contributions.

Figure 3.10 shows the normalised K_r and K_σ coefficients for every possible orientation of the target's dipole. As in the target pointing DCL, the B-field DCL creates a radial contribution with maxima at $\{Az_T, h_T\} = \{\pm 90°, 0°\}$ bounded within the same interval of the former, defined by equation (3.19).

The out of radial contribution results to be limited to the interval

$$K_\sigma(Az_T, h_T) \in \left[0, \frac{3\mu_{\epsilon\mu_0}}{8\pi}\right] \tag{3.24}$$

The analysis of K_r obtained with the proposed DCL shows that moving away from the maxima location, the coefficient decay is slowed down in the B-field aligned DCL compared to the target pointing DCL. This is evident from the percentage increment in K_r shown in figure 3.11, where increments up to 6% are identified.

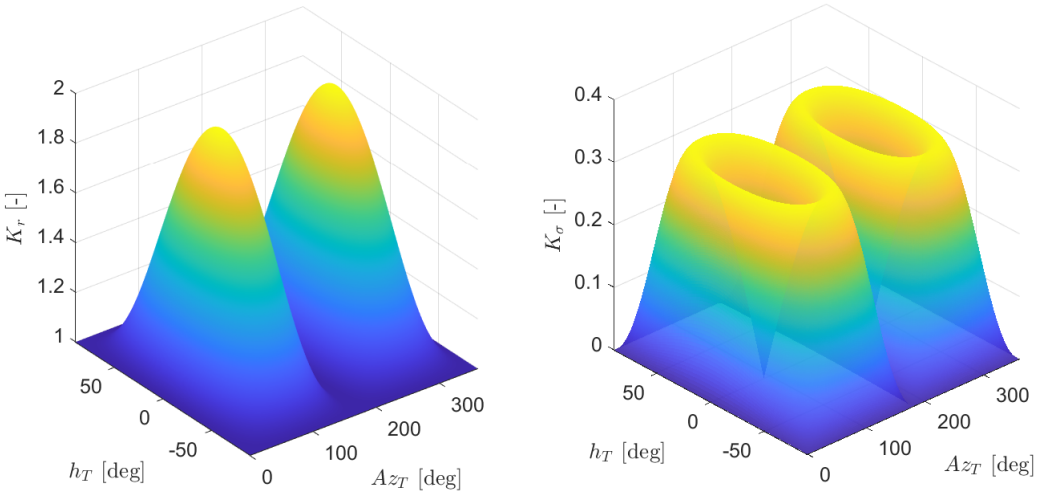

Figure 3.10: *Normalised radial and out of radial relative orientation coefficients function of the target's dipole azimuth and elevation in the NTH frame computed for the B-field aligned DCL*

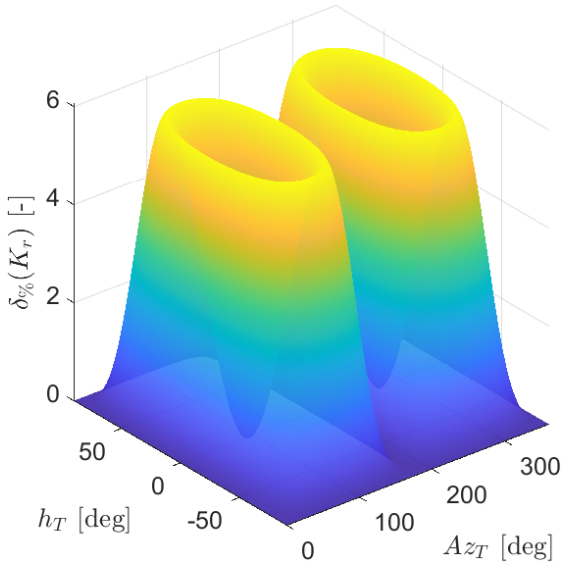

Figure 3.11: *K_r coefficient percentage increment in respect the target pointing DCL, function of the target's dipole azimuth and elevation in the NTH frame.*

Therefore, a GMT adopting the B-field aligned DCL reduces the chaser's angular momentum management workload, being the magnetic torque induced on the chaser absent. On the other hand, this advantage is translated into a non radially aligned magnetic force contribution that shall be compensated by the AOCS of the system, to allow the non-inertial hovering to happen at a fixed location.

3.3 Gravitational-magnetic tug model

This section presents the GMT model developed in the dissertation. Section 3.3.1 discusses the chaser's mass allocation and proposes a criterion for the GMT comparison with a classical GT. Section 3.3.2 presents three GMT tugging modes, and derives the relative hovering distance that satisfy both RNI and RTS. Section 3.3.3 discusses the procedure used to retrieve the estimated deflection at MOID epoch which is then used, in section 3.3.4, to compare the proposed GMT tugging modes. Section 3.3.5 presents the sensitivity analysis with respect to a selected group of parameters.

The GMT model is based on the GT model presented in section 2.5 which is here extended to consider the presence of a magnetic interaction. Even though all the hovering positions farther than d_{RNIL} are possible, the ones that also satisfy the RTS are a limited subset and depend on the actual capability of the chaser's PS to generate enough thrust in order to maintain the tugging for a given amount of time t_{tug}. The chaser shall also be able to generate and maintain a certain magnetic dipole using the onboard SMS.

The analysis is performed for special configuration in which the tumbling state of the target is not affecting the actual performance, and the resulting magnetic interaction has a pure radial component. Referring to section 3.2.4, this coincides with a constant K_r and null K_σ, and it is associated to a target with magnetic dipole and angular velocity vector orthogonal to the orbital plane. The tumbling state influence on the performance is analysed in section 3.4.

From an operational point of view, the assumptions could be met performing an initial target de-tumbling phase, followed by a re-orientation one, prior to the GMT. The actual feasibilities of such phases are not covered in the dissertation and are left for future work.

3.3.1 Chaser's mass repartition

The chaser's net mass is here distributed according to the specific task it is designed for. Figure 3.12 shows the considered repartition scheme, identifying the mass associated to the onboard available fuel (i.e., m_{fuel}), the dry mass (i.e., m_{dry}), and the power mass (i.e., m_{pw}) repartition between SMS and PS.

Recalling the GT static analysis, the chaser's net mass can be written as

$$\begin{cases} m_C(t) & = m_{dry} + m_{fuel}(t) = \\ & = m_s + m_{pw} + m_{fuel}(t) = \\ & = (1 - POD)m_{dry} + PODm_{dry} + m_{fuel}(t) \end{cases} \tag{3.25}$$

where the dry mass is expanded to identify the fraction associated to the PGS (i.e., m_{pw}) using the POD ratio.

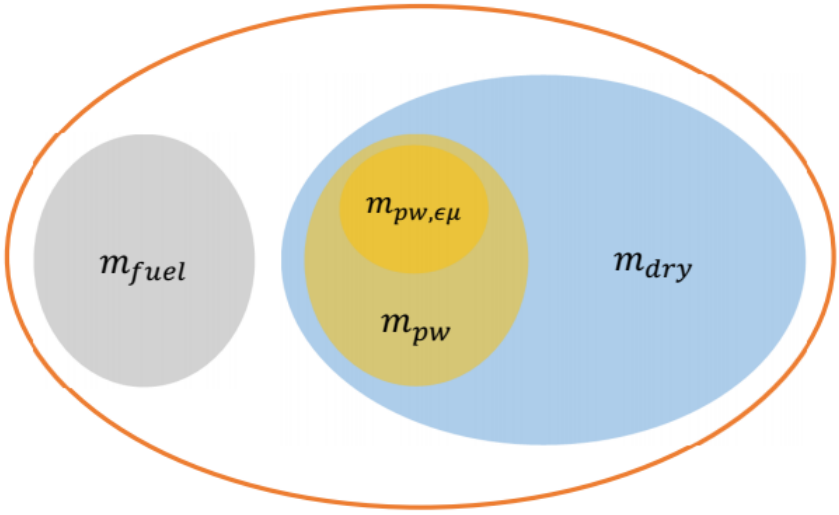

Figure 3.12: *Chaser mass repartition scheme at interception epoch.*

For the GMT case, the PGS mass is further partitioned into the power masses associated to the thrust generation $m_{pw,th}$ $[kg]$, and into the one associate to the magnetic dipole generation $m_{pw,\epsilon\mu}$ $[kg]$.

The net mass is rewritten as

$$\begin{cases} m_C(t) & = (1 - POD)m_{dry} + POD_{th}m_{dry} + POD_{pw}m_{dry} + m_{fuel}(t) \\ \alpha_{POD} & \triangleq \frac{m_{pw,th}}{m_{pw}} \\ POD_{pw,th} & \triangleq \alpha_{POD}POD \\ POD_{pw,\epsilon\mu} & \triangleq (1 - \alpha_{POD})POD \end{cases} \tag{3.26}$$

where α_{POD} [−] is introduced to describe such refined partition and it is defined as the ratio of PGS's mass used for PS over PGS's mass used for SMS.

It is important to understand that for a GT, the entire mass dedicated to the power generation can be used for propulsive purposes, whereas, for a GMT, it shall be partitioned as in equation (3.26) to consider the presence of the new subsystem which is necessary to operate. Recalling that the available thrust is assumed to be proportional to the power mass (i.e., equation 2.12), the thrusting capability for a chaser performing a GT is always higher than the one associated to the same chaser performing a GMT.

To effectively compare the two approaches, the net mass at interception m_{C0}, the power over dry mass ratio *POD*, the PS performance τ_{pw}, and the PGS performance ξ_{th} are kept constant. This means that the overall gravitational contribution to the GMT is not improved by the presence of any additional mass associated to SMS nor by any improvement of the chaser ability to sustain a closer hovering point (i.e., higher tugging force).

3.3.2 Tugging modes

Three different approaches are presented and compared. They all aim to define the chaser's magnetic dipole to achieve a certain amplification of the tugging force, compared to a pure GT. Table 3.2 presents an overview of the proposed Tugging Modes (TMs).

Tugging Mode	**TM1**	**TM2**	**TM3**
Magnetic fuel mass compensation	✓		
Magnetic amplification	✓	✓	✓
Constant dipole magnitude			✓

Table 3.2: *GMT tugging modes*

(**TM1**) The magnetic interaction is such that the mass loss due to fuel mass consumption is completely compensated during the entire duration of the tug. This leads to an interaction force of

$$F_{GMT}(t) = (1 + \nu)\, F_{GT}(t_i) = const \tag{3.27}$$

where the ν [−] allows to set the ratio between the GMT and GT forces at interception.

(**TM2**) The ratio between magnetic and gravitational interactions is constant and equal to ν, for the entire duration of the tug. This leads to a magnetic interaction force of

$$F_{MT}(t) = \nu\, F_{GT}(t) \tag{3.28}$$

(**TM3**) The ratio between magnetic and gravitational interactions is set to be equal to ν at the interception epoch. This leads to a magnetic interaction force of

$$F_{MT}(t) = \nu\, F_{GT}(t_i) = const \tag{3.29}$$

The coefficient ν is referred, from now on, as magnetic amplification factor $\nu \in \mathbb{R}^+$.

Tugging mode 1

In this mode the magnetic interaction magnitude is changing in time to allow the compensation to happen. This leads to a variable chaser's magnetic dipole strength of

$$\begin{aligned} \mu_{\epsilon\mu_C}(t,d) &= \frac{1}{K}\frac{\nu F_{GT}(t_i,d) + \Delta F_{GT}(t,d)}{\mu_{\epsilon\mu,T}} d^4 = \\ &= \frac{G}{K}\,\frac{m_T\big(\nu m_{C0} + (m_{C0} - m_C(t,d))\big)}{\mu_{\epsilon\mu,T}} d^2 \end{aligned} \tag{3.30}$$

The chaser's mass variation in time is computed integrating (2.14) from interception to a generic tugging time and, being the tugging force constant, it results in

$$m_C(t,d) = m_{C0} - (1+\nu) G \frac{m_T m_{C0}}{d^2\, Isp\, g_0\, \eta_{th}(d)} (t - t_i) \tag{3.31}$$

Equation (3.31) shows that the highest magnetic dipole magnitude is proportional to the fuel mass stored onboard the chaser.

The equilibrium hovering distance that satisfies both RTS and RNI requirements is found solving equation (2.27) in which the Right Hand Side (RHS) is written with the amplified tugging contribution and the relation (3.31) is used to compute the dry mass of the chaser. The resulting implicit equation is

$$(1+\nu)\,G\,\frac{m_T\,m_{C0}}{(d_{GMT})^2} - POD_{pw}\frac{m_C(t_{co},d_{GMT})}{2}\frac{\xi_{th}}{\tau_{pw}}\eta_{th}\,(d_{GMT}) = 0 \tag{3.32}$$

where d_{GMT} is the sustainable hovering distance.

Equation (3.32) is solved using the numerical method based on ”fsolve” algorithm which is part of the numerical optimization toolbox of Matlab®. Figure 3.13 shows the LHS of equation (3.32) for the reference data in table 3.1, parametrized over the total tugging time, as a function of the hovering distance between d_{RNIL} (i.e., lower boundary for hovering position admissibility) and $5d_{RNIL}$.

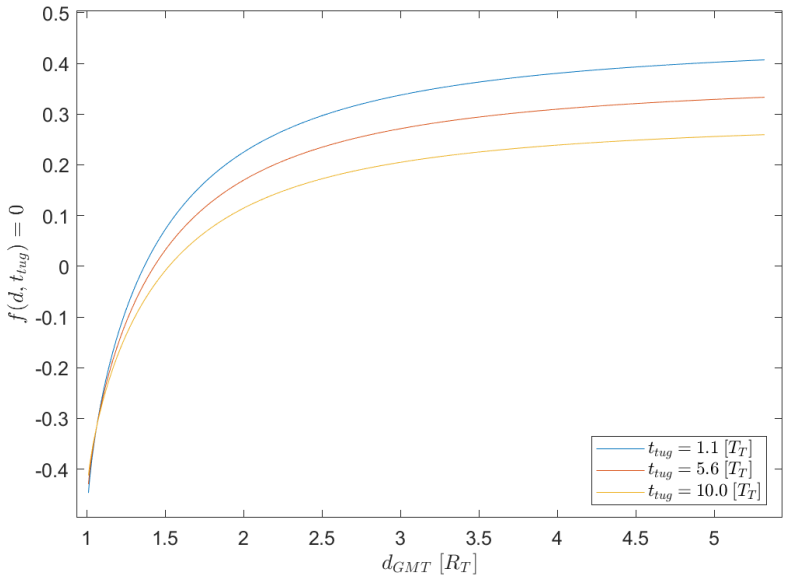

Figure 3.13: *TMI implicit function computed with the reference data for a unitary amplification factor, parametrized over the total tugging time.*

For a total given tugging time, it is now possible to use d_{GMT} to compute: the force acting on the target using equation 3.27, the required magnetic dipole that allows such LTA using equations (3.30) and the mass internal repartition using equations (3.25) and (3.26).

The resulting acceleration acting on the target is

$$\underline{a}_{GMT} = -\frac{F_{GMT}(t_i,d_{GMT})}{m_T}\hat{r} \tag{3.33}$$

which is associated to a total transferred impulse of

$$\underline{I}_{TOT} = \int_{t_i}^{t_{co}} m_T \, \underline{a}_{GMT} dt \tag{3.34}$$

that can be particularised for TM1 as

$$\begin{cases} I_{TOT,r} & = F_{GMT}(t_i, d_{GMT})(t_{co} - t_i) = \\ & = (1+\nu) G \frac{m_T m_{C0}}{d_{GMT}^2} t_{tug} \qquad [s] \end{cases} \tag{3.35}$$

Tugging mode 2

In this mode the magnetic interaction magnitude is changing in time such that it is always ν times the gravitational contribution. The resulting chaser's magnetic dipole strength is changing in time and is equal to

$$\begin{aligned} \mu_{\epsilon\mu_C}(t,d) &= \frac{\nu}{K} \frac{F_{GT}(t,d)}{\mu_{\epsilon\mu,T}} d^4 = \\ &= \nu \frac{G}{K} \frac{m_T m_C(t,d)}{\mu_{\epsilon\mu,T}} d^2 \end{aligned} \tag{3.36}$$

which is leading to a tugging force equal to

$$F_{GMT}(t,d) = (1+\nu) F_{GT}(t,d) \tag{3.37}$$

Equation (3.36) shows that the highest magnetic dipole magnitude is achieved at interception epoch.

The chaser's mass time variation is obtained integrating equation (2.14) with (3.37), obtaining

$$\begin{cases} m_C(t,d) = m_{C0} \exp^{-(1+\nu)A(d)(t-t_i)} \\ A(d) \triangleq \frac{G m_T}{d^2 \, Isp \, g_0 \, \eta_{th}(d)} \end{cases} \tag{3.38}$$

Note that the resulting chaser's mass has the same structure of equation 2.26, being the GT tugging force constantly amplified by the amplification factor.

The equilibrium hovering distance is found solving equation (2.27), rewriting its LHS using (3.37) and computing the chaser's dry mass with equation (3.38). The resulting implicit equation is

$$(1+\nu)\, G\, \frac{m_T\, m_{C0}}{(d_{GMT})^2} = POD_{pw} \frac{m_C(t_{co}, d_{GMT})}{2} \frac{\xi_{th}}{\tau_{pw}} \eta_{th}\,(d_{GMT}) \tag{3.39}$$

Equation 3.39 is solved proceeding in the same way as TM1 and the same derived quantities are computed.

Tugging mode 3

In this mode the magnetic interaction magnitude is constant in time and it is fixed at interception epoch to satisfy condition (3.29). The magnetic dipole that the chaser has to generate is

$$\begin{aligned} \mu_{\epsilon\mu_C}(t,d) &= \frac{\nu}{K} \frac{F_{GT}(t_i,d)}{\mu_{\epsilon\mu,T}} d^4 = \\ &= \nu\, \frac{G}{K} \frac{m_T m_{C0}}{\mu_{\epsilon\mu,T}} d^2 \end{aligned} \tag{3.40}$$

which is leading to a tugging force equal to

$$F_{GMT}(t,d) = (\nu) F_{GT}(t_i,d) + F_{GT}(t,d) \tag{3.41}$$

The resulting LTA results to be the sum of a constant magnetic contribution and a decreasing gravitational one. To find the chaser's mass evolution in time, the IVP (2.14) shall be written as

$$\begin{cases} \dot{m}_C + A(d) m_C = B(d) \\ A(d) = \frac{G m_T}{d^2\, Isp\, g_0\, \eta_{th}(d)} \\ B(d) \triangleq -(\nu) \frac{G m_T m_{C0}}{d^2\, Isp\, g0\, \eta_{th}(d)} \end{cases} \tag{3.42}$$

Equation 3.42 is then integrated, leading to

$$\begin{aligned} m_C = m_C(t) &= m_{C0} \exp^{-A(d)(t-t_i)} - \frac{B(d)}{A(d)} \left[\exp^{-A(d)(t-t_i)} - 1\right] = \\ &= m_{C0} \left[(1+\nu) \exp^{-A(d)(t-t_i)} - \nu)\right] \end{aligned} \tag{3.43}$$

The equilibrium hovering distance is found solving equation (2.27), rewriting its LHS with (3.41) and using (3.43) to express the chaser's dry mass. The resulting implicit equation is

$$(1+\nu)\,G\,\frac{m_T\,m_{C0}}{(d_{GMT})^2} = POD_{pw}\frac{m_C(t_{co},d_{GMT})}{2}\frac{\xi_{th}}{\tau_{pw}}\eta_{th}\,(d_{GMT}) \tag{3.44}$$

Equation (3.44) is solved proceeding in the same way as TM1 and the same derived quantities are computed.

3.3.3 Estimated deflection at minimum orbit intersection distance

The estimation of the deviation is done creating a virtual MOID event in which the target and the IO are at their MOID true anomalies at the MOID epoch. For this preliminary analysis, the KEP at MOID of these objects is computed using geometric considerations; the procedure is described in appendix B.

Given the target KEP at MOID, the target state that allows it to be tugged from interception epoch until the MOID epoch itself is

$$\begin{cases} KEP_T(t_i) = [a, e, i, \Omega, \omega, \theta(t_i)]_T \\ M_T(t_i) = M_T(t_{moid}) - \frac{2\pi}{T_T}t_{tug} \end{cases} \tag{3.45}$$

where the M_T is the mean anomaly of the nominal target and the map between true and mean anomalies is given by relation (2.10).

The target's state variation due to a pure tangential LTA is then computed integrating Gauss' equations with the acceleration induced by either GT (i.e., equation (2.29)) or by GMT (i.e., equations (3.27),(3.37),(3.41)). The integration is performed using ODE113 provided by Matlab®using the tolerances absolute tolerance of $1e-16$. The deviation from nominal target position at MOID is computed using equations (2.21), for all the proposed TM.

3.3.4 Tugging modes comparison

In order to compare the presented GMT tugging modes with the traditional GT, two test targets are considered. Braille, one of the possible identified candidates with a global magnetisation state that has the highest SMM and the lowest minimum chaser's SMM required for RNI, and a virtual asteroid with same physical properties of Apophis [56] for which an SMM equal to Braille is used.

A summary of the physical properties of the selected targets is presented in table 3.3, while the orbital elements and related derived quantities are summarized in table 3.4. The analysis covers a tugging period from one week up to $15T_T$ with a discretization step of 1 week. The upper limit is selected considering that the higher it is, the greater is the required propellant mass that allows the chaser to sustain the tug. The adopted value is for comparison purposes only and does not represent any particular condition.

Test target I: $Apophis$			Test target II: $Braille$		
R_{T1}	185	m	R_{T2}	800	m
ρ_{T1}	2300	kg/m^3	ρ_{T2}	3900	kg/m^3
m_{T1}	$6.1 \cdot 10^{10}$	kg	m_{T2}	$8.3642 \cdot 10^{12}$	kg
$\mu_{\epsilon\mu,T1}/m_{T1}$	0.0251	Am^2/kg	$\mu_{\epsilon\mu,T2}/m_{T2}$	0.0251	Am^2/kg
$\mu_{\epsilon\mu,T1}$	$1.5311 \cdot 10^9$	Am^2	$\mu_{\epsilon\mu,T2}$	$2.0994 \cdot 10^{11}$	Am^2

Table 3.3: *Selected test targets.*

Target	a $[AU]$	e $[-]$	i $[deg]$	Ω $[deg]$	ω $[deg]$	θ_{MOID} $[deg]$	T $[y]$
$Apophis$	0.9223	0.1911	3.33	204.46	126.36	101.16	0.8857
$Braille$	2.3416	0.4332	28.99	241.95	356.19	138.65	3.5832

Table 3.4: *Keplerian elements of the selected test targets and derived quantities*

All the GMT modes are compared with the GT under the assumptions of fixed interception mass, fixed chaser PS geometry and performance, fixed PGS performance and fixed *POD* ratio. Table 3.5 reports a summary of the selected test chaser.

m_{C0}	1500	kg	Isp	3100	s	α_{POD}	0.5
ξ_{th}	$3.4 \cdot 10^{-5}$	N/W	τ_{pw}	0.025	kg/W	ν	1
β_p	20	deg	POD	0.5			

Table 3.5: *Selected test chaser physical properties and efficiencies.*

Sustainable hovering distance

The hovering distance that satisfies RNI and RTS is found solving equations 3.32, 3.39, 3.44 for the GMT and equation (2.28) for the GT.

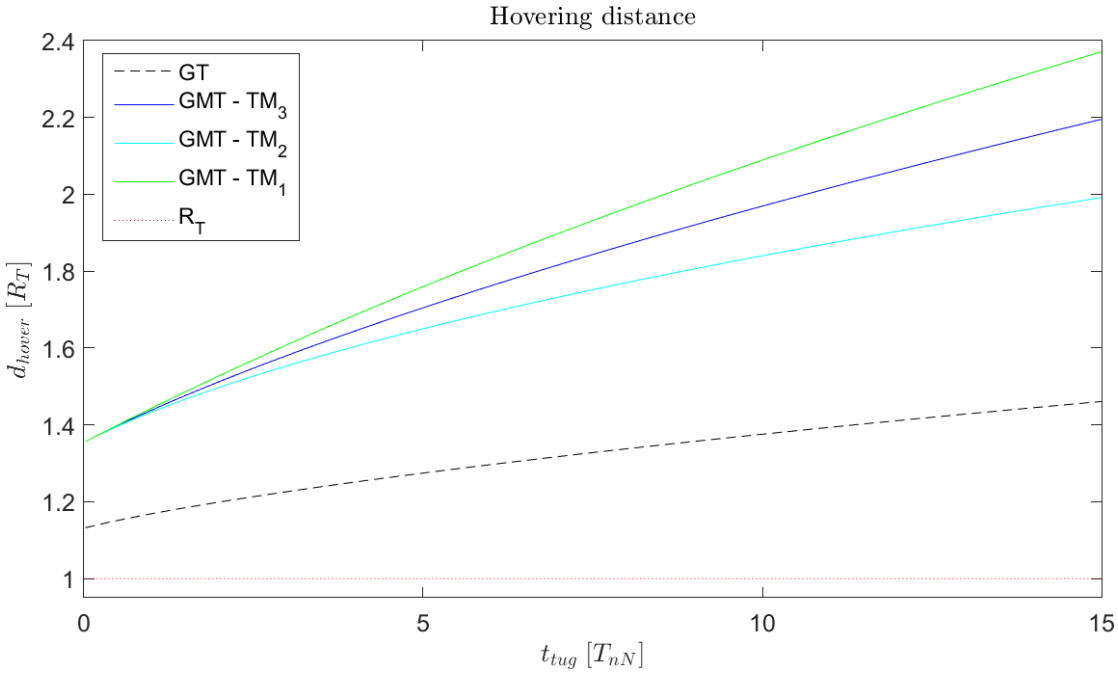

Figure 3.14: *Hovering distances as a function of the total tugging time for target I (i.e., $R_T = 185m$).*

Figure 3.14 shows the sustainable distances for each approach applied to test target I. As expected from the analysis of the chaser's mass evolution in time (e.g., equation (3.31)), the higher the total tugging time is, the lower is the resulting dry mass that allows to store the proper amount of fuel for the tug to take place. As a consequence, the chaser's thrusting capability is decreasing as the tugging time increases and thus, the need of a farther hovering distance.

Any of the proposed GMT TMs allow the LTA to be applied at a farther distance with respect of the one associated to a traditional GT. The farther the distance is, the lower is the cant angle β_p of the adapted nozzle configuration, and the lower is the cosine losses introduced by equation (2.24). This results into a more efficient usage of the PS.

Figure 3.15 shows the obtained relative percentage increment in hovering distance for test target I, referred to the GT. TM1 leads to the highest relative increment of the hovering distance, for a constant total tugging time, whereas TM2 to the smallest.

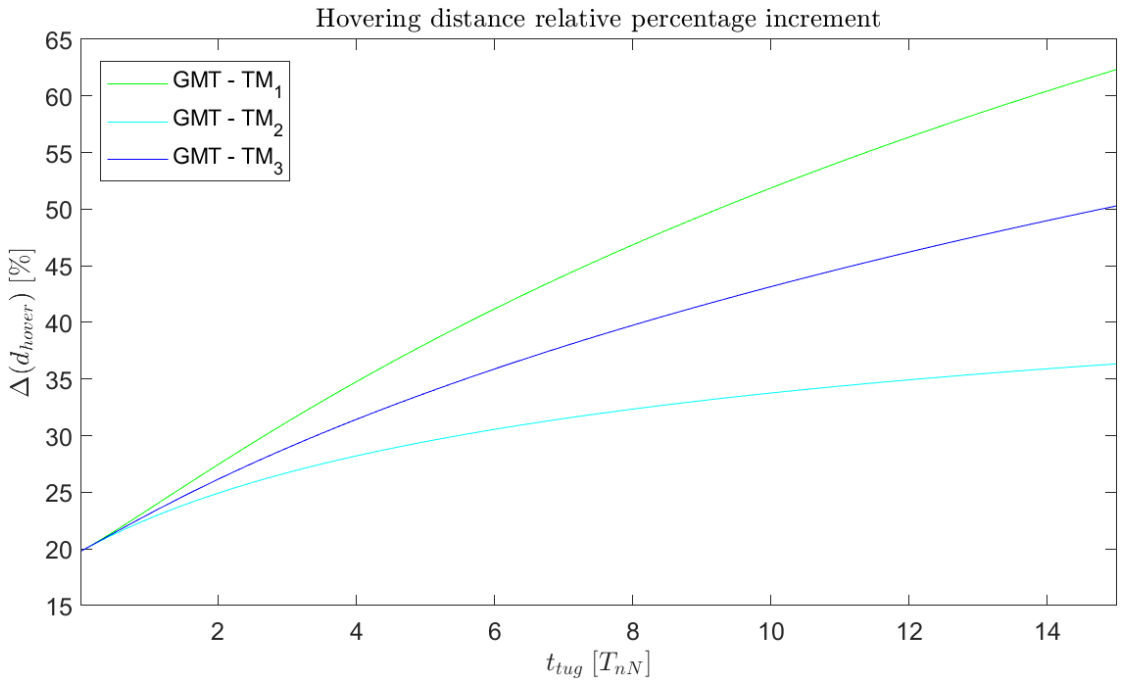

Figure 3.15: *GMT hovering distances percentage increase with respect of the GT one, as a function of the total tugging time.*

The results of the test case II are similar to the one presented here and are shown in Appendix B.

Tugging forces at interception and cut-off epochs

Given the hovering position, the force profile acting on the target is found using equations (3.27), (3.37),(3.41) for the GMT, and equation (2.22) for the GT. Figure 3.16 shows the tugging force acting on target I evaluated at interception epoch (i.e., initial force) and at MOID epoch (i.e., final force), for all the proposed TMs.

The same figure also shows the tugging force obtained with a traditional GT (i.e., black lines). The higher the total tugging time is, the smaller is the tugging force at interception for both GMT and GT. For low total tugging times, the GMT force starts higher than the one achieved by the same chaser performing a GT, whereas, for longer total tugging times the situation is inverted. However, within the propagation interval, the tugging force at MOID is always higher than the one achieved by the GT.

The tugging force's excursion, from interception to MOID epoch, is absent for TM1 (i.e., constant tugging force), it is smaller in TM3 with respect to TM2, and it is always higher for the classical GT, within the propagation interval. Examples of the tugging force profiles, for all TMs, are proposed in appendix B.

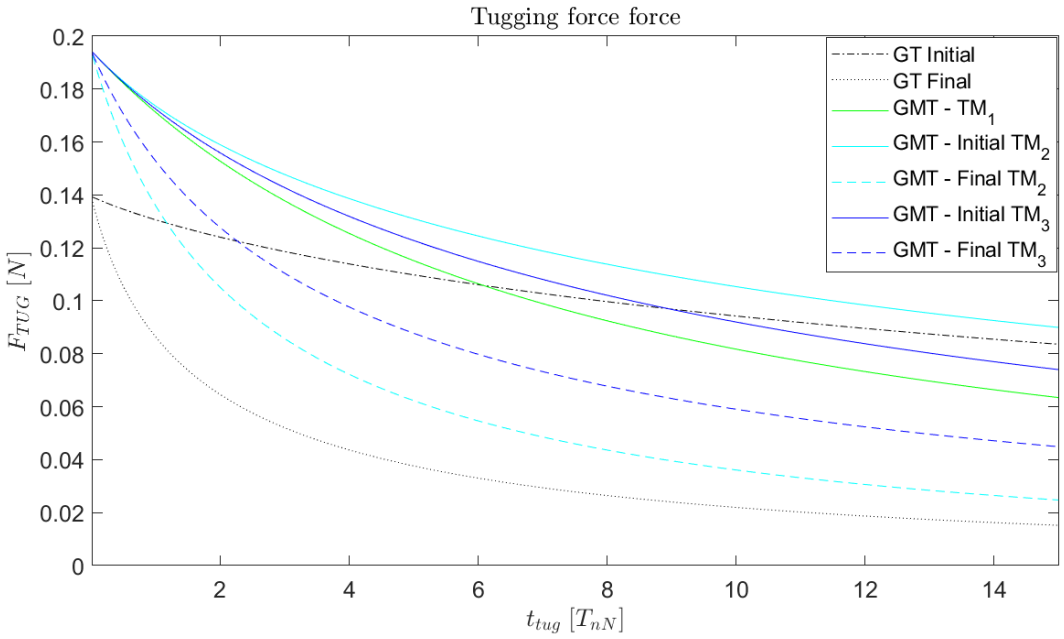

Figure 3.16: *Tugging force acting on target I at interception epoch, and at MOID one, as a function of the total tugging time for all the proposed GMT tugging modes and the GT.*

Considering the results obtained on target II, presented in figure 3.17, the situation is drastically altered. The gravitational interaction that shall be compensated by the PS is greater, being $m_{T1} >> m_{T2}$, and the bigger equivalent radius of target II shifts the maintainable hovering position farther away from the target itself.

The GMT force at interception epoch is always lower than the one of a traditional GT. However, the force excursion is still smaller for the GMT, leading to a higher interaction force at interception.

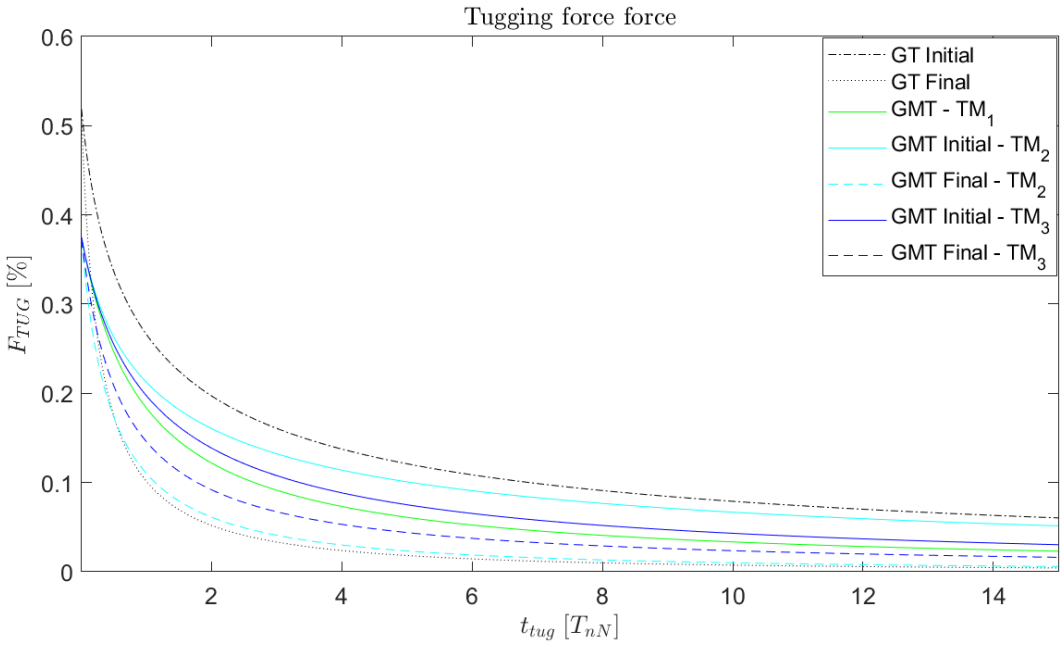

Figure 3.17: *Tugging force acting on target II at interception epoch, and at MOID, one as a function of the total tugging time for all the proposed GMT tugging modes and the GT.*

Total impulse imparted to the target

The total impulse imparted on the test targets is found with equation (3.34), applied to the proposed GMT tugging mode and to the GT. The results for target I, presented in figure 3.18, show that the total impulse achieved with any GMT tugging mode is always higher than the one obtained by a classical GT. The situation is again different for target II.

The selected GMT tugging mode starts to affect the results, and can lead to a situation (i.e., TM2) in which the total impulse transferred to the target is mostly lower than the one of a classical GT. This is visible in figure 3.19, and it is associated to a final GMT interaction force (i.e., at MOID epoch) that becomes either lower, or closer, with respect to the one achieved by the GT, at the same epoch.

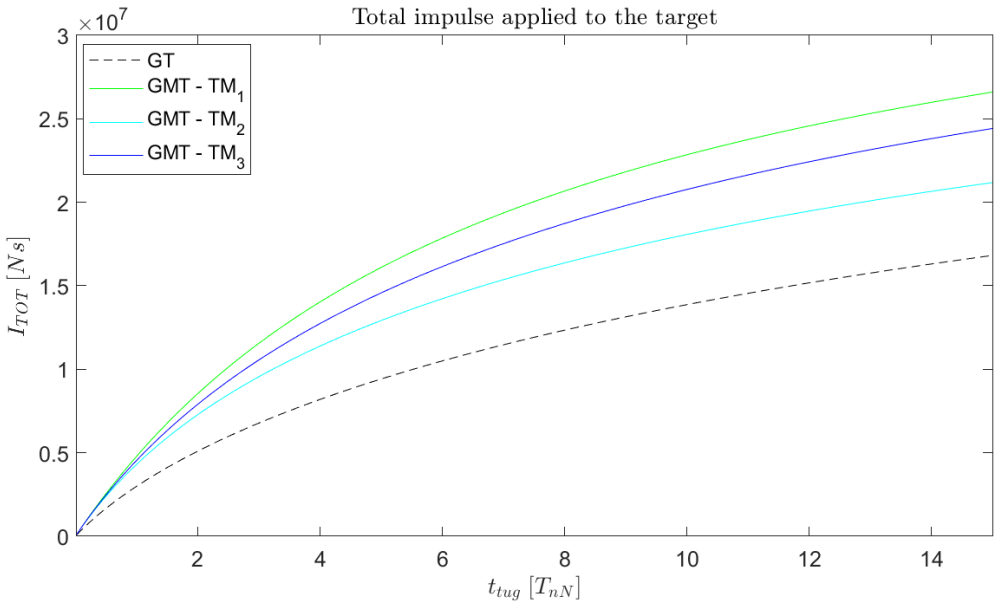

Figure 3.18: *Total impulse imparted on the test target I with all GMT tugging modes and the GT.*

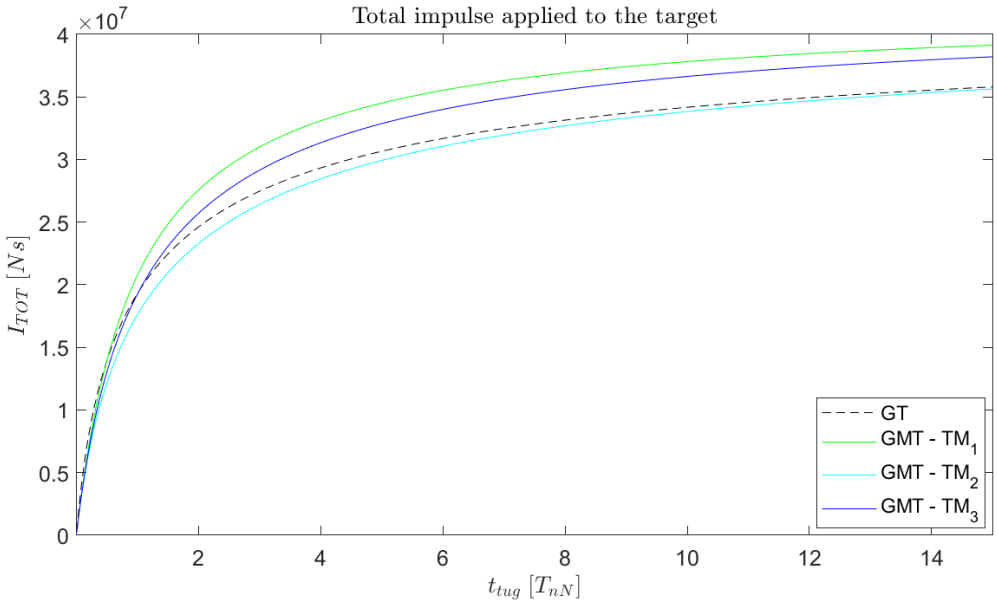

Figure 3.19: *Total impulse imparted on the test target II with all GMT tugging modes and the GT.*

Deflection at MOID

The achieved deflection for target I and II adoptiong GMT and GT are shown, respectively, in figures 3.20 and 3.21. The deflection of target I at any given total tugging time increases in all the GMT modes. Conversely, the results for target II show an opposite situation in which the GT is always performing better than any of the GMT modes, for same total tugging times.

The relative percentage increment in deflection with respect to the GT is shown in figures 3.22 and 3.23, and it is computed as

$$\Delta(dr) = 100\frac{dr_{GMT} - dr_{GT}}{dr_{GT}} \tag{3.46}$$

For a given total tugging time, the advantage of using any of the GMT modes is evident for target I, whereas is absent in target II. In both cases, the deflection relative increment reaches a maxima and drops. Such behaviour is not observed in TM2 applied to target II where, after a certain total tugging time, it is more convenient than all the other GMT tugging modes.

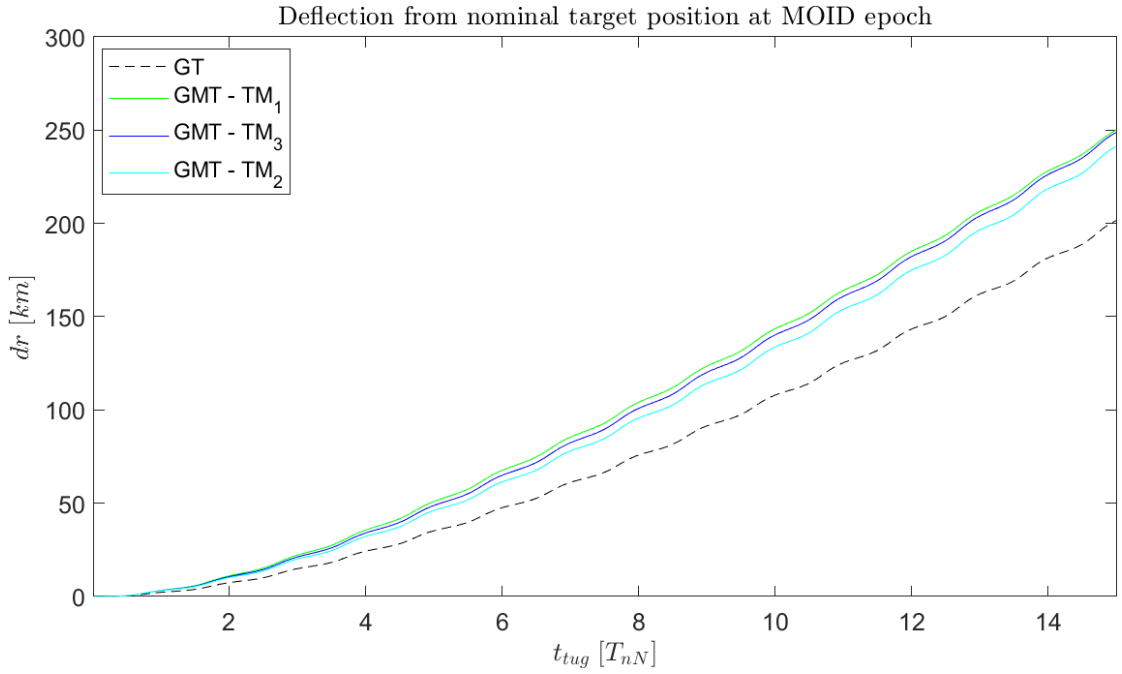

Figure 3.20: *Target I deflection at nominal MOID epoch achieved using the proposed GMT tugging modes and the traditional GT as a function of the total tugging time.*

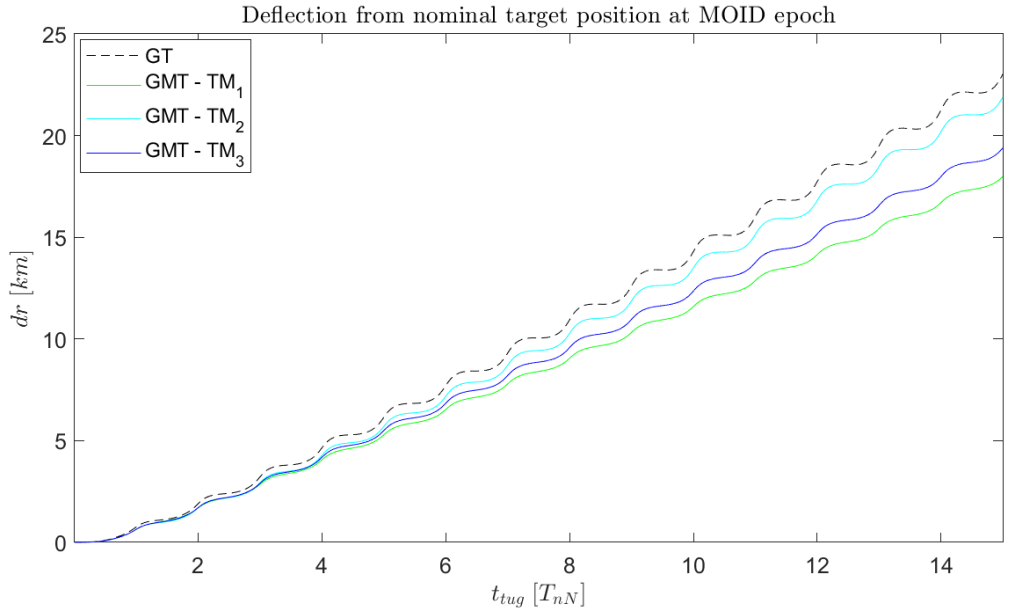

Figure 3.21: *Target II deflection at nominal MOID epoch achieved using the proposed GMT tugging modes and the traditional GT, as a function of the total tugging time.*

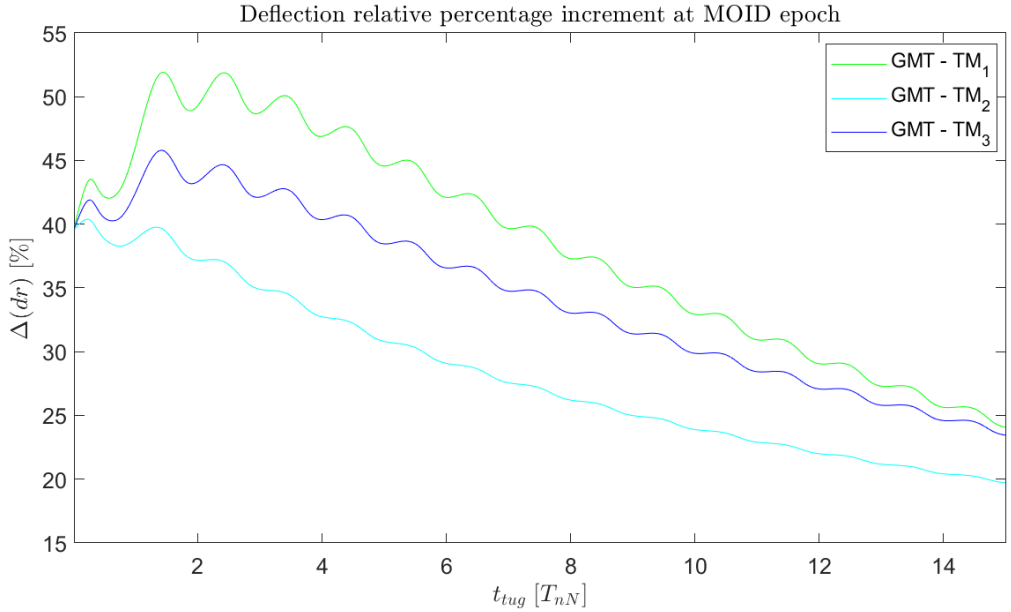

Figure 3.22: *Target I deflection percentage increment using GMT with respect GT evaluated at nominal MOID epoch.*

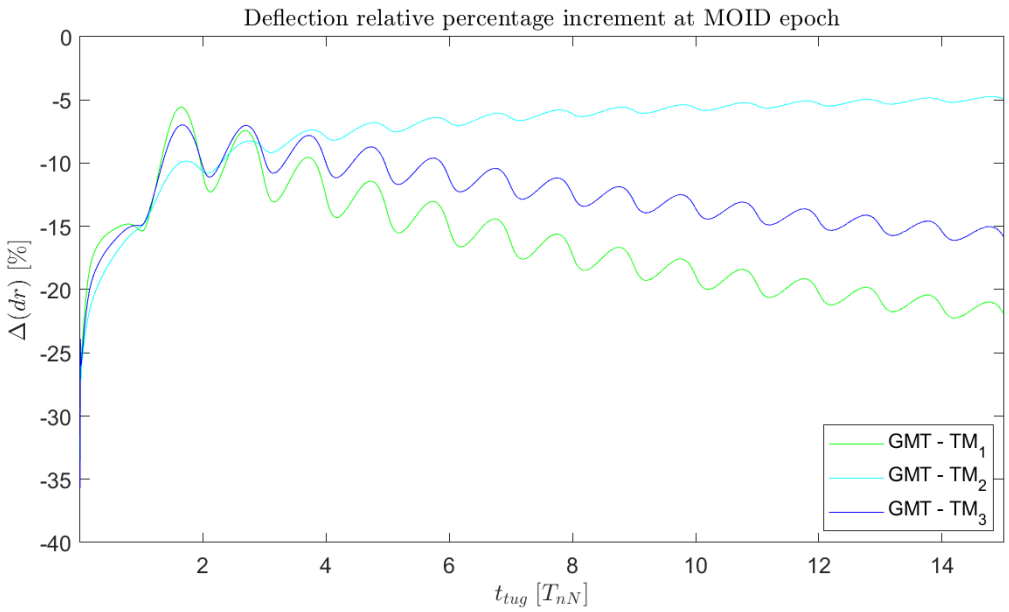

Figure 3.23: *Target II deflection percentage increment using GMT with respect GT evaluated at nominal MOID epoch.*

The relative percentage increment peak is connected to an interception close to the nominal target pericenter, whereas the oscillations are connected to an interception that is moving from the pericenter to the apocenter of the nominal target. This is also explored in the sensitivity analysis, section 3.3.5.

Chaser dry mass fraction

The dry mass fraction of the chaser is shown in figures 3.24 and 3.25. For small total tugging times, all the proposed GMT modes result into dry mass fractions that are higher than the ones of a traditional GT. The longer the total tugging time is, the lower is the dry mass fraction that allows the chaser to store the proper amount of fuel to sustain the tug (i.e., $\Pi_p = 1 - \Pi_{dry} = 1 - m_{dry}/m_{C0}$). This eventually leads to a situation in which the dry mass of GT becomes higher than the one required for GMT. Comparing the proposed GMT tugging modes, TM1 results to be the most fuel demanding approach, whereas TM2 the least fuel demanding one.

The aforementioned considerations are valid for both selected targets. Therefore, for a limited total tugging time interval, a chaser adopting any of the proposed GMT tugging modes can use the same amount of fuel (i.e., same dry mass fraction) to sustain a longer tug.

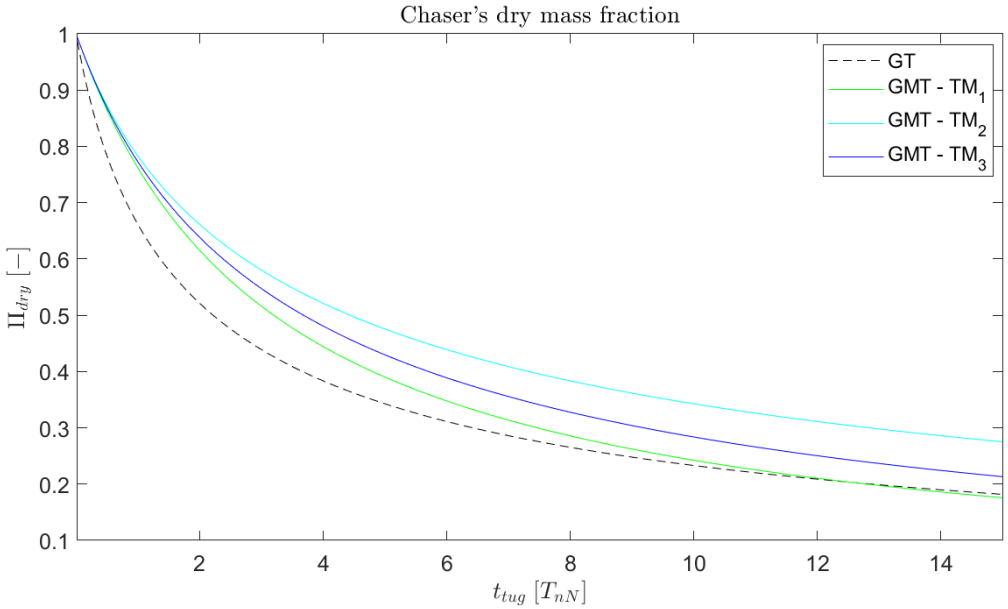

Figure 3.24: *Chaser dry mass fraction, for test target I tug, as a function of the total tugging time for all the GMT tugging modes and for GT.*

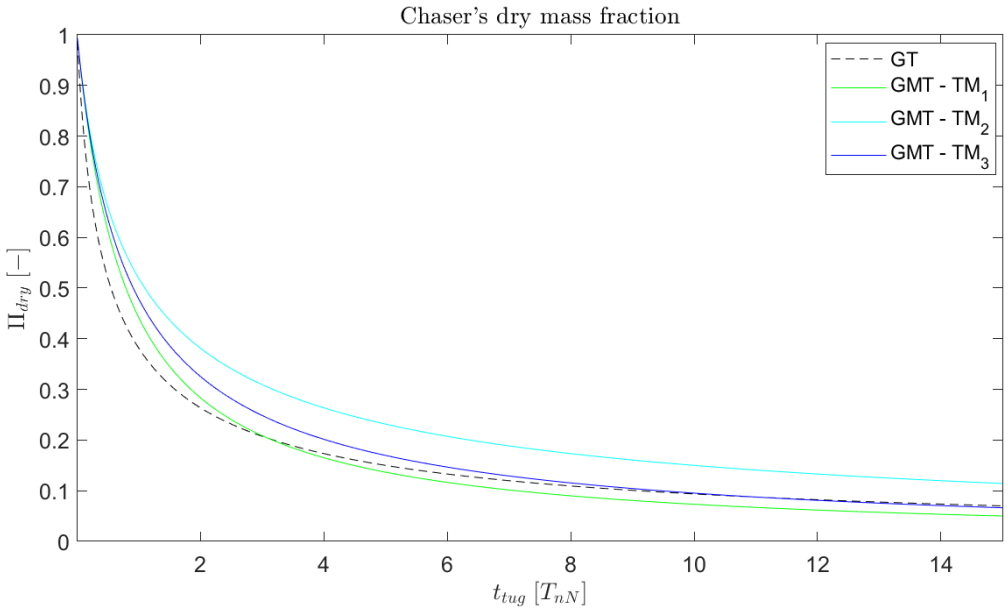

Figure 3.25: *Chaser dry mass fraction, for test target II tug, as a function of the total tugging time for all the GMT tugging modes and for GT.*

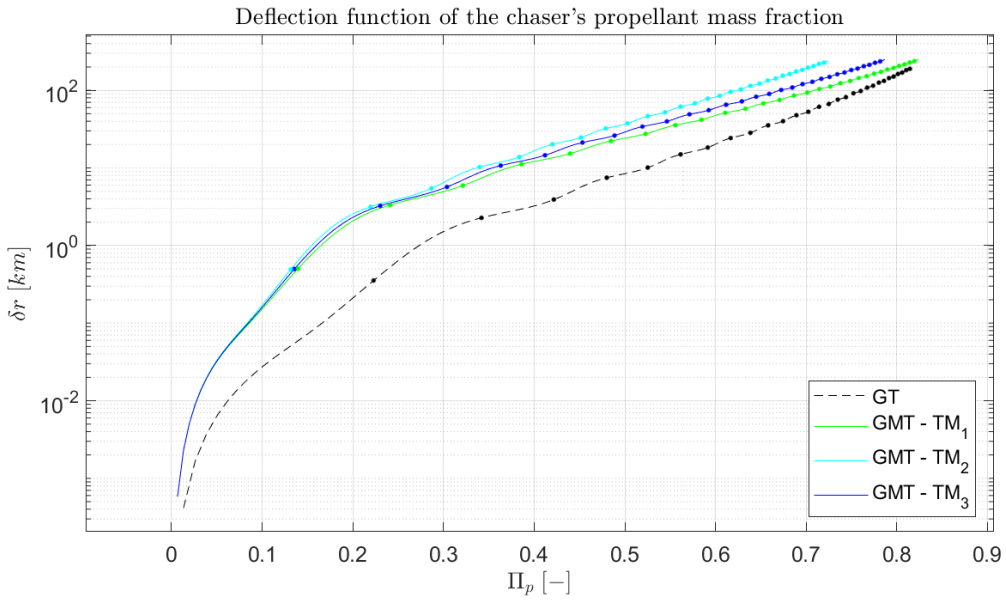

Figure 3.26: *Deflection of target I as a function of the chaser's propellant mass fraction. The dots are happening at a total tugging time multiple of $T_T/2$.*

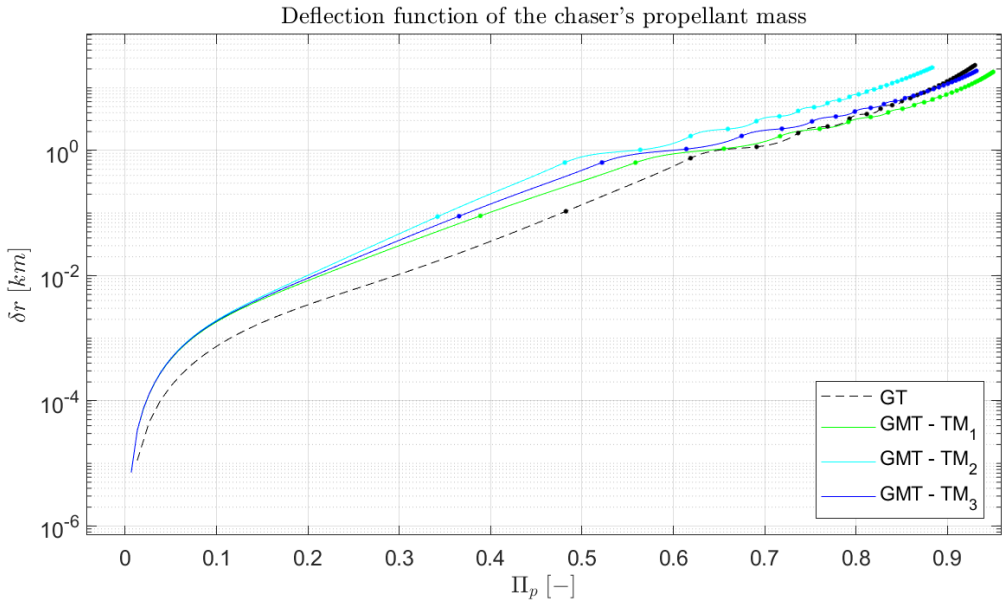

Figure 3.27: *Deflection of target II as a function of the chaser's propellant mass fraction. The dots are happening at a total tugging time multiple of $T_T/2$.*

This is more evident looking at the achieved deflection as a function of the chaser's propellant mass fraction, shown in figures 3.26 and 3.27. Note that, in these graphs the information about the total tugging time is lost and it reintroduced using dots collocated at a propellant mass fraction associated to a multiple of $t_{tug} = 0.5T_T$. The complete temporal link shall be retrieved using figures 3.24 and 3.25.

The deflection enhancements, using any of the GMT tugging modes, are comparable for small propellant mass fractions (i.e., for small total tugging times), but start to be dependant upon the GMT tugging mode for higher ones. In both test cases TM2 leads to the best deflection for a given fuel fraction, whereas TM1 leads to the worst result.

Chaser's magnetic dipole

The chaser's magnetic dipole magnitude that allows the GMT to take place, for target I and for any tugging modes, is shown in figure 3.28.

It is worth to recall that the magnetic dipole magnitude is assumed a priori, at the beginning of the analysis, by choosing a GMT tugging mode. The SMS shall be able to generate such dipole with the available power mass and shall be integrated within the available dry mass of the chaser, given the results of the static analysis.

A measure of the SMS efficiency is given by the SMM weighted over the actual power mass dedicated to its generation

$$\frac{\mu_{\epsilon\mu_T}}{m_{pw,\epsilon\mu}} \equiv \frac{\mu_{\epsilon\mu_T}}{(1-\alpha_{POD})PODm_{dry}} \tag{3.47}$$

and it is shown in figure 3.29.

The higher the total tugging time is, the higher is the required SMS efficiency since it is connected to a decreasing dry mass and to an increasing magnetic dipole magnitude to maintain the chosen TM. The SMS efficiency of all the GMT tugging modes is similar when small total tugging times are considered, but it starts to be dependant upon the chosen TM as the total tugging time increases. Comparing all TMs, TM1 requires the highest SMS efficiency to operate, which is set at MOID epoch (i.e., when the most demanding mass compensation is required). Conversely, the SMS efficiency for both TM2 and TM3 is set at interception epoch, and is minimum for TM2.

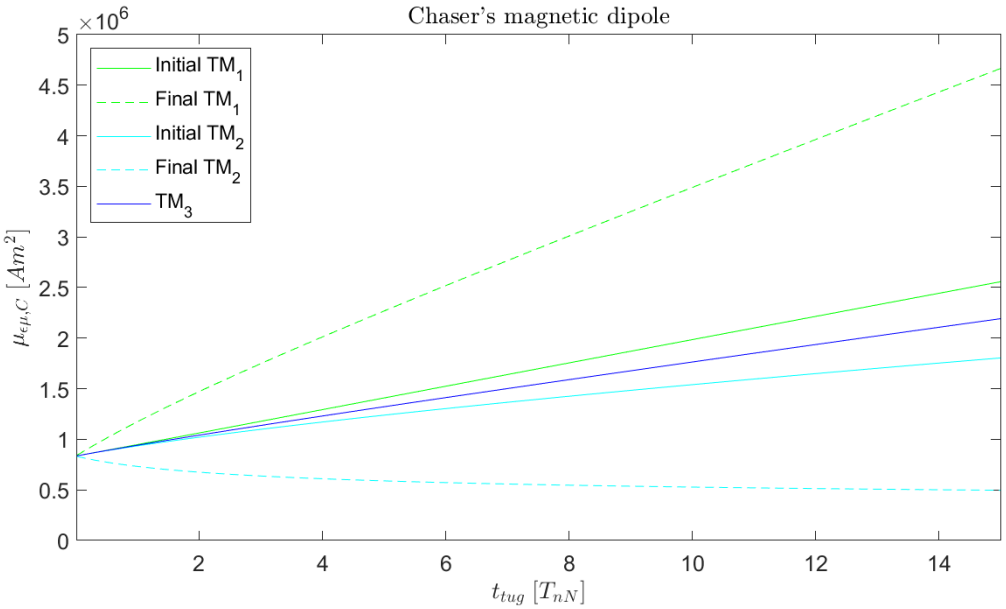

Figure 3.28: *Initial and final chaser's magnetic dipole magnitudes for all the proposed GMT tugging modes on target I.*

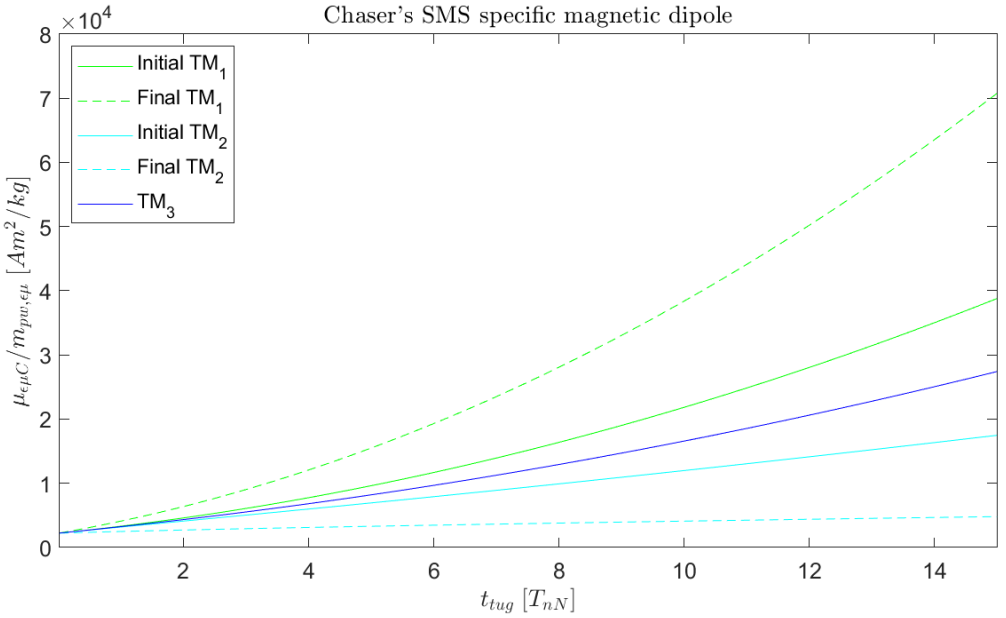

Figure 3.29: *Initial and final chaser's SMS efficiency for all the proposed GMT tugging modes on target I.*

As of target II, the results are similar and have an order of magnitude of the magnetic dipole that reaches values up to 10^8 $[Am^2]$.

3.3.5 Sensitivity Analysis

The sensitivity analysis aims to understand how the chaser and target properties are affecting the achieved deflection, the hovering distance, and how the SMS performance is impacted when the GMT is applied to the test cases presented in tables 3.5, 3.3 and 3.4. These are referred to as nominal values in the following discussion. The results are generated using the same procedure followed in sections 2.5 and 3.3, using the third tugging mode only (i.e., TM3). This choice is made in order to obtain more readable results for the SMS efficiency. The other TMs lead to similar results and are here omitted.

Sensitivity to the chaser performance parameters

Recalling equation (2.12), the sensitivity to the chaser performance is implemented considering a variable ξ_{th}/τ_{pw} ratio and a variable power mass repartition between the thrust and dipole generations (i.e., α_{POD}). A variation of ±90% with respect to the nominal values and a total tugging time of $1.5T_T$ are considered.

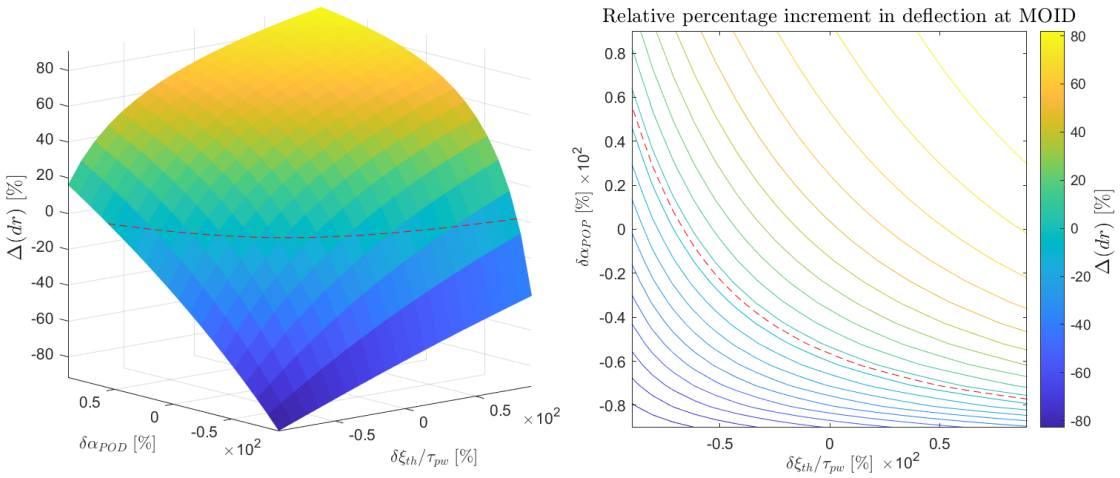

Figure 3.30: *Relative percentage increment in deflection as a function of the power mass repartition and the chaser thrusting performance for target I. The dashed red line is the zero-change result.*

Figure 3.30 shows the relative percentage increment in deflection at MOID, achieved using the GMT on target I. The improvement is increasing as the ξ_{th}/τ_{pw} ratio increases, meaning that either the PS is capable to generate a higher amount of thrust

per power dedicated to the system or, the PGS requires less mass to generate the required amount of overall power. The mass repartition between the PS and SMS has a positive effect in the achieved deflection when it increases, meaning that most of the power is redirected to propulsive purposes instead of dipole generation.

On the other hand, a high value of α_{POD} means that the SMS needs to generate a given magnetic dipole using less power mass available to the system and thus, its efficiency in doing so may increase. This is visible in figures 3.31 and 3.32 where the required dipole magnitude, the mass dedicated to SMS and, the specific magnetic dipole associated to the SMS subsystem are shown.

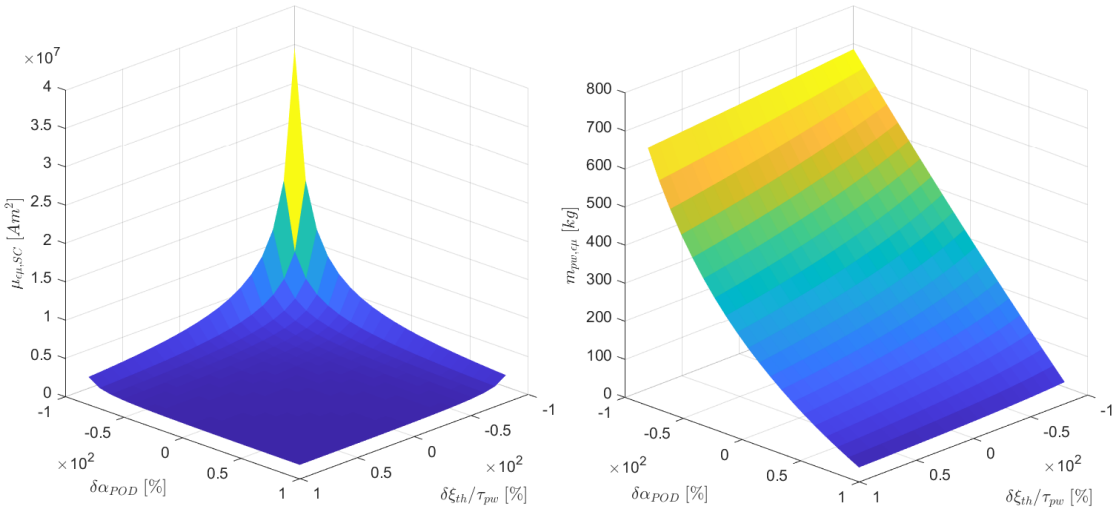

Figure 3.31: *Chaser magnetic dipole (on the left) and its power mass dedicated to the dipole generation (on the right) as function of the power mass repartition and the thrusting performance for target I.*

The chaser dry mass fraction is also affected by the variation of these parameters, leading to values that may not be achievable due to structural limitations (e.g., the chaser cannot be only fuel). Figure 3.31 shows that increasing the overall performance of the system, the dry mass reduction is amplified when the power repartition is in PS favour.

In addition, the overall performance enhancement allows the operations to happen at a closer relative distance in respect to the target, being the maximum achievable thrust higher for a fixed power mass dedicated to PS. Figure 3.34 shows that, the higher the overall performance is, the closer is the GMT hovering point to the GT one. Lowering the mass dedicated to the PS for a fixed performance restores a farther hovering position. Considering the target II results presented in figure 3.33, it is

possible to see how an improvement of the overall system performance can lead to positive deflection increment, at the considered total tugging time.

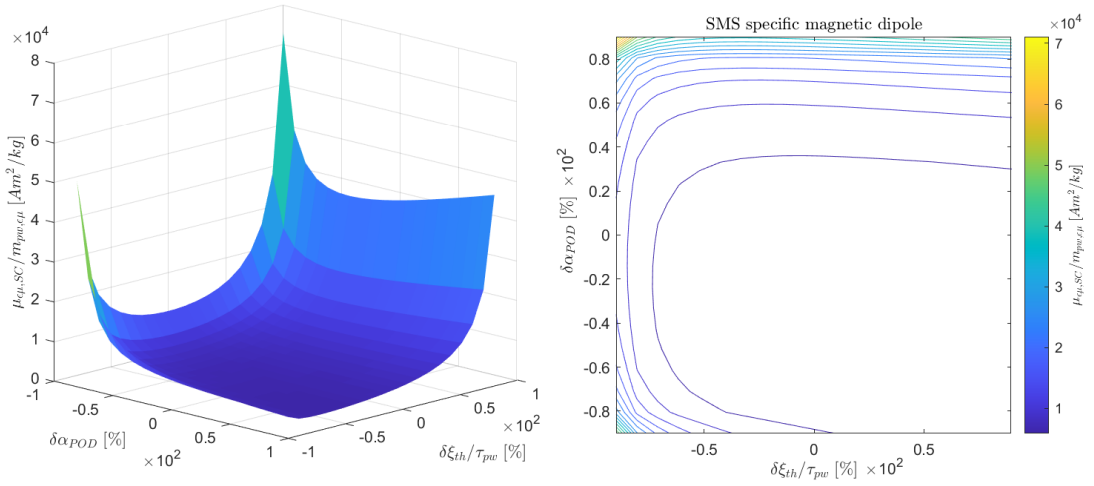

Figure 3.32: *SMS efficiency as function of the power mass repartition (i.e., α_{POD}) and the chaser thrusting performance for target I.*

Note that such increment is negative in the nominal case. For a massive and large target, this is the only way to improve the deflection, and it may not be achievable given the currently available performances (i.e., nominal ones) and structural limitations related to the chaser.

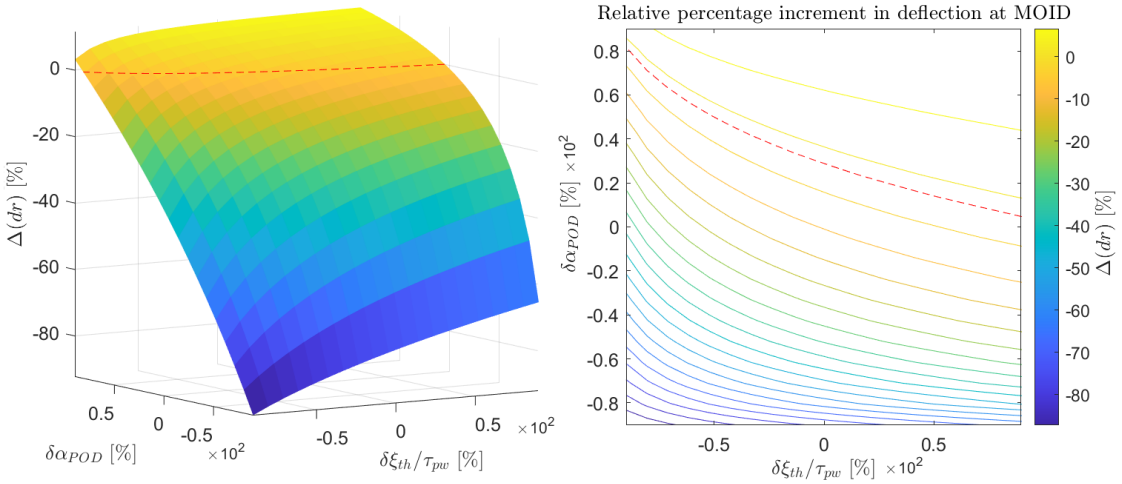

Figure 3.33: *Relative deflection increment as a function of the power mass repartition and the chaser thrusting performance for target II*

On the other hand, this is translated into an higher cost in therms of SMS efficiency that is increased by two order of magnitudes in respect target I results.

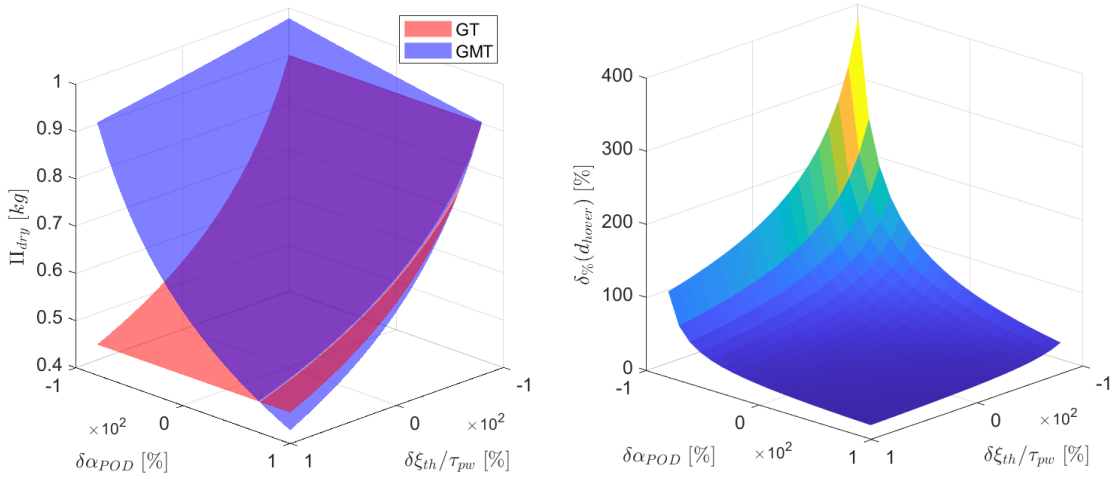

Figure 3.34: *Dry mass fraction (i.e., left graph) and relative hovering distance increment (i.e., right graph) as function of the power mass repartition and the chaser thrusting performance for target I.*

Deflection sensitivity to the magnetic amplification factor

The deflection sensitivity to the amplification factor is presented in figure 3.35 for only target II and focusing on the region in which the relative percentage increment obtained with the nominal tug is the highest (i.e., close to $t_{tug} = 1.6T_T$). Increasing the magnetic amplification factor allows to achieve a positive relative increment region, obtaining a better performance of the GMT with respect to the GT. The cost in terms of SMS performance is visible in figure 3.36 and indicates that, for a given fixed performance, lower is the tugging time and higher is the maximum amplification factor that can be adopted. At the same time, the hovering distance is increasing as the magnetic amplification factor increases.

It is important to note that, such increment in deflection performance is achieved imposing an initial magnetic interaction which is up to ten times higher than the local gravitational contribution. This does not actually lead to a cooperation between gravitational and magnetic forces, but rather to the latter predominance.

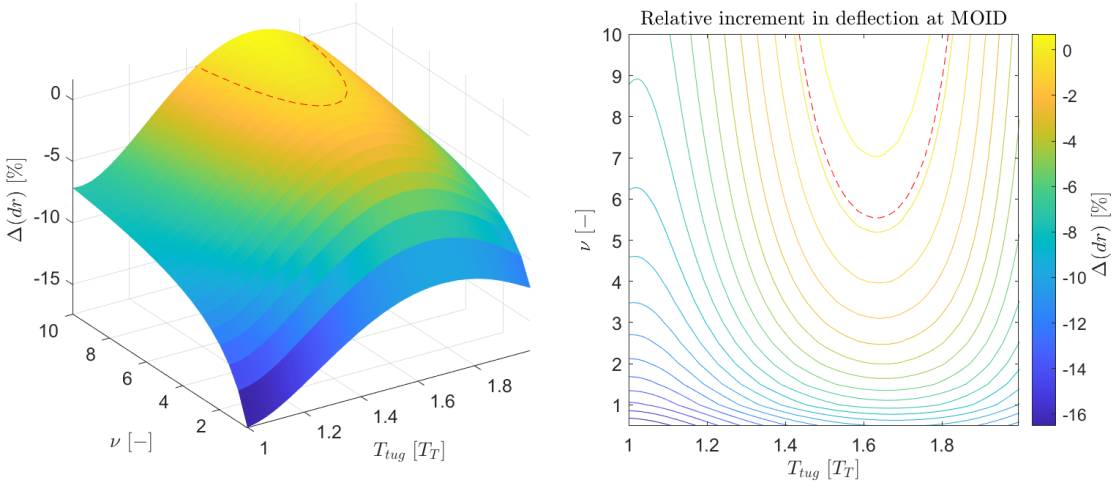

Figure 3.35: *Relative percentage deflection increment as a function of the magnetic amplification factor and the total tugging time.*

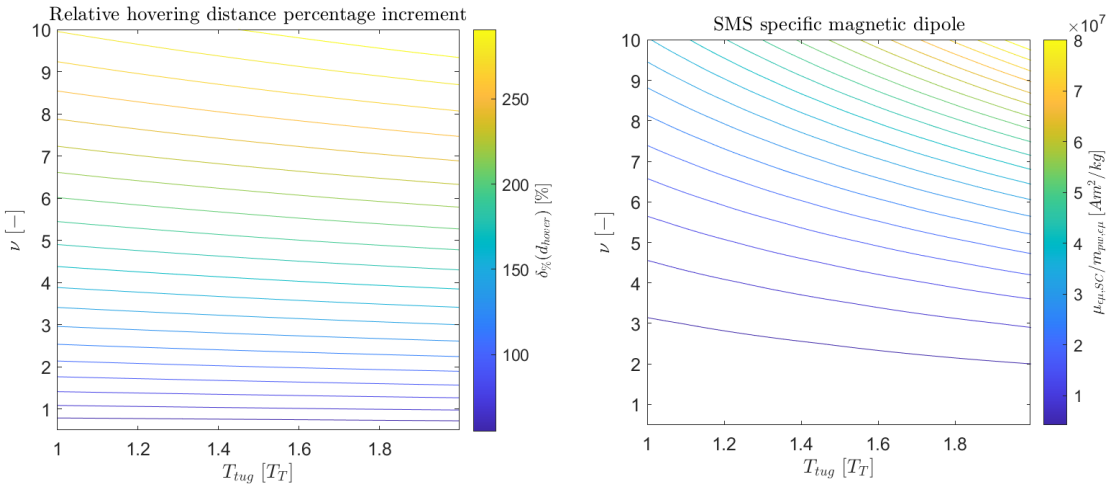

Figure 3.36: *SMS performance and hovering distance relative percentage increment as a function of the magnetic amplification factor and the total tugging time.*

Deflection sensitivity to the target semi-major axis and eccentricity

The deflection sensitivity to the target semi-major axis is performed assuming a variation of 0.1% of the nominal value, whereas the sensitivity to target eccentricity is considering eccentricities from 0.1 to 0.8. Figure 3.37 shows that the best relative increments in performance are located at a total tugging time close to a multiple of the orbital time of MOID. Meaning that, since the tug is assumed to happen from interception until MOID epoch, the increment is maximized when the GMT starts close to the nominal target's pericenter.

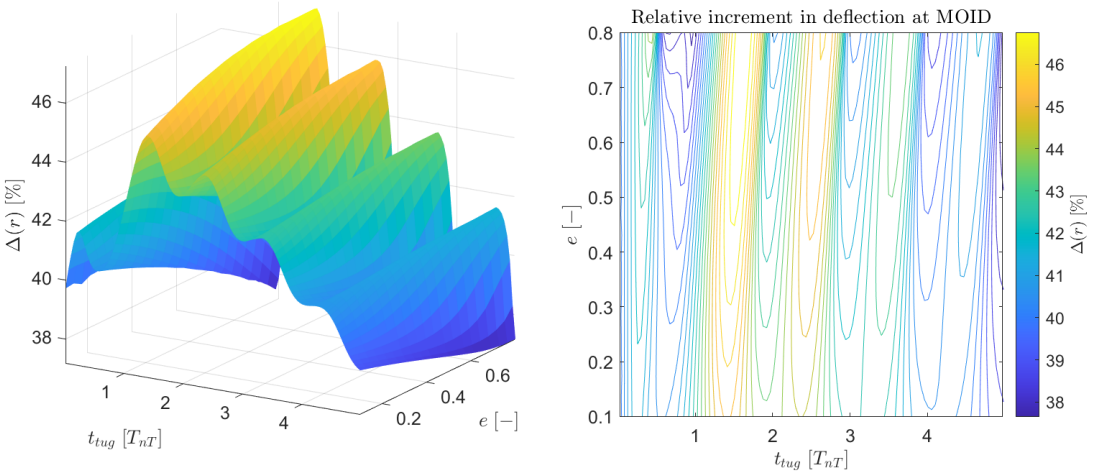

Figure 3.37: *Relative deflection increment as a function of the target eccentricity and the total tugging time.*

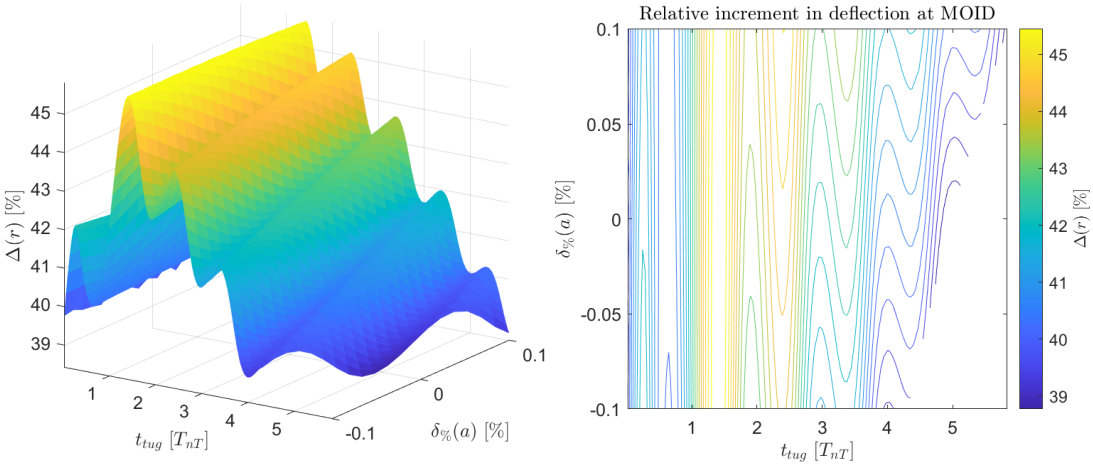

Figure 3.38: *Relative deflection increment as a function of the target semimajor axis and the total tugging time.*

Figures 3.38 also shows that, for different target orbital period (i.e., different MOID orbital times) the enhancements resulting from the adoption of the GMT are maximized if the tug stars at the first or second perigee passage, prior to the time of MOID.

Deflection sensitivity to the target radius

The deflection sensitivity to the target's equivalent radius is presented in figure 3.39 for the nominal target I. The results are computed assuming to change the radius at constant overall mass (i.e., target density changes).

The results show that, fixing the target mass, the GMT performs better with large target's equivalent radius and long total tugging time. The larger the equivalent radius is, the farther is the maintainable hovering position with respect to the target. The results also show that, the GMT is not performing well when the target's equivalent radius is lower than a threshold (i.e. dashed red line).

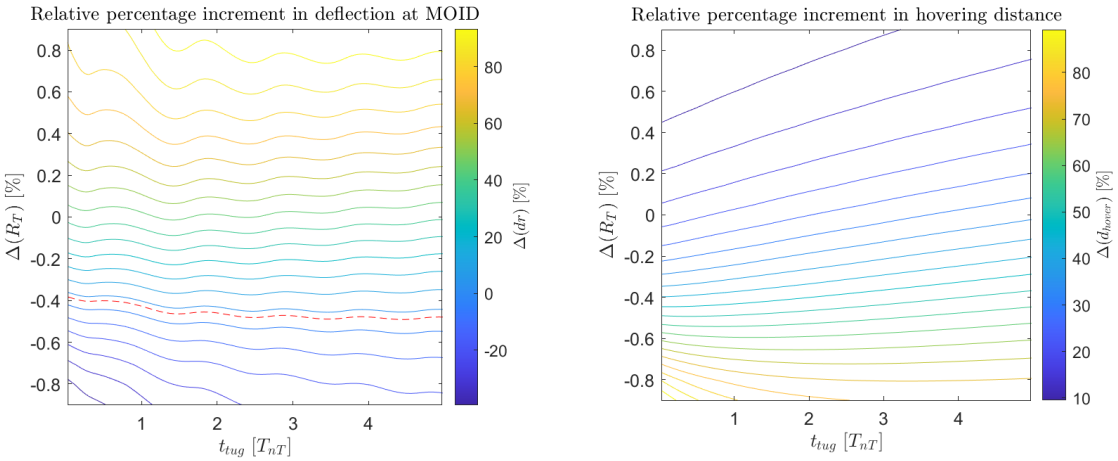

Figure 3.39: *Relative deflection increment as a function of the target radius and total tugging time, assuming a constant target mass.*

Letting the mass to change with the radius (i.e., retaining the nominal density), a more intuitive result is obtained and shown in figure 3.40. The smaller the radius is, the smaller is the target's mass, and the higher is the GMT performance. Decreasing the equivalent radius also shifts the GMT hovering distance closer to the one the GT.

Figure 3.41 presents the SMS efficiency for both analyses. For a fixed SMS efficiency, the smaller the equivalent radius is, the higher is the maximum total tugging time that the chaser can maintain.

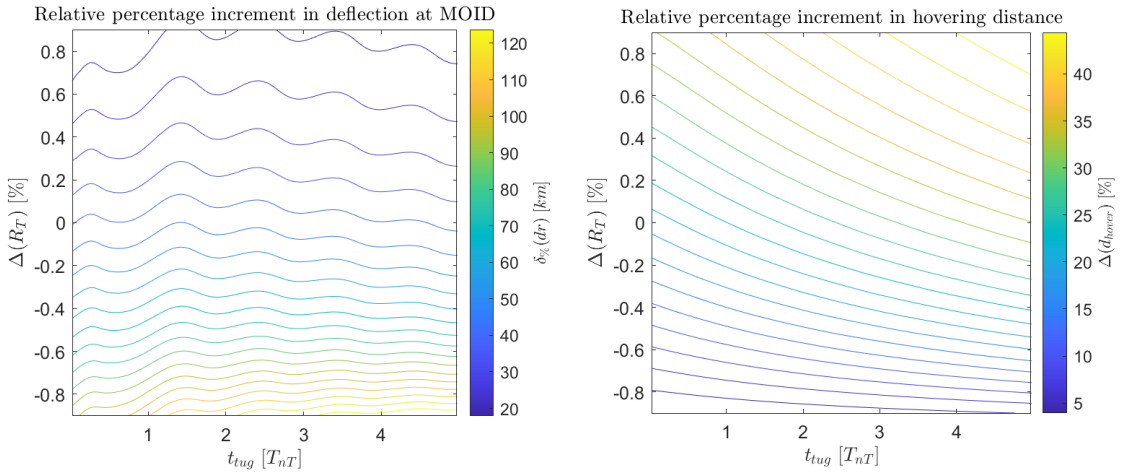

Figure 3.40: *Relative percentage increments in deflection at MOID (i.e., left graph) and hovering position, as a function of the target radius and total tugging time, assuming a constant target density.*

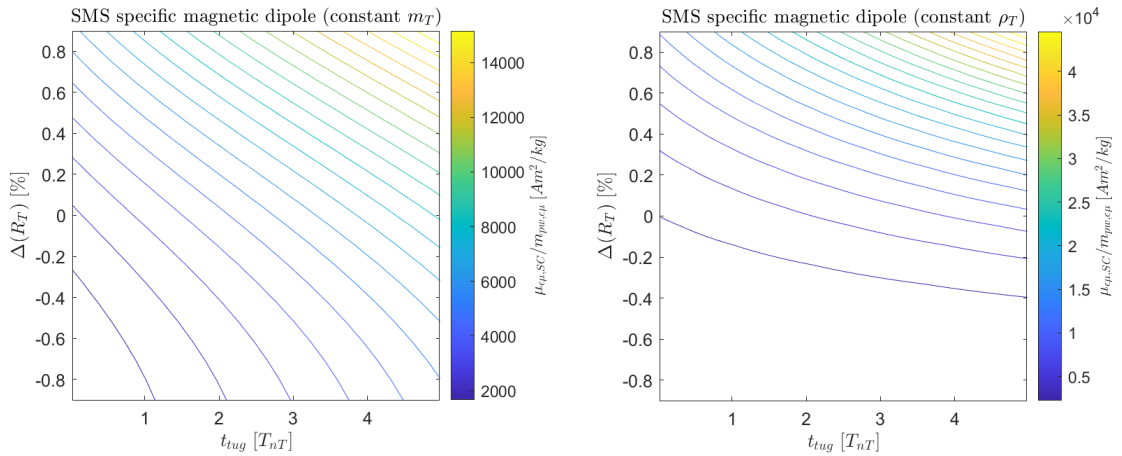

Figure 3.41: *SMS efficiency as a function of the target radius and total tugging time, assuming either constant target density or constant target mass.*

Deflection Sensitivity to the chaser mass at interception epoch

Figure 3.42 shows the achieved deflection and the chaser's dry mass using GMT and GT, for increasing chaser's mass at interception epoch. The analysis is done considering $m_{C0} \in [1500, 10000]$ kg.

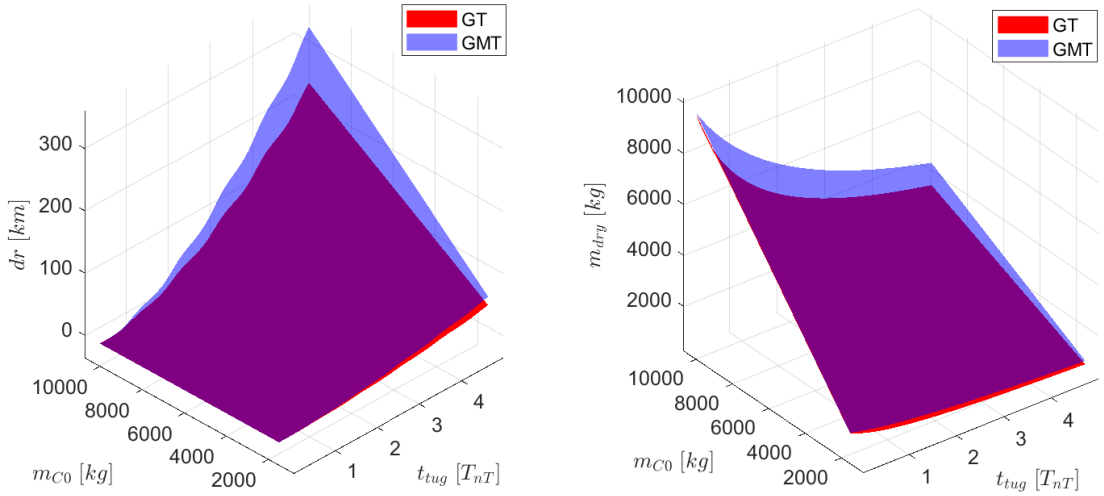

Figure 3.42: *Achieved deflection (i.e., left graph) and chaser's dry mass (i.e., right graph) as a function of the total tugging time and chaser's mass at interception*

The higher the chaser's mass at interception is, the higher is the chaser's dry mass. Being the maximum thrust of the chaser proportional to the dry mass, the chaser can maintain the hover at the same position as the nominal case. This leads to a greater LTA on the target, due to the higher chaser's mass, and to an higher achieved deflection at MOID epoch. However, the relative deflection increment of the GMT with respect to the GT is not affected, and remains the same as the nominal case (i.e., 3.22). Moreover, the higher the chaser's mass is, the higher is the required chaser's dipole that allows to operate with the selected TM (i.e., TM3 in this case). The SMS efficiency results to be the same as nominal case (i.e., 3.28).

Deflection sensitivity to the cut-off time

The model presented in section 3.3 assumes a thrusting arc that starts at interception epoch, and ends at MOID epoch. Referring to the nominal case and considering a given total tugging time $\bar{t}_{tug}$, the maintainable hovering position $\bar{d}_{hover}$ with respect to the target is known. This means that, any thrusting arc with the same total tugging time $\bar{t}_{tug}$ is maintainable if the relative hovering distance is kept at $\bar{d}_{hover}$. This

also means that the SMS efficiency is common for thrusting arcs with equal $\bar{t}_{tug}$.

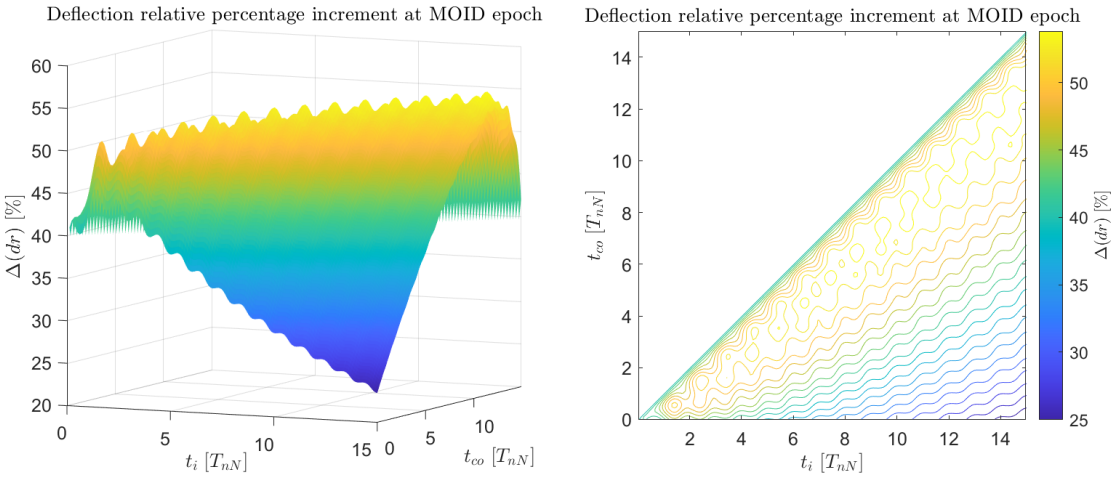

Figure 3.43: *Relative deflection increment as a function of the interception epoch and cut-off epoch (epochs prior to the MOID condition)*

Figure 3.43 shows the relative deflection increment at MOID of GMT with respect to GT, as a function of the interception epoch and the cut-off epoch prior to the MOID condition. The results are obtained following the same procedure described in section 3.3, introducing the cut-off epoch t_{co} such that the total tugging time is $\bar{t}_{tug} = t_i - t_{co}$ with $t_{co} < t_i$. The deflection at MOID is computed using (2.20) and (2.21), considering the reduced thrusting arc.

Referring to the MOID epoch, the farther away in time the GMT operates, the greater is the advantage in using it with respect to the GT. The maximum relative percentage increment is associated to short thrusting arcs close to the interception epoch t_i, with a $\bar{t}_{tug}$ comparable with the one associated to the maximum performance identified in figure 3.22.

3.4 Relative target-chaser dynamics

The results obtained in section 3.3 are referred to a GMT performing a hover at a fixed point aligned with the target velocity vector, without considering any other forces contribution than the gravitational-magnetic one between the objects. The chaser is designed assuming the worst orientation coefficient identified in sections 3.2, thus imposing to the SMS the generation of the most demanding magnet dipole to allow the tug to be maintainable for the total tugging time.

The relative dynamic model aims to understand the impact of a non-optimal relative configuration of the magnetic dipoles from a deflection point of view, when the proposed GMT is adopted to hover close to the target. The actual motion of the objects about the primary is considered and an initial target's tumbling state is assumed. The target deflection performance as well as the chaser's AOCS requirements are then derived and discussed for the test target I (i.e., Apophis) reported in table 3.4 and 3.3. The analysis is done directly propagating in time the dynamics using a model implement in Simulink® (figure 3.44).

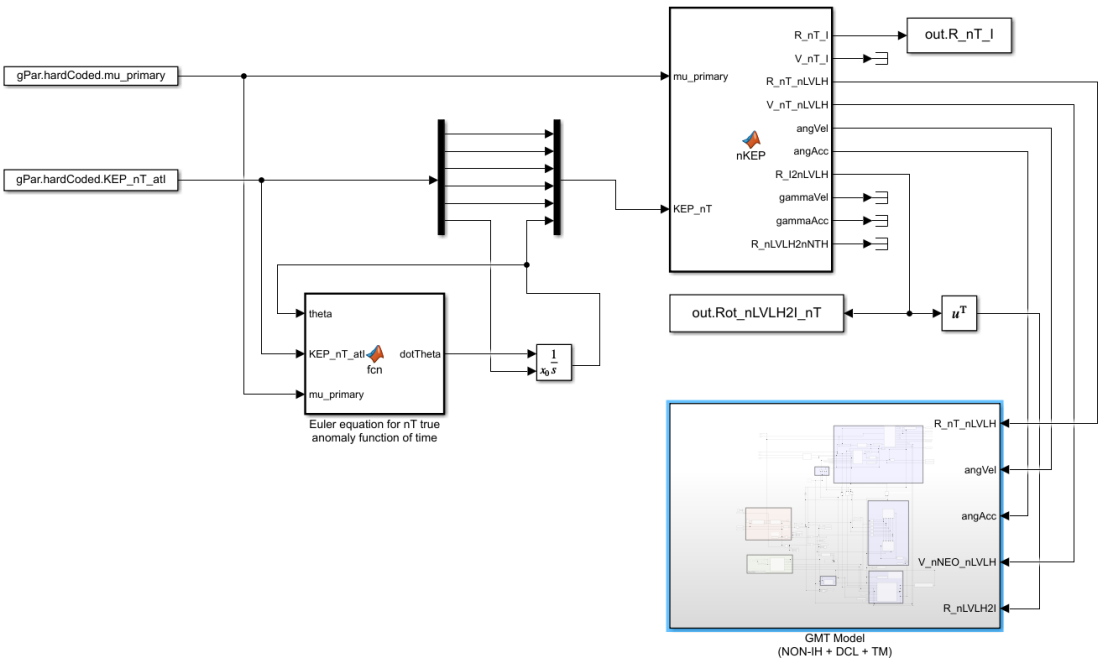

Figure 3.44: *View of the model developed in Simulink®*

The assumptions made in section 3.1 are here extended with

1. The target and the chaser are the only objects orbiting the primary, which is considered as a central body.

2. The chaser is able to perfectly control the relative position with respect to the target.

3. The chaser is able to retrieve the target's dipole azimuth and elevation in the target's NTH frame.

4. The chaser's AOCS can generate thrusts along the axes of $\mathcal{B}_{\mathcal{C}}$ frame, using ion engines with common performance.

5. No perturbations other than the magnetic interaction and the mutual gravitational contributions of the objects and primary are considered.

6. The chaser's internal mass repartition, the nominal relative hovering distance and maximum magnetic dipole magnitude are set by the GMT model presented in section 3.3, adopting TM3.

7. The relative hovering distance from the target can be increased, to satisfy the RTS, and the chaser's is capable to maintain the adapted nozzle configuration condition.

3.4.1 Dynamic models

The translational and rotational dynamic models are constructed starting from the linear and angular inertial dynamic equations presented in section 2.6, which are then used to derive the relative translational dynamics of both the deflected target with respect to the nominal one and the chaser with respect to the deflected target.

Absolute dynamics

Referring to figure 3.45 and using equation (2.30), the objects motion about the central body can be written in the ecliptic inertial frame centred at the primary as

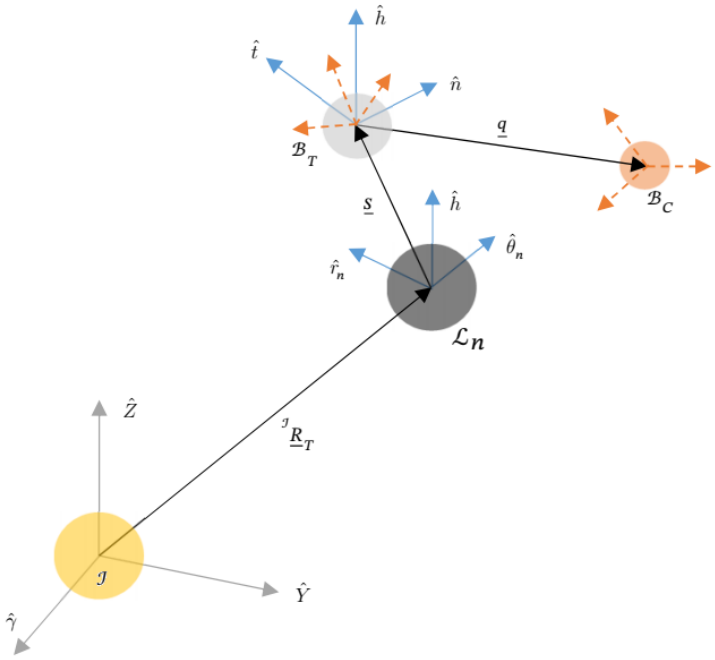

Figure 3.45: *Overview of the utilized frames of reference.*

$$\begin{cases} {}^{\mathcal{J}}\ddot{\underline{R}}_T = -\mu_{sun}\dfrac{{}^{\mathcal{J}}\underline{R}_T}{{}^{\mathcal{J}}R_T^3} + \mu_C\dfrac{{}^{\mathcal{J}}\underline{r}}{{}^{\mathcal{J}}r_C^3} + \dfrac{{}^{\mathcal{J}}\underline{F}_{\epsilon\mu C\to T}}{m_T} \\ {}^{\mathcal{J}}\ddot{\underline{R}}_C = -\mu_{sun}\dfrac{{}^{\mathcal{J}}\underline{R}_C}{{}^{\mathcal{J}}R_C^3} - \mu_T\dfrac{{}^{\mathcal{J}}\underline{r}}{{}^{\mathcal{J}}r_C^3} + \dfrac{{}^{\mathcal{J}}\underline{F}_{\epsilon\mu T\to C}}{m_C} + \dfrac{{}^{\mathcal{J}}\underline{F}_{th}}{m_C} \\ {}^{\mathcal{J}}\underline{R}_i(t_0) = {}^{\mathcal{J}}\underline{R}_{i,0} \\ {}^{\mathcal{J}}\dot{\underline{R}}_i(t_0) = {}^{\mathcal{J}}\dot{\underline{R}}_{i,0} \\ {}^{\mathcal{J}}\underline{r} \triangleq {}^{\mathcal{J}}\underline{R}_C - {}^{\mathcal{J}}\underline{R}_T \\ \mu_{\epsilon\mu_i} \triangleq Gm_i \end{cases} \tag{3.48}$$

where $\mathcal{J}$ is the selected inertial frame, ${}^{\mathcal{J}}\underline{R}_i, i = \{T, C\}$ is the absolute position vector of the object i, ${}^{\mathcal{J}}\underline{r}$ is the relative position vector of the chaser with respect to the target, ${}^{\mathcal{J}}\underline{F}_{\epsilon\mu i\to j}$ is the magnetic force felt by object i due to object j defined in section 2.3, and ${}^{\mathcal{J}}\underline{T}_{th}$ is the control force developed by the PS of the chaser.

The absolute rotational dynamics is retrieved applying equation (2.31) to both target and chaser in their body fixed frames as

$$\begin{cases} \mathbf{J}_T \, {}^{\mathcal{B}_\mathcal{T}}\underline{\dot{\omega}}_{\mathcal{B}_\mathcal{T}\mathcal{I}} + \dot{\mathbf{J}}_T \, {}^{\mathcal{B}_\mathcal{T}}\underline{\omega}_{\mathcal{B}_\mathcal{T}\mathcal{I}} + \left[{}^{\mathcal{B}_\mathcal{T}}\underline{\omega}_{\mathcal{B}_\mathcal{T}\mathcal{I}}\right]^\wedge \mathbf{J}_T \, {}^{\mathcal{B}_\mathcal{T}}\underline{\omega}_{\mathcal{B}_\mathcal{T}\mathcal{I}} = {}^{\mathcal{B}_\mathcal{T}}\underline{T}_{\epsilon\mu C\to T} \\ \mathbf{J}_C \, {}^{\mathcal{B}_\mathcal{C}}\underline{\dot{\omega}}_{\mathcal{B}_\mathcal{C}\mathcal{I}} + \dot{\mathbf{J}}_C \, {}^{\mathcal{B}_\mathcal{C}}\underline{\omega}_{\mathcal{B}_\mathcal{C}\mathcal{I}} + \left[{}^{\mathcal{B}_\mathcal{C}}\underline{\omega}_{\mathcal{B}_\mathcal{C}\mathcal{I}}\right]^\wedge \mathbf{J}_C \, {}^{\mathcal{B}_\mathcal{C}}\underline{\omega}_{\mathcal{B}_\mathcal{C}\mathcal{I}} = {}^{\mathcal{B}_\mathcal{C}}\underline{T}_{\epsilon\mu T\to C} + {}^{\mathcal{B}_\mathcal{C}}\underline{T}_{as} \\ \dot{\mathbf{R}}_{\mathcal{I}\to\mathcal{B}_i} = -\left[{}^{\mathcal{B}_i}\underline{\omega}_{\mathcal{B}_i\mathcal{I}}\right]^\wedge \mathbf{R}_{\mathcal{I}\to\mathcal{B}_i} \\ {}^{\mathcal{B}_i}\underline{\omega}_{\mathcal{B}_i\mathcal{I}}(t_0) = {}^{\mathcal{B}_i}\underline{\omega}_{\mathcal{B}_i\mathcal{I},0} \\ \mathbf{R}_{\mathcal{I}\to\mathcal{B}_i}(t_0) = \mathbf{R}_{\mathcal{I}\to\mathcal{B}_i,0} \end{cases} \tag{3.49}$$

where $\mathcal{B}_i, i = \{T, C\}$ is the principal body fixed frame of object i centred at its CM, ${}^{\mathcal{B}_\mathcal{C}}T_{\epsilon\mu i\to j}$ is the magnetic torque felt by object i defined in section 2.3, and ${}^{\mathcal{B}_\mathcal{C}}T_{as}$ is the control torque generated by the chaser's AOCS.

Note that the target cannot control its attitude (i.e., it is non-cooperative) and the chaser's control torque can be achieved either with an external action (e.g., thrusters, magnetic interaction) or by exploiting internal angular momentum storing devices (e.g., inertial wheels, controlled moment gyro) whose dynamics is here not considered.

Target relative translational dynamics

The target relative translational dynamics with respect to the nominal one, seen by the inertial frame, is retrieved using equations (2.30) and (2.29) as

$${}^{\mathcal{I}}\underline{\ddot{r}}_T \triangleq {}^{\mathcal{I}}\underline{\ddot{R}}_T - {}^{\mathcal{I}}\underline{\ddot{R}}_{nT} = -\mu_\odot\left(\frac{{}^{\mathcal{I}}\underline{R}_T}{{}^{\mathcal{I}}R_T^3} - \frac{{}^{\mathcal{I}}\underline{R}_{nT}}{{}^{\mathcal{I}}R_{nT}^3}\right) + \mu_C\frac{{}^{\mathcal{I}}\underline{r}}{{}^{\mathcal{I}}r^3} + \frac{{}^{\mathcal{I}}\underline{F}_{\epsilon\mu C\to T}}{m_T} \tag{3.50}$$

Considering the nominal target LVLH (i.e., $\mathcal{L}_n$) frame and using (2.35), the LHS of equation 3.50 is expanded. This leads to the ODE that describes the deflected target dynamics with respect to the nominal one, seen by the $\mathcal{L}_n$ frame and written in the same frame components

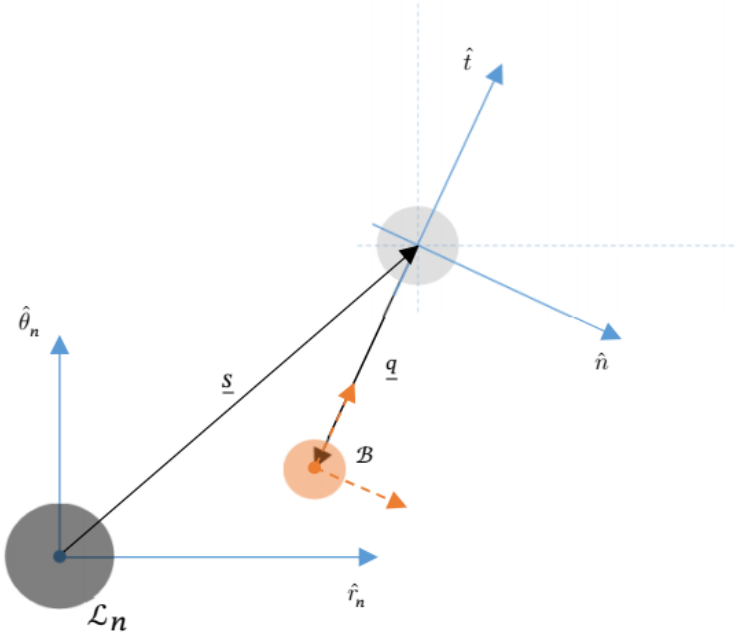

Figure 3.46: *Chaser (i.e., red) non-inertial hovering about the deflected target (i.e., light grey) velocity unit vector.*

$$
\begin{cases}
\ddot{\underline{s}} = & -\mu_{\odot}\left(\dfrac{{}^{\mathcal{L}_n}\underline{R}_T}{R_T^3} - \dfrac{{}^{\mathcal{L}_n}\underline{R}_{nT}}{R_{nT}^3}\right) + \\
& -\left(\left[{}^{\mathcal{L}_n}\underline{\Omega}_{L_nI}\right]^{\wedge}\left(\left[{}^{\mathcal{L}_n}\underline{\Omega}_{L_nI}\right]^{\wedge}\underline{s}\right) + \left[{}^{\mathcal{L}_n}\dot{\underline{\Omega}}_{L_nI}\right]^{\wedge}\underline{s} + 2\left[{}^{\mathcal{L}_n}\underline{\Omega}_{L_nI}\right]^{\wedge}\dot{\underline{s}}\right) + \\
& +\mu_C\dfrac{{}^{\mathcal{L}_n}\underline{r}}{{}^{\mathcal{L}_n}r^3} + \dfrac{{}^{\mathcal{L}_n}\underline{F}_{\epsilon\mu C\to T}}{m_T} \\
{}^{\mathcal{L}_n}\underline{R}_T = & {}^{\mathcal{L}_n}\underline{R}_{nT} + \underline{s}; \\
\dot{\underline{s}}(t_i) = & [0,0,0]^T \\
\underline{s}(t_i) = & [0,0,0]^T
\end{cases}
\tag{3.51}
$$

where $\underline{s}$ is the deflected target relative position to the nominal target, $\dot{\underline{s}}$ is its relative velocity seen in $\mathcal{L}_n$ frame, ${}^{\mathcal{L}_n}\underline{R}_{nT}$ is the absolute position of the nominal target, and vectors ${}^{\mathcal{L}_n}\underline{\Omega}_{L_nI}$ and ${}^{\mathcal{L}_n}\dot{\underline{\Omega}}_{L_nI}$ are the angular velocity and acceleration of $\mathcal{L}_n$ with respect to $\mathcal{I}$ computed using equations (2.36) and (2.37) applied to the nominal target.

Note that equation (3.51) initial conditions are obtained considering that the deflected and nominal targets have the same state vector at interception epoch.

Nominal target trajectory

The nominal target trajectory is reconstructed using equation (2.7) and integrating equation (2.9) to find the relation between the nominal true anomaly of the target and the propagation time. The result is then projected as

$$^{\mathcal{L}n}\underline{R}_{nT} = \mathbf{R}_{\mathcal{J}\to\mathcal{L}n}\,{}^{\mathcal{J}}\underline{R}_{nT} \equiv r_{nT}\hat{r_n} \tag{3.52}$$

where $\hat{r_n}$ is the first unit vector of $\mathcal{L}_n$.

Chaser relative translational dynamics

The chaser relative translational dynamics is written with respect to the deflected target and expressed in its NTH frame (i.e., $\mathcal{N}$). This is done to ease the application of the proposed DCL and the adoption of a fixed hovering position collocated along the deflected target velocity unit vector.

Using again equations (2.30), the dynamics can be written in the inertial frame as

$$\begin{cases} {}^{\mathcal{J}}\ddot{\underline{r}} & = -\tilde{\mu}\dfrac{{}^{\mathcal{J}}\underline{r}}{{}^{\mathcal{J}}r^3} + \mu_{\odot}\left(\dfrac{{}^{\mathcal{J}}\underline{R}_T}{{}^{\mathcal{J}}R_T^3} - \dfrac{{}^{\mathcal{J}}\underline{R}_{nT}}{{}^{\mathcal{J}}R_{nT}^3}\right) + \dfrac{{}^{\mathcal{J}}\underline{F}_{\epsilon\mu T\to C}}{m_{red}} + \dfrac{{}^{\mathcal{J}}F_{th}}{m_C} \\ \tilde{\mu} & = G\left(m_T + m_C\right) \\ m_{red} & \triangleq \dfrac{m_t m_C}{m_T + m_C} \end{cases} \tag{3.53}$$

Equation (3.53) can be expanded in the non-inertial frame $\mathcal{N}$, and projected onto it through $\mathbf{R}_{\mathcal{J}\to\mathcal{N}}$, obtaining the ODE that describes the chaser translational dynamics with respect to the deflected target, seen by the latter $\mathcal{N}$ frame and written in the same frame components

$$
\begin{cases}
\ddot{\underline{q}} = & -\tilde{\mu}\frac{\underline{q}}{q^3} - \left(\left[{}^{\mathcal{N}}\underline{\Omega}_{\mathcal{N}\mathcal{I}}\right]^{\wedge}\left(\left[{}^{\mathcal{N}}\underline{\Omega}_{\mathcal{N}\mathcal{I}}\right]^{\wedge}\underline{q}\right) + \left[{}^{\mathcal{N}}\dot{\underline{\Omega}}_{\mathcal{N}\mathcal{I}}\right]^{\wedge}\underline{q} + 2\left[{}^{\mathcal{N}}\underline{\Omega}_{\mathcal{N}\mathcal{I}}\right]^{\wedge}\dot{\underline{q}}\right) + \\
& -\mu_{\odot}\left(\frac{{}^{\mathcal{N}}\underline{R}_C}{R_C^3} - \frac{{}^{\mathcal{N}}\underline{R}_T}{R_T^3}\right) + \frac{{}^{\mathcal{N}}\underline{F}_{\epsilon\mu T\to C}}{m_{RED}} + \frac{{}^{\mathcal{N}}\underline{F}_{th}}{m_C} \\
{}^{\mathcal{N}}\underline{R}_T & = \mathbf{R}_{\mathcal{L}_n\to N}\,{}^{\mathcal{L}_n}\underline{R}_T \\
{}^{\mathcal{N}}\underline{R}_C & = {}^{\mathcal{N}}\underline{R}_T + \underline{q}; \\
\dot{\underline{q}}(t_i) & = [0,0,0]^T \\
\underline{q}(t_i) & = [0,-d_{hover},0]^T
\end{cases}
\tag{3.54}
$$

where $\underline{q}$ is the chaser's relative position with respect to the deflected target, $\dot{\underline{q}}$ is its relative velocity seen by the $\mathcal{N}$ frame, and vectors ${}^{\mathcal{N}}\dot{\underline{\Omega}}_{\mathcal{N}\mathcal{I}}$ and ${}^{\mathcal{N}}\underline{\Omega}_{\mathcal{N}\mathcal{I}}$ are the angular velocity and acceleration of $\mathcal{N}$ with respect to $\mathcal{I}$ computed using equations (2.41) applied to the osculating orbit of the deflected target.

Note that equation (3.54) initial conditions are obtained imposing the tangential tugging to take place along the instantaneous velocity vector, behind the target. Note also that the contribution of (2.11) can be identified in both equations (3.51) and (3.54), and that the $\tilde{\mathcal{N}}$ notation used to indicate the osculating NTH frame, introduced in section 2.6, is here replaced with $\mathcal{N}$.

Imposing the GMT and DCL

Being the relative dynamics of the chaser written in frame $\mathcal{N}$, the proposed GMT is obtained imposing $\ddot{\underline{q}} = 0$ and $\dot{\underline{q}} = 0$ in equation (3.54).

The chaser's dipole unit vector is defined by equations (3.16) or (3.22), and its magnitude is assumed to be

1. **Constant magnetic dipole magnitude**
   The magnitude of the chaser's dipole is kept at the maximum value achievable by the chaser's SMS, for the entire duration of the tug. Considering the TM3, such value is $\mu_{\epsilon\mu,w}$ and it is set at interception epoch to satisfy equation (3.40), when the worst relative dipole orientation (i.e., target's dipole orthogonal to orbital plane) is chosen as a design condition.

$$\mu_{\epsilon\mu_C} = \mu_{\epsilon\mu,w} \tag{3.55}$$

2. **Modulated magnetic dipole magnitude**
   The magnitude of the chaser's dipole is modulated as

$$\mu_{\epsilon\mu_C} = \frac{\mu_{\epsilon\mu,w}}{\tilde{K}_r(Az_T, h_T)} \tag{3.56}$$

   where $\tilde{K}_r(Az_T, h_T)$ is the normalised radial relative orientation coefficient K_r, associated to the chosen DCL, defined in equations (3.18) and (3.23).

It is therefore possible to compute the chaser's control force that allows the non-inertial hover (i.e., ${}^{\mathcal{N}}\underline{F}_{th,eq}$) inverting equation (3.54) with the imposed DCL. Moreover, the RNI requirement is introduced assuming that the chaser body fixed frame is perfectly tracking the deflected target NTH one. Meaning that the $\mathcal{B}_{\mathcal{C}}$ can be confused with $\mathcal{N}$, and that the tangential force component ${}^{\mathcal{N}}\underline{F}_{th,eq} \cdot \hat{t}$ is amplified by the thrust efficiency defined in equation (2.24) (i.e., $\eta_t h$).

The chaser's mass evolution in time is found considering independent thrust generation units, along $\mathcal{B}_{\mathcal{C}}$'s axes, as

$$\begin{cases} F_n = \left|{}^{\mathcal{N}}\underline{F}_{th,eq} \cdot \hat{n}\right| + \left|({}^{\mathcal{N}}\underline{F}_{th,eq} \cdot \hat{t}/\eta_{th})\right| + \left|{}^{\mathcal{N}}\underline{F}_{th,eq} \cdot \hat{h}\right| \\ \dot{m}_C = -\frac{F_n}{g_0\, Isp} \\ m_C(t_i) = m_{C0} \end{cases} \tag{3.57}$$

where F_n is the total thrust that the chaser's PS shall generate, and the component along $\hat{t}$ is amplified to consider the adapted canted pair of nozzles that allows RNI satisfaction.

Under the same assumptions, the torque that the AOCS of the chaser shall develop to maintain the tug is obtained inverting (3.49) after imposing the perfect $\mathcal{N}$ tracking.

RTS satisfaction

The hovering position is assumed to be equal to the one found by application of the proposed GMT model presented in section 3.3. Being such model performed without any non-inertial contribution nor any magnetic contributions different from the radial one, the chaser's PS may be required to generate a total thrust F_n higher than its actual capabilities. These latter is set by the GMT model to be

$$\begin{cases} max(F_n) = POD\, m_{dry} \frac{\xi_{th}}{\tau_{pw}} & (GT) \\ max(F_n) = \alpha_{POD}\, POD m_{dry} \frac{\xi_{th}}{\tau_{pw}} & (GMT) \end{cases} \tag{3.58}$$

To re-establish the RTS satisfaction, in case of $F_n > max(F_n)$, the fixed hovering position is increased.

3.4.2 Numerical propagation and results

Equations (3.50), (3.54), (3.57) and (3.49) are implemented and propagated through Simulink® using ODE45 solver with an integration tolerance of $1e-14$, for the target I only (i.e., Braille), following the same logic behind the deflection evaluation in section 3.3. The numerical propagation error is checked with ODE113 solver, finding no significant difference in the obtained results.

$$\begin{aligned} t_{tug} &= 1.428 T_{nT} \\ \Delta(dr) &= 45.7\ \% \\ d_{hovering} &= 272.15\ m \end{aligned}$$

Table 3.6: *Nominal GMT tug conditions.*

The propagation is performed for a total tugging time associated to the maximum relative percentage increment in deflection, using TM3, identified in section 3.3, visible in figure 3.22.

The performance of the deflection is evaluated considering a target characterised with a magnetic dipole either orthogonal to the target's orbital plane (i.e., $h_{\epsilon\mu T} = 90^o$) or always contained in the target's orbital plane (i.e., $h_{\epsilon\mu T} = 0^o$), and assuming a rotational period of $T_{nT}/4$. Table 3.6 summarized such conditions.

Target pointing DCL

The achieved deflection at MOID, visible in figure 3.47, shows that the chaser is able to maintain the hovering position adopting both modulated and constant magnetic dipole, and achieve a deflection close to the predicted one by the GMT model. However, in the constant chaser's dipole case, the total thrust F_n that the chaser shall generate is too high for its fixed PS and PGS efficiency. This is happening mainly due to the radial relative orientation coefficient K_r that, for the test target, reaches values up to two times the one used to design the chaser (i.e., nominal hovering position). As a consequence, the relative hovering distance shall be increased by $25m$ from the nominal value, to re-establish the RTS satisfaction.

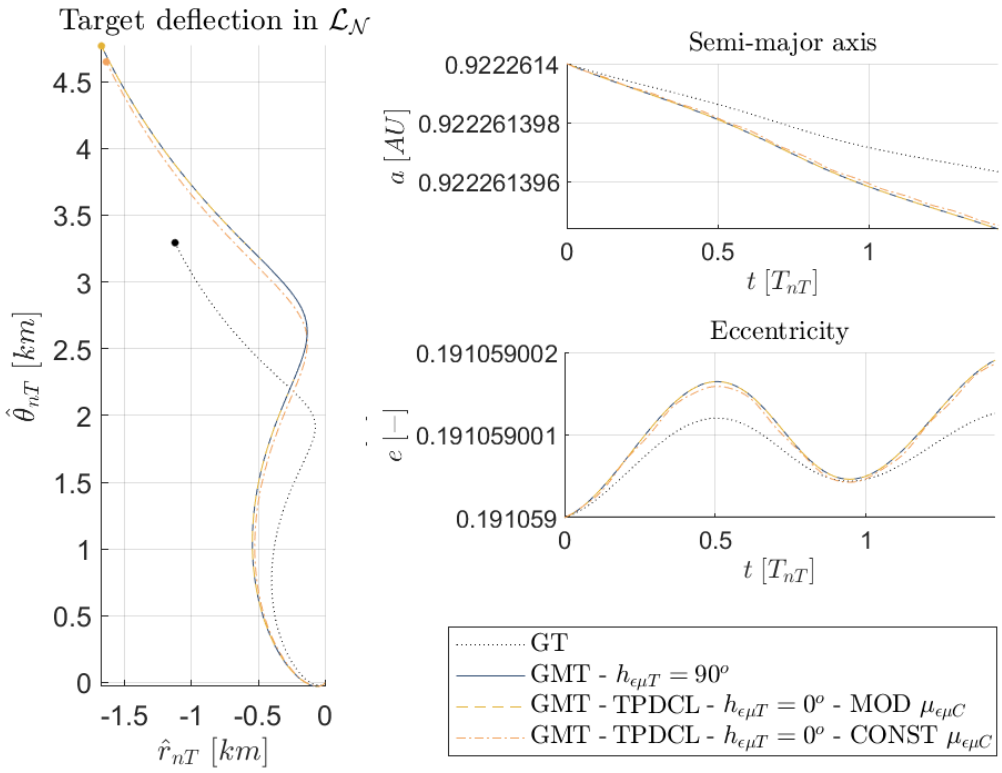

Figure 3.47: *Deflection at MOID using the target pointing DCL (i.e., TPDCL), target's semi-major axis and its eccentricity as a function of the simulation time*

Modulating the chaser's dipole in order to maintain the designed radial interaction magnitude, the chaser is able to maintain the hovering at a position which is $\sim 1m$ farther than the nominal one found with the proposed GMT model.

The control force and torque generated by the chaser's AOCS, and the magnetic dipole magnitude obtained by its SMS are shown in figure 3.48.

When the chaser is operating with a constant $\mu_{\epsilon\mu,C}$ magnitude, the farther hovering distance leads to a better thrust efficiency η_{th}, thus to a slightly higher maximum maintainable LTA on the target. For the considered test case, the torque acting on the chaser is reaching values up to $2Nm$ and evolves in time according to the target's dipole evolution in $\mathcal{N}$ frame. The chaser's internal angular momentum management may not be sufficient to stabilize the chaser, and adequate strategies shall be considered to re-gain controllability (e.g., scheduled usage of the SMS for tugging purposes). This is not addressed in the thesis, and it is left to future work.

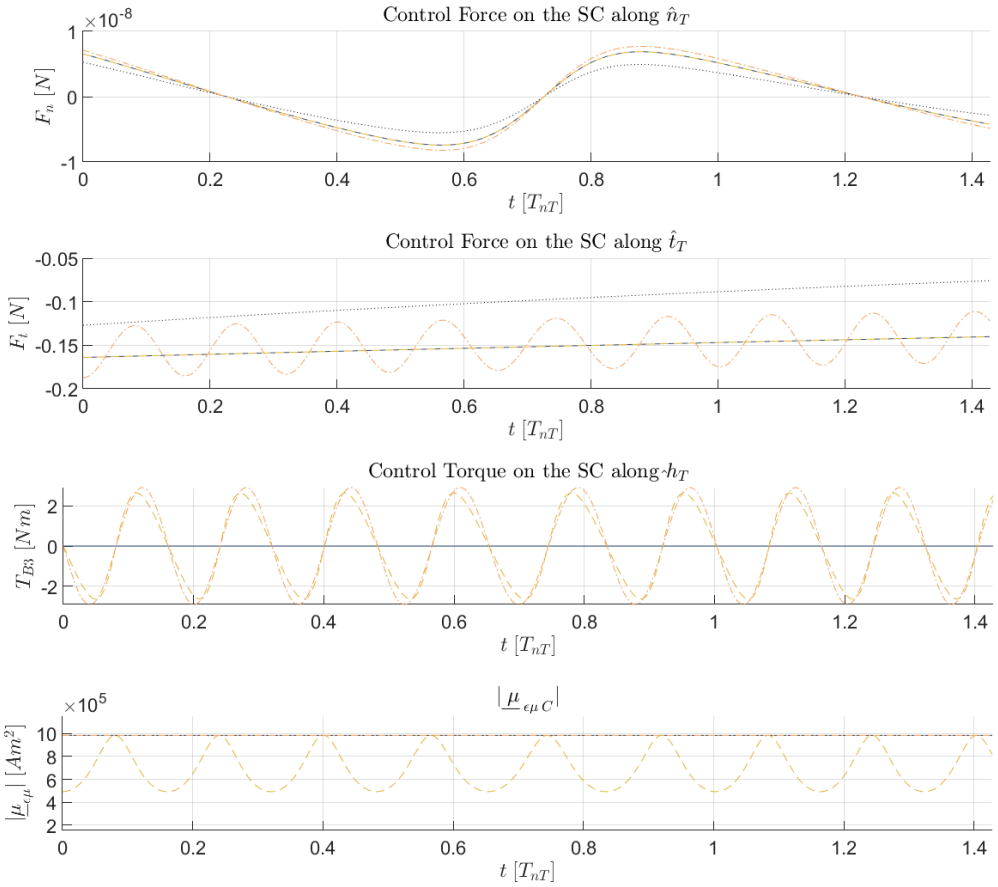

Figure 3.48: *Control force and toqrue profiles and magnetic dipole magnitude as a function of propagation time, using the target pointing DCL (i.e., TPDCL).*

Furthermore, the farther hovering distance obtained adopting a constant $\mu_{\epsilon\mu_C}$ leads to a lower fuel consumption, presented in appendix B. This can be used to increase the total tugging time of a thrusting arc that ends before the MOID epoch and designed with the nominal total tugging time reported in table 3.6.

B-field aligned DCL

The performance of the deflection is evaluated with the same condition reported in table 3.6, using the b-field aligned DCL. The achieved deflection at MOID, visible in figure 3.49, shows that the chaser is able to maintain the hovering position adopting both modulated and constant magnetic dipole, and achieve a deflection close to the predicted one by the GMT model. In this case, the magnetic interaction can be characterized by a non null K_σ (i.e., component orthogonal to the chaser's position unit vector) and a higher K_r with respect to the one achieved with the target pointing DCL.

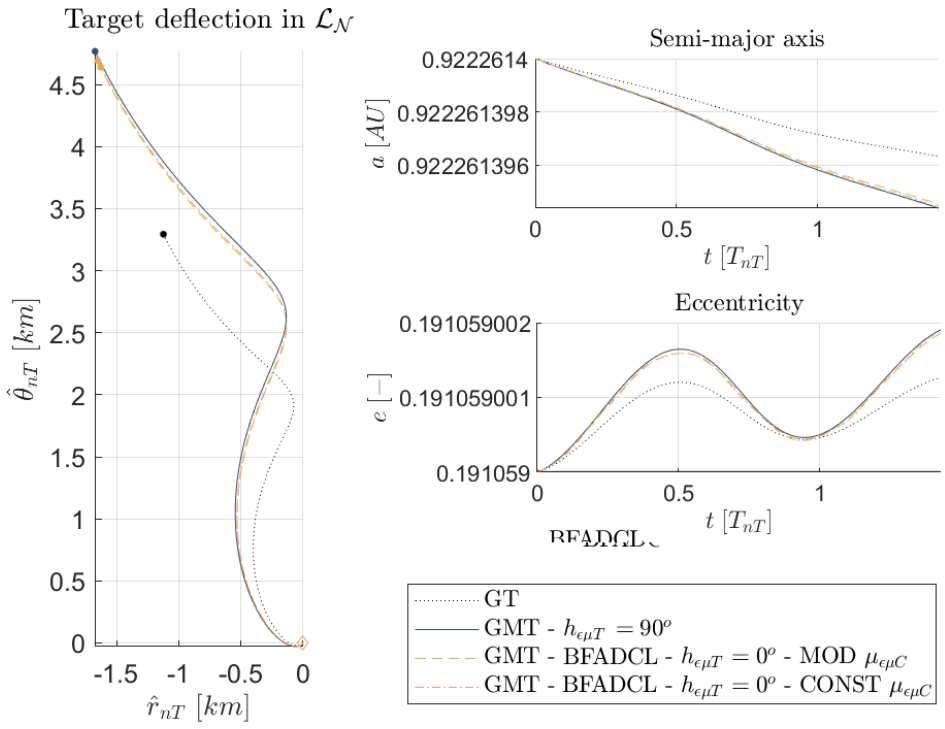

Figure 3.49: *Deflection at MOID using the B-field aligned DCL (i.e., BFADCL), target's semi-major axis and its eccentricity as a function of the simulation time*

The modulation of the chaser's dipole magnitude brings to a shift in relative hovering distance of $\sim 3m$ whereas, maintaining a constant dipole, the shift increases up to $\sim 24.5m$. Figure 3.50 shows the control force, the control torque, and the magnetic dipole magnitude obtained with the considered chaser and test target. Using the B-field DCL leads to the absence of the magnetic contribution that acts on the chaser, obtaining a reduction of the workload on its AOCS. The only torque contribution is related to the $\mathcal{B}_\mathcal{C}$ frame tracking the $\mathcal{N}$ frame.

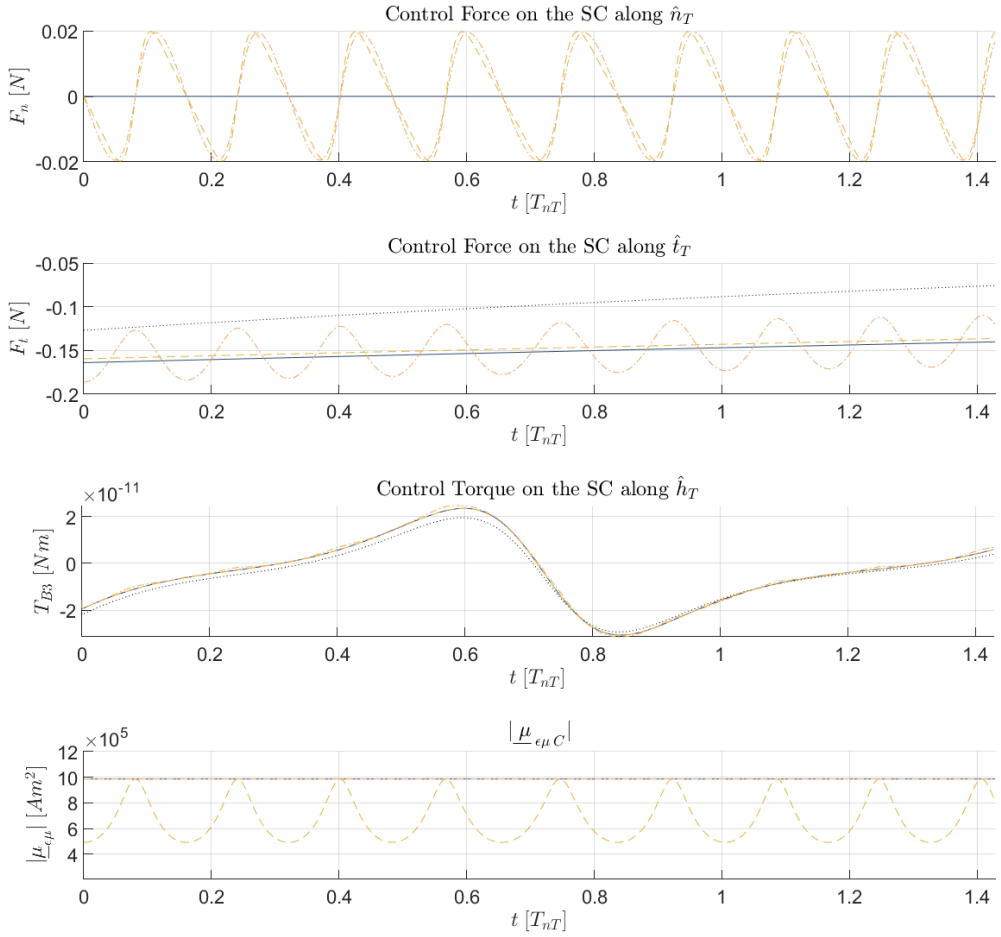

Figure 3.50: *Control force and torque profiles and magnetic dipole magnitude as a function of propagation time, using B-field aligned DCL (i.e., TPDCL).*

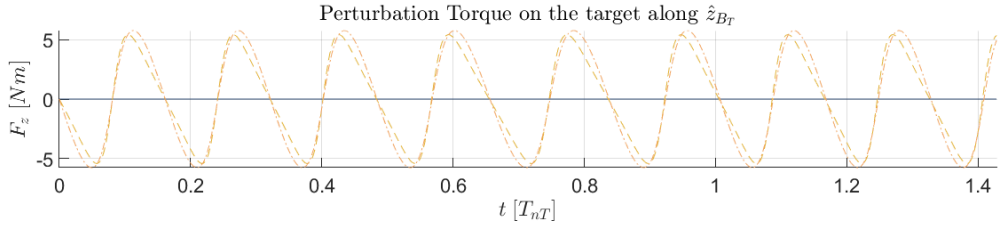

Figure 3.51: *Torque acting on the the target as a function of propagation time, using B-field aligned DCL.*

Note that, when the magnetic force is pointing the target, the control torque on the chaser and the perturbing magnetic torque on the target are the same. Using the B-field aligned, the magnetic torque acting on the target is incresed [65]. This is visible in figure 3.51, and it may be used to control the target's attitude while tugging it.

Deflection sensitivity to the target's rotational axis and dipole orientation at interception epoch

The deflection sensitivity with respect to the initial orientation of the target's rotational axis $\hat{l}_\omega$ and the target's dipole direction $\underline{\mu}_{\epsilon\mu,T}$ evaluated at interception epoch, is briefly covered. The propagation is applied on the test target (i.e., Apophis), assuming 50 randomly selected orientations for both $\hat{l}_\omega$ and $\underline{\mu}_{\epsilon\mu,T}$, using the TM3, adopting the B-field aligned DCL and the magnetic dipole magnitude modulation.

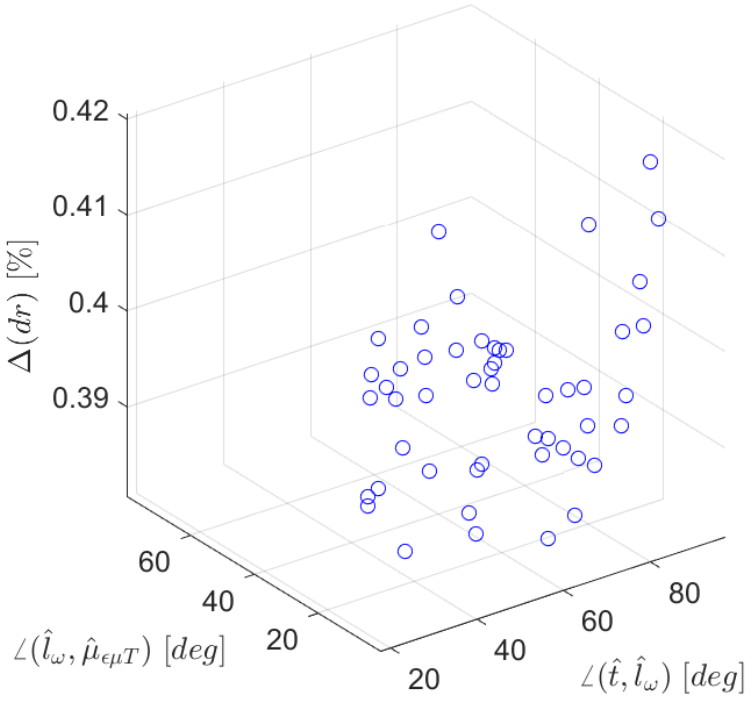

Figure 3.52: *Relative percentage increment in deflection, with magnetic dipole magnitude modulation, as a function of the angles between the tugging direction and target's rotational axis, and target's dipole and its rotational axis.*

The results, presented in figure 3.52, show that the achieved relative increment in deflection with respect to the classical GT is affected by both $\hat{l}_\omega$ and $\mu_{\epsilon\mu_T}$. The lowest observed increment reaches values as low as $\Delta(dr) = 38.1\%$. The higher the angle

between the target's rotational axis and the tugging direction is, the higher is the relative increment in deflection, when a low angle between the target's rotational axis and the target's dipole direction is considered. The resulting increment in relative hovering distance is shown in figure 3.53, and it can be as high as $dh_{hover} = 5\,[m]$.

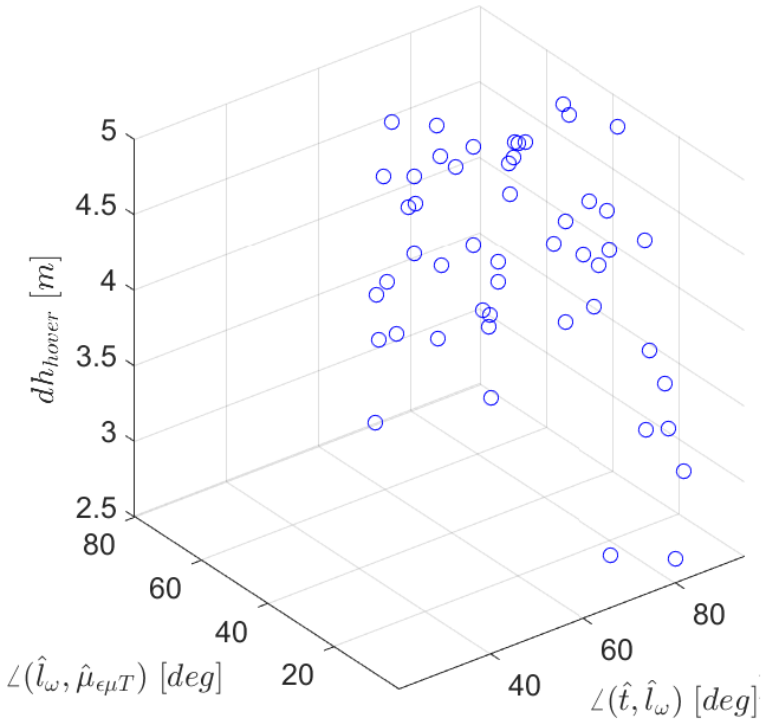

Figure 3.53: *Relative hoovering distance increment, with magnetic dipole magnitude modulation, as a function of the angles between the tugging direction and target's rotational axis, and target's dipole and its rotational axis.*

When a constant chaser's dipole magnitude is considered, the decrement in GMT performance can reach higher values (i.e., $min(\Delta(dr)) =\sim 30\%$) and the relative hovering distance increases as high as $dh_{hover} = 24.5\,[m]$.

3.5 Summary

The analysis performed in section 3.2.3 allowed to select a test target, among the identified NEA with a global magnetisation state. The study performed in section 3.2.4 brought to the definition of two DCLs and to the identification of the optimal target's dipole orientations, measured in the target's NTH frame, that allow the maximization/minimization of the magnetic force component aligned with the target's

velocity vector.

The model developed in section 3.3 allowed to design the chaser's internal mass allocation, the hovering position, and the SMS efficiency that allow the chaser to maintain the GMT tug for a given nominal total tugging time. This is done considering both chaser's thrusting capabilities and PS geometry, aiming to satisfy both RNI and RTS, and considering the target-chaser relative orientation that leads to the highest required chaser's dipole. This forces the SMS to achieve the design magnetic interaction when the target's dipole has an orientation that minimize the achievable magnetic interaction (i.e., target's magnetic dipole is orthogonal to its orbital plane, or smallest K_r), thus allowing the operations to be carried out at a minimum relative hovering distance equal to the nominal one.

Three different tugging modes are proposed and compared, identifying the optimal total tugging time that maximize the relative percentage increment in deflection at MOID, and the SMS efficiency in terms of generated magnetic dipole weighted over the power mass allocated to such subsystem. Among them, TM1 results to be the most performant one, but requires the highest SMS efficiency among the proposed TMs. The analysis performed in section 3.2 allowed to study the sensitivity of the achieved deflection with respect to a selection of parameters of the GMT model. The results show that, the GMT performs well with target's characterised by small radius and small mass, and with small total tugging times. This suggests the application of the GMT when the warning time is high and the thrusting arc can be collocated far from the MOID epoch.

The relative dynamics propagation, presented in section 3.4, allowed to understand the actual performance achieved by a chaser, designed to operate at the nominal tugging conditions defined in section 3.3, and used when the target's is characterised by a magnetic dipole direction that evolves in the target's NTH frame. The results show that, the design relative hovering position shall be increased to allow the chaser satisfy RTS, leading to a better thrust efficiency, to a smaller fuel consumption, and to a higher achievable total tugging time. This hovering distance increment is dependant upon the adopted DCL, the initial tumbling state of the target, the target's dipole initial orientation at interception epoch, and upon the non-inertial contributions characterizing the close target operations. The results also show that the B-field aligned DCL is the best approach to mitigate the workload over the chaser's AOCS, and to impart the highest magnetic torque on the target. However, it does not generate a pure radial magnetic interaction with the target, as the target point DCL does.

The relative percentage increment in deflection is reduced with respect to the nominal value achieved in design conditions, however, such decrement is contained and the GMT performance results to be always greater than the classical GT one.

Chapter 4

Conclusions

The aims of this dissertation is to understand weather or not the deflection achieved by a classic GT can be improved by the introduction of a magnetic interaction between the target and the chaser, in addition to their mutual gravitational attraction.

The results of the preliminary analysis carried out in the dissertation show that there are conditions for which the exploitation of a magnetic interaction, with a NEO that have a residual magnetisation state, may lead to some benefits from both deflection magnitude at MOID and safety of the proximity operations. Generally, when the target is suitable for a GT (i.e., small mass and small equivalent radius), the GMT has an appreciable performance.

Considering the selected targets, the highest relative percentage increment in deflection at MOID is as high as $\Delta(dr) \sim 50\%$, obtained when the target has a magnetic dipole orthogonal to its orbital plane. The performance can be further increased if the GMT is acting on the target for a short amount of tugging time, close to interception epoch. For the virtual target I (i.e., Apohpis), the optimal total tugging time is $t_{tug} \sim 1.43\,[T_{nT}]$. However, the SMS required to operate shall be able to generate a magnetic dipole that can easily reach values that may not be achievable with nowadays high TRL space technology. This shall also be integrable in the chaser's structure and operate with a specific allocated power mass budget. For the virtual target I, the chaser's dipole magnitude is in the order of $\mu_{\epsilon\mu,C} \sim 984553\,[Am^2]$, generated by a SMS with an efficiency of $\mu_{\epsilon\mu,C}/m_{pw,\epsilon\mu} \sim 3709\,[Am^2/kg]$, and a dedicated power mass of $m_{pw,\epsilon\mu} \sim 265\,[kg]$.

The relative percentage increment is highly affected by the target tumbling state at interception epoch, and it is reduced when the actual non-inertial hover about the target is considered. Results from the target-chaser dynamic propagation show that, the design hovering position must shift to farther location, allowing the chaser with

fixed performance and fixed internal mass allocation to maintain the tug. This also leads to a higher maintainable total tugging time with respect the nominal one, being the thrust efficiency of the canted PS higher, that may be used to further increase the achievable deflection if the GMT is operating far from MOID epoch. Nevertheless, such reduction is contained and the relative percentage increment remains positive, when the GMT is lasting for a total tugging time equal to the nominal one. Results obtained for target I show that, the reduction of the relative percentage increment in deflection at MOID is dependant upon the chosen DCL, and can be as low as $\Delta(dr) \sim 38\%$. The hovering position shift can be as high as $d_{hover} \sim 25\,[m]$.

4.1 Future work

The analysis developed in the thesis is particularised for non-inertial hovering conditions that allow the tug to happen along the velocity vector of a target with known global magnetization state, considering the ideal control action that the chaser would need to implement to maintain the hover. Furthermore, the mutual magnetic interaction of the objects is approximated using the far-field formulation and described using the magnetic dipole theory.

The work developed may be extended to assess the chaser actual controllability, and evaluate its internal momentum management strategy. The work may also be extended to consider non uniformities in the target's magnetic properties, non-spherical and uniform mass distributions, and the possibility of magnetic interaction modified by mechanisms here not considered.

The adoption of different GT approaches, other than the non-inertial hover along the velocity vector, shall be considered (e.g., shifted Keplerian orbits, Keplerian arcs) as well as the utilization of multiple chasers in cooperation close to the target. Furthermore, the actual TRL of the SMS capable to generate the chaser magnetic dipole is not addressed and shall be investigated.

Appendix A

Free-free dipole model matrices

$$\boldsymbol{\Phi}_i = \boldsymbol{\Phi}_i(\hat{r}, \hat{\mu}_{\epsilon\mu,i}) = \begin{bmatrix} 2ax & ay+bx & az+cx \\ ay+bx & 2by & bz+cy \\ az+cx & bz+cy & 2cz \end{bmatrix} +$$

$$-(ax+by+cz)\begin{bmatrix} 5x^2-1 & 5xy & 5xz \\ 5xy & 5y^2-1 & 5yz \\ 5xz & 5yz & 5z^2-1 \end{bmatrix}$$

$$\boldsymbol{\beta}_i = \boldsymbol{\beta}_i(\hat{r}) = \begin{bmatrix} 3x^2-1 & 3xy & 3xz \\ 3xy & 3y^2-1 & 3yz \\ 3xz & 3yz & 3z^2-1 \end{bmatrix}$$

Appendix B

Additional figures

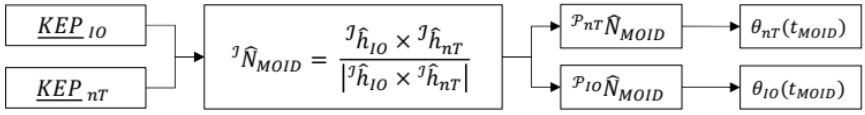

Figure B.1: *Flow-chart for geometric MOID computation. $\mathcal{P}_i$ is the perifocal frame of object i.*

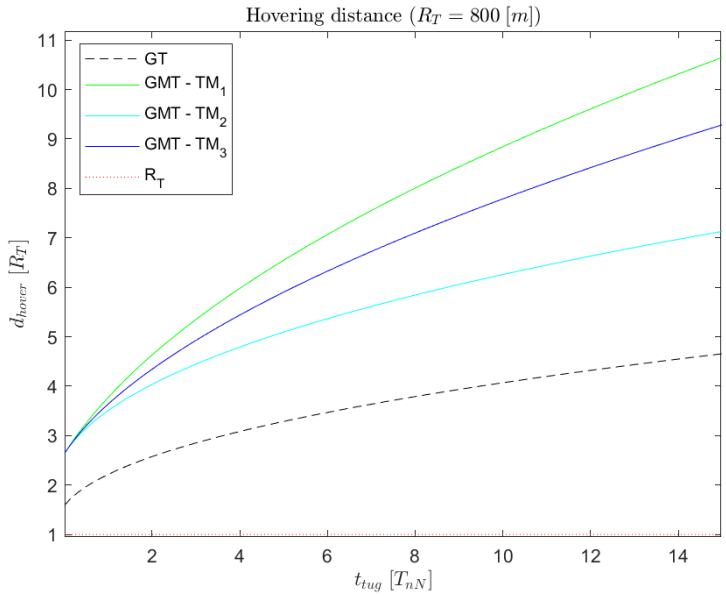

Figure B.2: *Relative hovering distance with respect to target II as a function of the total tugging time.*

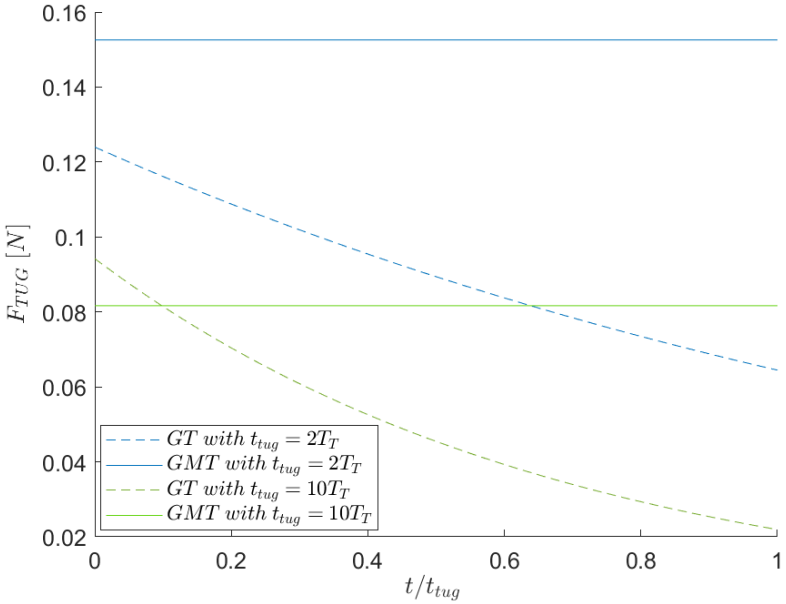

Figure B.3: *Example of interaction force profile for target I, using TM1*

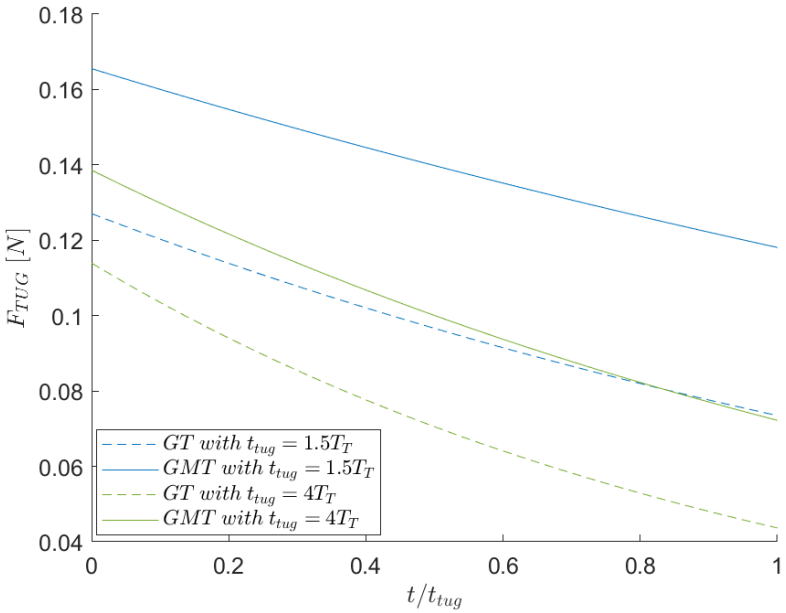

Figure B.4: *Example of interaction force profile for target I, using TM2*

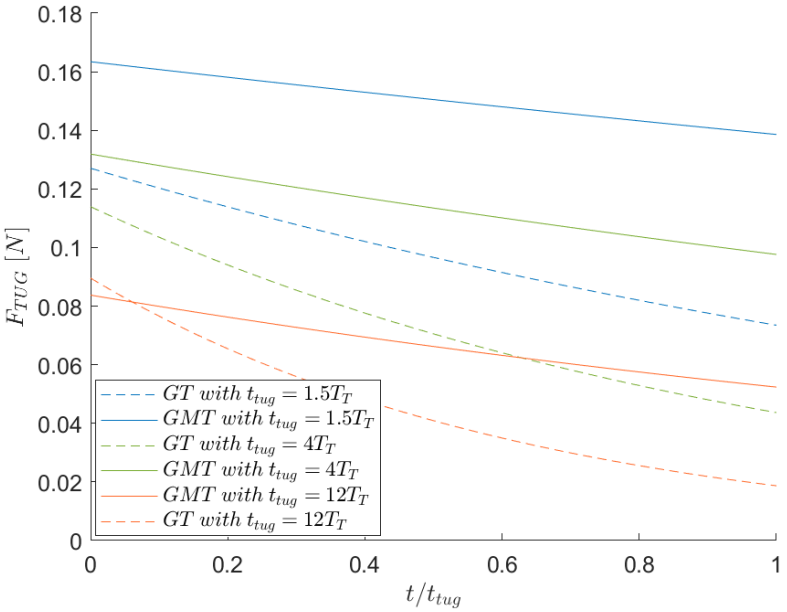

Figure B.5: *Example of interaction force profile for target I, using TM3*

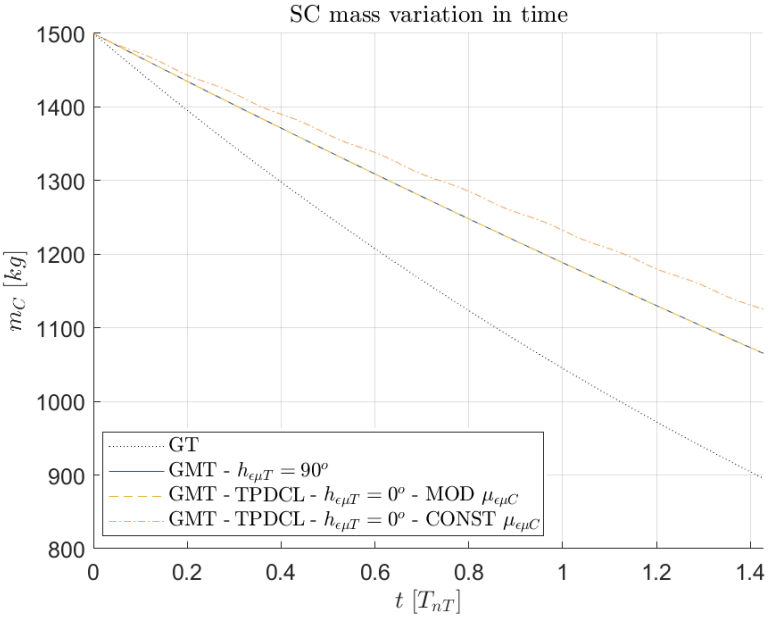

Figure B.6: *Chaser mass as a function of the simulation time, using the target pointing DCL.*

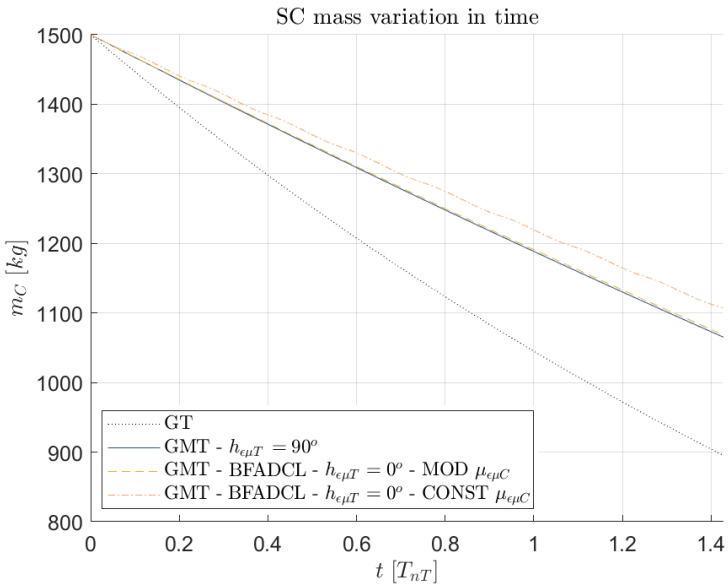

Figure B.7: *Chaser mass as a function of the simulation time, using the B-field aligned DCL.*

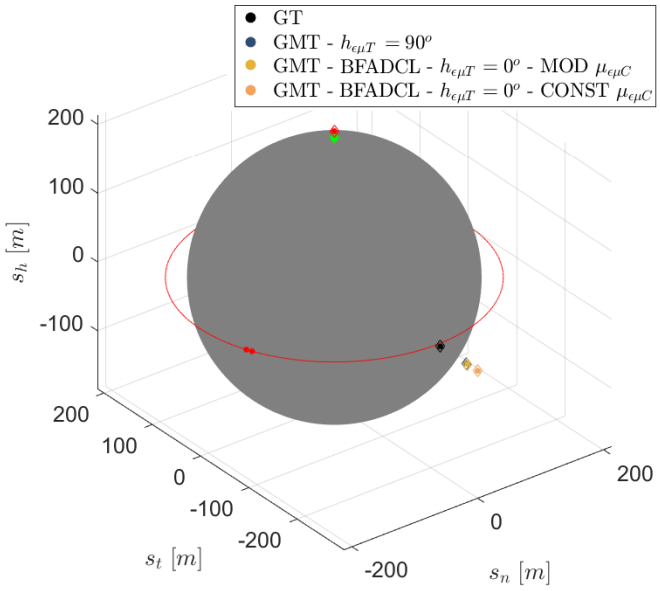

Figure B.8: *Hovering position with respect the target, using the B-field aligned DCL. Dipole evolution in red solid line, rotational axis as a green dot.*

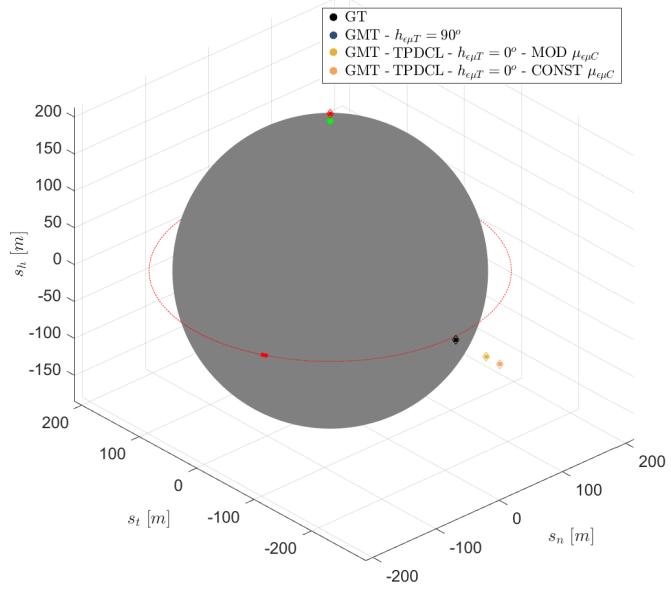

Figure B.9: *Hovering position with respect the target, using the target pointing DCL. Dipole evolution in red solid line, rotational axis as a green dot.*

Bibliography

[1] K. Lodders, 'Solar system abundances of the elements,' in *Astrophysics and Space Science Proceedings*, Springer Berlin Heidelberg, 2010, pp. 379–417. DOI: 10.1007/978-3-642-10352-0_8 (cit. on p. 1).

[2] B. Chauvineau and F. Mignard, 'Dynamics of binary asteroids,' *Icarus*, vol. 83, no. 2, pp. 360–381, Feb. 1990. DOI: 10.1016/0019-1035(90)90073-i (cit. on p. 1).

[3] G. J. Taylor, K. Keil, T. McCoy, H. Haack and E. R. D. Scott, 'Asteroid differentiation: Pyroclastic volcanism to magma oceans,' *Meteoritics*, vol. 28, no. 1, pp. 34–52, Mar. 1993. DOI: 10.1111/j.1945-5100.1993.tb00247.x (cit. on p. 1).

[4] P. Radio, 'A return to asteroid mining, and digging into space ethics with joel sercel,' 2020. [Online]. Available: https://www.planetary.org/planetary-radio/1104-2020-joel-sercel (cit. on p. 1).

[5] J. Drmola and T. Hubik, 'Kessler syndrome: System dynamics model,' *Space Policy*, vol. 44-45, pp. 29–39, Aug. 2018. DOI: 10.1016/j.spacepol.2018.03.003 (cit. on p. 2).

[6] S. D. Office. 'Esa, space debris by the numbers.' (1st Apr. 2021), [Online]. Available: https://www.esa.int/Safety_Security/Space_Debris/Space_debris_by_the_numbers (cit. on p. 2).

[7] Esa. 'Mitigating space debris generation.' (1st Apr. 2021), [Online]. Available: https://www.esa.int/Safety_Security/Space_Debris/Mitigating_space_debris_generation (cit. on p. 2).

[8] Tahc. 'Euler diagram of solar system bodies.' (1st Apr. 2021), [Online]. Available: https://en.wikipedia.org/wiki/List_of_Solar_System_objects (cit. on p. 2).

[9] I. A. Union. 'Resolution b5 - definition of a planet in the solar system.' (), [Online]. Available: https://www.iau.org/static/resolutions/Resolution_GA26-5-6.pdf (visited on 25/11/2020) (cit. on p. 3).

[10] T. M. P. Center. 'Closest approaches to the earth by comets.' (), [Online]. Available: https://www.minorplanetcenter.org/iau/lists/ClosestComets.html (visited on 25/11/2020) (cit. on pp. 3, 5).

[11] A. of Harvard and Smithsonian. 'Center for near earth obect studies.' (), [Online]. Available: https://cneos.jpl.nasa.gov/ (visited on 30/04/2020) (cit. on p. 3).

[12] ESA. 'Near earth object coordination centre (neocc).' (), [Online]. Available: http://neo.ssa.esa.int/neo-home (visited on 30/04/2020) (cit. on p. 4).

[13] A. Morbidelli, *Origin and evolution of near earth asteroids*, 2001. DOI: 10.1007/978-94-010-0712-2_19 (cit. on p. 4).

[14] S. R. Chesley, P. W. Chodas, A. Milani, G. B. Valsecchi and D. K. Yeomans, 'Quantifying the risk posed by potential earth impacts,' *Icarus*, vol. 159, no. 2, pp. 423–432, Oct. 2002. DOI: 10.1006/icar.2002.6910 (cit. on p. 5).

[15] P. Pravec, A. W. Harris and B. D. Warner, 'NEA rotations and binaries,' *Proceedings of the International Astronomical Union*, vol. 2, no. S236, pp. 167–176, Aug. 2006. DOI: 10.1017/s1743921307003201 (cit. on p. 6).

[16] L. Siltala and M. Granvik, 'Asteroid mass estimation with the robust adaptive metropolis algorithm,' *Astronomy & Astrophysics*, vol. 633, A46, Jan. 2020. DOI: 10.1051/0004-6361/201935608 (cit. on p. 6).

[17] E. Greenstadt, 'Conditions for magnetic interaction of asteroids with the solar wind,' *Icarus*, vol. 14, no. 3, pp. 374–381, Jun. 1971. DOI: 10.1016/0019-1035(71)90008-x (cit. on p. 6).

[18] N. Omidi, X. Blanco-Cano, C. T. Russell, H. Karimabadi and M. Acuna, 'Hybrid simulations of solar wind interaction with magnetized asteroids: General characteristics,' *Journal of Geophysical Research: Space Physics*, vol. 107, no. A12, SSH 12–1–SSH 12–10, Dec. 2002. DOI: 10.1029/2002ja009441 (cit. on p. 6).

[19] B. Anderson and M. Acuña, 'Search for solar wind–asteroid interactions at eros,' *Advances in Space Research*, vol. 33, no. 11, pp. 1989–1995, Jan. 2004. DOI: 10.1016/j.asr.2003.03.032 (cit. on p. 6).

[20] F. Herbert, 'Solar wind interaction with asteroids,' *Advances in Space Research*, vol. 13, no. 10, pp. 249–258, Oct. 1993. DOI: 10.1016/0273-1177(93)90076-n (cit. on p. 6).

[21] M. G. Kivelson, L. F. Bargatze, K. K. Khurana, D. J. Southwood, R. J. Walker and P. J. Coleman, 'Magnetic field signatures near galileo's closest approach to gaspra,' *Science*, vol. 261, no. 5119, pp. 331–334, Jul. 1993. DOI: 10.1126/science.261.5119.331 (cit. on pp. 6, 7).

[22] I. Richter, C. Koenders, K. H. Glassmeier, B. T. Tsurutani and R. Goldstein, 'Deep space 1 at comet 19p/borrelly: Magnetic field and plasma observations,' *Planetary and Space Science*, vol. 59, no. 8, pp. 691–698, Jun. 2011. DOI: 10.1016/j.pss.2011.02.001 (cit. on p. 6).

[23] O. P. Popova, P. Jenniskens, V. Emel'yanenko *et al.*, 'Chelyabinsk airburst, damage assessment, meteorite recovery, and characterization,' *Science*, vol. 342, no. 6162, pp. 1069–1073, Nov. 2013. DOI: 10.1126/science.1242642 (cit. on p. 6).

[24] P. Rochette, J. Gattacceca, M. Bourot-denise, G. Consolmagno, L. Folco, T. Kohout, L. Pesonen and L. Sagnotti, 'Magnetic classification of stony meteorites: 3. achondrites,' *Meteoritics & Planetary Science*, vol. 44, no. 3, pp. 405–427, Mar. 2009. DOI: 10.1111/j.1945-5100.2009.tb00741.x (cit. on p. 6).

[25] D. Hercik, H.-U. Auster, D. Constantinescu *et al.*, 'Magnetic properties of asteroid (162173) Ryugu,' *Journal of Geophysical Research: Planets*, vol. 125, no. 1, Jan. 2020. DOI: 10.1029/2019je006035 (cit. on pp. 6, 7).

[26] I. Richter, H. U. Auster, K. H. Glassmeier, C. Koenders, C. M. Carr, U. Motschmann, J. Müller and S. McKenna-Lawlor, 'Magnetic field measurements during the Rosetta flyby at asteroid (21)lutetia,' *Planetary and Space Science*, vol. 66, no. 1, pp. 155–164, Jun. 2012. DOI: 10.1016/j.pss.2011.08.009 (cit. on p. 7).

[27] H. Auster, I. Richter, K. Glassmeier, G. Berghofer, C. Carr and U. Motschmann, 'Magnetic field investigations during ROSETTA's 2867 šteins flyby,' *Planetary and Space Science*, vol. 58, no. 9, pp. 1124–1128, Jul. 2010. DOI: 10.1016/j.pss.2010.01.006 (cit. on p. 7).

[28] P. Heinisch, H.-U. Auster, I. Richter and K. H. Glassmeier, 'Revisiting the magnetization of comet 67p/Churyumov-Gerasimenko,' *Astronomy & Astrophysics*, vol. 630, A46, Sep. 2019. DOI: 10.1051/0004-6361/201834278 (cit. on p. 7).

[29] D. Herčík, H.-U. Auster, J. Blum *et al.*, 'The MASCOT magnetometer,' *Space Science Reviews*, vol. 208, no. 1-4, pp. 433–449, Jan. 2016. DOI: 10.1007/s11214-016-0236-5 (cit. on p. 7).

[30] M. Acuña, B. Anderson, C. Russell, P. Wasilewski, G. Kletetschka, L. Zanetti and N. Omidi, 'NEAR magnetic field observations at 433 Eros: First measurements from the surface of an asteroid,' *Icarus*, vol. 155, no. 1, pp. 220–228, Jan. 2002. DOI: 10.1006/icar.2001.6772 (cit. on p. 7).

[31] I. Richter, D. E. Brinza, M. Cassel, K.-H. Glassmeier, F. Kuhnke, G. Musmann, C. Othmer, K. Schwingenschuh and B. T. Tsurutani, 'First direct magnetic field measurements of an asteroidal magnetic field: DS1 at Braille,' *Geophysical Research Letters*, vol. 28, no. 10, pp. 1913–1916, May 2001. DOI: 10.1029/2000gl012679 (cit. on p. 7).

[32] N. R. Council, D. on Engineering Physical Sciences, A. S. E. Board and S. S. Board, *Defending Planet Earth*. National Academies Press, 21st Jun. 2010, 152 pp., ISBN: 0309149681 (cit. on p. 8).

[33] M. Petit, 'Optimal deflection of resonant near-earth objects using the b-plane,' M.S. thesis, Department of Aerospace Science and Technology (DAER), Politecnico di Milano, Italy, 25th Jul. 2018. [Online]. Available: http://hdl.handle.net/10589/141507 (cit. on p. 9).

[34] M. Petit and C. Colombo, 'Optimal deflection of resonant near-earth objects using the b-plane,' 3rd Apr. 2019. [Online]. Available: https://www.aiaa.org/5thCEAS/ (cit. on p. 9).

[35] J. P. Sanchez, C. Colombo, M. Vasile and G. Radice, 'Multicriteria comparison among several mitigation strategies for dangerous near-earth objects,' *Journal of Guidance, Control, and Dynamics*, vol. 32, no. 1, pp. 121–142, Jan. 2009. DOI: 10.2514/1.36774 (cit. on pp. 9, 21, 25, 29, 31).

[36] M. Vasile and C. Colombo, 'Optimal impact strategies for asteroid deflection,' *Journal of Guidance, Control, and Dynamics*, vol. 31, no. 4, pp. 858–872, Jul. 2008. DOI: 10.2514/1.33432 (cit. on pp. 9, 27).

[37] W. Tedeschi, J. Remo, J. Schulze and R. Young, 'Experimental hypervelocity impact effects on simulated planetesimal materials,' *International Journal of Impact Engineering*, vol. 17, no. 4-6, pp. 837–848, Jan. 1995. DOI: 10.1016/0734-743x(95)99904-6 (cit. on p. 9).

[38] NASA, 'Near-earth object survey and deflection analysis of alternatives,' 2007 (cit. on p. 9).

[39] *Defending Planet Earth*. National Academies Press, Jun. 2010. DOI: 10.17226/12842 (cit. on p. 9).

[40] D. Scheeres, 'Close proximity operations for implementing mitigation strategies,' in *2004 Planetary Defense Conference: Protecting Earth from Asteroids*, American Institute of Aeronautics and Astronautics, Feb. 2004. DOI: 10.2514/6.2004-1445 (cit. on p. 10).

[41] C. R. McInnes, 'Dynamics, stability, and control of displaced non-keplerian orbits,' *Journal of Guidance, Control, and Dynamics*, vol. 21, no. 5, pp. 799–805, Sep. 1998. DOI: 10.2514/2.4309 (cit. on p. 10).

[42] C. Foster, J. Bellerose, D. Mauro and B. Jaroux, 'Mission concepts and operations for asteroid mitigation involving multiple gravity tractors,' *Acta Astronautica*, vol. 90, no. 1, pp. 112–118, Sep. 2013. DOI: 10.1016/j.actaastro.2012.10.010 (cit. on pp. 10, 11).

[43] SpaceX. (15th Mar. 2021), [Online]. Available: https://www.spacex.com/vehicles/falcon-heavy/ (cit. on p. 10).

[44] L. B. King, 'Spacecraft formation-flying using inter-vehicle coulomb force, nasa final report,' 2002 (cit. on p. 10).

[45] N. Murdoch, D. Izzo, C. Bombardelli, I. Carnelli, A. Hilgers and D. Rodgers, 'Electrostatic tractor for near earth objectdeflection,' 2008 (cit. on p. 10).

[46] C. R. Seubert, L. A. Stiles and H. Schaub, 'Effective coulomb force modeling for spacecraft in earth orbit plasmas,' *Advances in Space Research*, vol. 54, no. 2, pp. 209–220, Jul. 2014. DOI: 10.1016/j.asr.2014.04.005 (cit. on p. 10).

[47] M. Vasile, A. Gibbings, I. Watson and J.-M. Hopkins, 'Improved laser ablation model for asteroid deflection,' *Acta Astronautica*, vol. 103, pp. 382–394, Oct. 2014. DOI: 10.1016/j.actaastro.2014.01.033 (cit. on p. 10).

[48] M. Vetrisano and C. C. andc, 'Asteroid rotation and orbit control via laser ablation,' *Advances in Space Research*, vol. 57, no. 8, pp. 1762–1782, Apr. 2016. DOI: 10.1016/j.asr.2015.06.035 (cit. on pp. 10, 30).

[49] M. R. LaPointe, 'Formation flying with shepherd satellites,' NASA Institute for Advanced Concepts, Tech. Rep., 2001. [Online]. Available: http://www.niac.usra.edu/files/studies/final_report/607LaPointe.pdf (visited on 04/05/2020) (cit. on p. 11).

[50] Y.-w. Zhang, L.-p. Yang, Y.-w. Zhu and H. Huang, 'Dynamics and solutions for multispacecraft electromagnetic orbit correction,' *Journal of Guidance, Control, and Dynamics*, vol. 37, no. 5, pp. 1604–1610, Sep. 2014. DOI: 10.2514/1.g000331 (cit. on p. 11).

[51] E. M. C. Kong, D. W. Kwon, S. A. Schweighart, L. M. Elias, R. J. Sedwick and D. W. Miller, 'Electromagnetic formation flight for multisatellite arrays,' *Journal of Spacecraft and Rockets*, vol. 41, no. 4, pp. 659–666, Jul. 2004. DOI: 10.2514/1.2172 (cit. on pp. 11, 41).

[52] N. O. Gómez and S. J. Walker, 'Eddy currents applied to de-tumbling of space debris: Analysis and validation of approximate proposed methods,' *Acta Astronautica*, vol. 114, pp. 34–53, Sep. 2015. DOI: 10.1016/j.actaastro.2015.04.012 (cit. on p. 11).

[53] E. Fabacher, S. Lizy-Destrez, D. Alazard, F. Ankersen and A. Profizi, 'Guidance of magnetic space tug,' *Advances in Space Research*, vol. 60, no. 1, pp. 14–27, Jul. 2017. DOI: 10.1016/j.asr.2017.03.042 (cit. on pp. 11, 24).

[54] T. Voirin, S. Kowaltschek and O. Dubois-Matra, 'Nomad: A contactless technique for active large debris removal,' in *63rd IAC, Naples, Italy*, 2012. [Online]. Available: https://iafastro.directory/iac/archive/browse/IAC-12/A6/7/14126/ (visited on 29/04/2020) (cit. on p. 11).

[55] C. R. McInnes, 'Near earth object orbit modification using gravitational coupling,' *Journal of Guidance, Control, and Dynamics*, vol. 30, no. 3, pp. 870–873, May 2007. DOI: 10.2514/1.25864 (cit. on pp. 11, 29).

[56] B. Wie, 'Dynamics and control of gravity tractor spacecraft for asteroid deflection,' *Journal of Guidance, Control, and Dynamics*, vol. 31, no. 5, pp. 1413–1423, Sep. 2008. DOI: 10.2514/1.32735 (cit. on pp. 11, 29, 62).

[57] D. Yeomans, S. Bhaskaran, S. Broschart, S. Chesley, P. Chodas, M. Jones and T. Sweetser, 'Near-earth object (neo) analysis of transponder tracking and gravity tractor performance,' B612 Foundation, Tech. Rep., 2008. [Online]. Available: https://cneos.jpl.nasa.gov/doc/b612_report.html (cit. on p. 11).

[58] W. Brown, 'A novel push-pull asteroid magnetic tractor(MT),' *Acta Astronautica*, vol. 156, pp. 371–374, Mar. 2019. DOI: 10.1016/j.actaastro.2017.12.020 (cit. on pp. 11, 13).

[59] K. Yamaguchi and H. Yamakawa, 'Orbital deflection of potentially hazardous asteroids using a coulomb force attractor,' *TRANSACTIONS OF THE JAPAN SOCIETY FOR AERONAUTICAL AND SPACE SCIENCES, AEROSPACE TECHNOLOGY JAPAN*, vol. 12, no. ists29, Tr_27–Tr_33, 2014. DOI: 10.2322/tastj.12.tr_27 (cit. on pp. 12, 29).

[60] H. D. Curtis, *Orbital Mechanics for Engineering Students*. Elsevier, 2014. DOI: 10.1016/c2011-0-69685-1 (cit. on pp. 16, 19, 20, 22, 33, 35).

[61] K. W. Yung, P. B. Landecker and D. D. Villani, 'An analytic solution for the force between two magnetic dipoles,' *Magnetic and Electrical Separation*, vol. 9, no. 1, pp. 39–52, 1998. DOI: 10.1155/1998/79537 (cit. on p. 24).

[62] K. Prytz, *Electrodynamics: The Field-Free Approach*. Springer International Publishing, 31st Mar. 2015, 388 pp., ISBN: 3319131702. [Online]. Available: https://www.ebook.de/de/product/23172912/kjell_prytz_electrodynamics_the_field_free_approach.html (cit. on p. 24).

[63] E. Fabacher, S. Lizy-Destrez, D. Alazard, F. Ankersen and J.-F. Jourdas, *Guidance and navigation for electromagnetic formation flight orbit modification*. Springer-Verlag GmbH, 4th Apr. 2015, ISBN: 9783319175188. [Online]. Available: https://oatao.univ-toulouse.fr/13830/ (cit. on p. 24).

[64] E. Fabacher, D. Alazard, F. Ankersen, S. Lizy-Destrez and L. de Mijolla, 'Control of magnetic space tug,' *IFAC-PapersOnLine*, vol. 49, no. 17, pp. 278–283, 2016. DOI: 10.1016/j.ifacol.2016.09.048 (cit. on p. 24).

[65] P. B. Landecker, D. D. Villani and K. W. Yung, 'An analytic solution for the torque between two magnetic dipoles,' vol. 10, pp. 29–33, 1999, ISSN: 1055-6915. DOI: 10.1155/1999/97902 (cit. on pp. 25, 98).

[66] C. Colombo, M. Vasile and G. Radice, 'Semi-analytical solution for the optimal low-thrust deflection of near-earth objects,' *Journal of Guidance, Control, and Dynamics*, vol. 32, no. 3, pp. 796–809, May 2009. DOI: 10.2514/1.40363 (cit. on p. 27).

[67] J. L. Gonzalo, C. Colombo and P. D. Lizia, 'Analytical framework for space debris collision avoidance maneuver design,' *Journal of Guidance, Control, and Dynamics*, vol. 44, no. 3, pp. 469–487, Mar. 2021. DOI: 10.2514/1.g005398 (cit. on p. 27).

[68] J. L. Gonzalo, C. Colombob and P. D. Lizia, 'A semi-analytical approach to low-thrust collision avoidance manoeuvre design,' in *70th International Astronautical Congress (IAC 2019)*, 21st Oct. 2019. [Online]. Available: http://hdl.handle.net/11311/1116451 (visited on 15/04/2020) (cit. on p. 38).

[69] Z. Technik. 'Zarm technik droducts datasheet.' (), [Online]. Available: https://cdn.website-editor.net/639e6263bfff47cca5f1570c039bdb44/files/uploaded/ZARM_Technik_Information.pdf (cit. on p. 40).